On Sun Testing of a Single Spike of the Spiky Central Receiver Air Preheater (SCRAP)

by

Renier Johannes Janse van Vuuren

Thesis presented in partial fulfilment of the requirements for the degree of Master of Engineering (Mechanical) in the Faculty of Engineering at Stellenbosch University

Supervisor: Dr. J. E. Hoffmann

Co-supervisor: Prof. A. B. Sebitosi

December 2020

The financial assistance of the National Research Foundation (NRF) towards this research is hereby acknowledged. Opinions expressed and conclusions arrived at, are those of the author and are not necessarily to be attributed to the NRF.

Declaration

By submitting this thesis electronically, I declare that the entirety of the work contained therein is my own, original work, that I am the sole author thereof (save to the extent explicitly otherwise stated), that reproduction and publication thereof by Stellenbosch University will not infringe any third party rights and that I have not previously in its entirety or in part submitted it for obtaining any qualification.

Date: September 2020 .....

Abstract

On Sun Testing of a Single Spike of the Spiky Central Receiver Air Preheater (SCRAP)

R. J. Janse van Vuuren

Department of Mechanical and Mechatronic Engineering,
University of Stellenbosch,
Private Bag X1, Matieland 7602, South Africa.

Thesis: MEng (Mech)

December 2020

Concentrating solar power (CSP) provides a significant advantage over other forms of renewable energy due to its high energy potential and low cost. When CSP central receiver technology is implemented in a combined Brayton-Rankine cycle with thermal energy storage (TES), the overall Brayton cycle efficiency can be increased, while allowing for dispatchable energy generation at night or during times of reduced solar radiation. The SUNSPOT cycle consists of a solarized Brayton cycle with a rock bed TES facility which powers a bottoming Rankine cycle. The Spiky Central Receiver Air Pre-heater (SCRAP) is the central receiver concept envisaged for implementation in the SUNSPOT cycle's solarized Brayton cycle. The receiver would need to provide outlet air temperatures of above 800 °C with a total pressure drop of less than 30 kPa in order to satisfy the cumulative Brayton-Rankine cycle demands.

This study sought to investigate the thermal characteristics associated with a single spike of the SCRAP receiver. To this end an experimental receiver approximating a full-scale receiver was designed based on suggestions from a previous study. The experimental receiver was installed at the Helio40 facility at the University of Stellenbosch and tested in on-sun conditions. An experimental setup was designed to capture the key variables required to analyze the spike performance. An investigation to characterize the performance of the heliostat field was also conducted.

Through experimental testing, it was found that the irradiation concentration on the spike surface increases exponentially from behind the tip, leading to low irradiation at the front of the spike. It was further found that the exponential growth would cause high heating of the receiver base due to flow separation in the air manifold, limiting the selection of construction materials for a full-scale SCRAP receiver implementation. With an open annulus spike configuration, the receiver was also found to be susceptible to convective losses.

Finally, it was found that the coiled fins are effective in increasing the spike's thermal efficiency by a great margin by virtue of increased heat transfer surface area as well as higher heat transfer coefficients, which result when

the coiled ducts impart a centrifugal force to the air flow, moving the flow closer to the spike wall. The coiled ducts would also be effective in equalizing surface temperature variations caused by uneven circumferential irradiation distributions, mitigating the effects of local hotspots.

Uittreksel

Op Son Toetsing van 'n Enkele Pen van die Puntige Sentrale Ontvanger Lug Voorverhitter (PSOLV)

("On Sun Testing of a Single Spike of the Spiky Central Receiver Air Preheater (SCRAP)")

R. J. Janse van Vuuren

Departement Meganiese en Megatroniese Ingenieurswese,
Universiteit van Stellenbosch,
Privaatsak X1, Matieland 7602, Suid Afrika.

Tesis: MIng (Meg)

Desember 2020

Gekonsentreerde sonkrag (GS) bied 'n aansienlike voordeel bo ander vorme van hernubare energie as gevolg van die hoë energiepotensiaal en lae koste. Wanneer GS sentrale-ontvanger tegnologie in 'n gekombineerde Brayton-Rankine siklus met termiese-energieberging (TEB) geïmplementeer word, lei dit tot die toename in algehele doeltreffendheid van die Brayton-siklus, terwyl dit snags of gedurende tye van verminderde sonstraling die opwekking van energie beskikbaar stel. Die SUNSPOT-siklus bestaan uit 'n gesolariseerde Brayton-siklus met 'n rotsbed TEB-fasiliteit wat 'n sekondêre Rankine-siklus dryf. Die Puntige Sentrale Ontvanger Lug Voorverhitter (PSOLV) is die sentrale-ontvanger konsep wat beoog word vir implementering in die SUNSPOT-siklus se gesolariseerde Brayton-siklus. Die ontvanger moet uitlaat lugtemperature van bo 800 °C voorsien met 'n totale drukval van minder as 30 kPa om aan die gesamentlike Brayton-Rankine-siklus se vereistes te voldoen.

Die fokus van hierdie studie was om die termiese eienskappe van 'n enkele pen van die PSOLV te karakteriseer. Vir hierdie doel was 'n eksperimentele ontvanger, wat 'n volskaalse ontvanger benader, ontwerp op grond van voorstelle uit 'n vorige studie. Die eksperimentele ontvanger was by die Helio40-aanleg aan die Universiteit van Stellenbosch geïnstalleer en met sonstraling getoets. 'n Eksperimentele opstel is ook ontwerp om die veranderlikes wat benodig word om die termiese eienskappe te karakteriseer, vas te stel. 'n Ondersoek om die bestraling uitset van die heliostaatveld te bepaal, is ook uitgevoer.

Deur middel van die eksperimentele toetse is daar gevind dat die bestralingskonsentrasie op die pen oppervlak eksponensieel van agter die punt toeneem, wat lei tot lae bestraling aan die voorkant van die pen. Daar is verder gevind dat die eksponensiële groei aansienlike verhitting van die ontvangerbasis veroorsaak as gevolg van vloei skeiding in die lugspruitstuk, wat die keuse

van konstruksiemateriaal vir ’n volskaalse PSOLV ontvanger beperk. Met ’n oop-annulus pen opstel, is die ontvanger ook sensitief teen konveksie verliese.

Laastens, is daar gevind dat die die spiraalvormige vinne effektief is om die pen se termiese doeltreffendheid te verhoog deur middel van groter hitte-oordragoppervlakte sowel as hoër hitte-oordragkoëffisiënte, wat die gevolg is van wanneer die spiraalvormige kanale ’n sentrifugale krag aan die lugvloei verleen en sodoende die vloei nader aan die penmuur beweeg. Die spiraalvormige kanale sou ook effektief wees om die oppervlaktemperatuur-variasies, wat veroorsaak word deur oneweredige bestralingsverspreidings, gelyk te maak en sodoende die gevolge van gelokaliseerde warmkolle te versag.

Acknowledgements

"Climate is what we expect, weather is what we get" - A.J. Herbertson

I would like to thank everyone that contributed to the final completion of this project. In particular,

- My mother, Marlene, for her endless love and unfaltering support.
- Dr. Jaap Hoffmann, for his patience and timely insight.
- Prof. Ben Sebitosi, for his efforts in maintaining funding for this project.
- Juliun Stanfliet and Nathi Hlwempu, for their good company.
- The mechanical workshop staff, for their help in constructing, installing and modifying the test setup.

Dedications

vir die wat wil sien
vir die wat wil hoor
vir die wat wil weet
vir die wat wil glo

Contents

List of Figures

List of Tables

Nomenclature

Constants

$R_{air} = 287.058\,J/(kgK)$

$\sigma = 5.670 \times 10^{-8}\,W/(m^2K^4)$

Abbreviations

AISI	American Iron and Steel Institute
CF	Concentration Factor
CR	Central Receiver
CSP	Concentrating Solar Power
DIAPR	Directly Irradiated Annular Pressurized Receiver
DLR	Deutsches Zentrum für Luft-und Raumfahrt
DNI	Direct Normal Irradiation
DO	Discrete Ordinates
FLHIP	Frustum Like High Pressure Window
HTF	Heat Transfer Fluid
PT	Parabolic Trough
PV	Photovoltaic
REFOS	Receiver for solar-hybrid gas turbine and CC systems
RPC	Reticulated Porous Ceramic Foam
SCRAP	Spiky Central Receiver Air Pre-heater
SOLHYCO	Solar Hybrid Power and Cogeneration
SOLUGAS	Solar Up-scale Gas
SUNSPOT	Stellenbosch University Solar Power Thermodynamic Cycle
TES	Thermal Energy Storage
WIS	Weissman Institute of Science

Variables

A	Area	$[m^2]$
A	Azimuth	$[^\circ]$
a	Annular diameter ratio	$[\ ]$
c_p	Specific heat capacity	$[J/kgK]$
D	Diameter	$[m]$
dx	Differential length	$[m]$
f	Friction factor	$[\ ]$

h	Convective heat transfer coefficient	$[\mathrm{W/m^2K}]$
I	Irradiation	$[\mathrm{W/m^2}]$
k	Thermal conductivity	$[\mathrm{W/mK}]$
L	Length	$[\mathrm{m}]$
m	Mass	$[\mathrm{kg}]$
$\dot{m}$	Mass flow	$[\mathrm{kg/s}]$
P	Pressure	$[\mathrm{Pa}]$
p	Perimeter	$[\mathrm{m}]$
$\dot{Q}$	Heat rate	$[\mathrm{W}]$
$\dot{Q}$	Volumetric flow rate	$[\mathrm{m^3/s}]$
$\dot{q}$	Heat flux	$[\mathrm{W/m^2}]$
R	Thermal resistance	$[^\circ\mathrm{C/W}]$
r	Radius	$[\mathrm{m}]$
T	Temperature	$[^\circ\mathrm{C}]$
α	Absorptivity	$[\ ]$
α	Altitude	$[^\circ]$
γ	Specific heat ratio	$[\ ]$
δ	Declination	$[^\circ]$
ϵ	Emissivity	$[\ ]$
η	Efficiency	$[\ ]$
μ	Dynamic viscosity	$[\mathrm{kg/ms}]$
ρ	Density	$[\mathrm{kg/m^3}]$
ϕ	Latitude	$[^\circ]$
Φ	Relative angle	$[^\circ]$
ω	Hour angle	$[^\circ]$

Vectors and Tensors

P	Position vector

Subscripts

ap	aperture
b	bulk
c	cross section
$conv$	convection
cv	control volume
h	hydraulic

i	inner
n	control volume number
o	outer
rad	radiation
sol	solar
w	wall

Dimensionless numbers

Nu	Nusselt number	[ ]
Re	Reynolds number	[ ]
Pr	Prandtl number	[ ]

Chapter 1

Introduction

1.1 Background

In 2015 South Africa's electricity production amounted to roughly 249.6 TWh (International Energy Agency, 2015). Of this, the main contributors were coal (91.6%), nuclear (4.9%), solar[1] (1.8%), hydro (1.5%) and wind(0.9%). Following the global trend of transitioning to green energy, South Africa has set a goal of achieving a 43% supply of renewable energy by 2030 (Department of Energy, 2015).

As part of the Department of Energy's Integrated Resource Plan for 2019 (Department of Energy, 2019), South Africa aims to decommission 5400 MW of electricity generated from coal by 2022, and another 10 500 MW by 2030. As the Koeberg nuclear power station reaches the end of its design life in 2024, a decision has also been made to extend the plant's design life by a further 20 years with aims of expanding nuclear power in the long term. In an attempt to diversify the electricity mix, renewable energy in the form of Solar photovoltaic (PV), wind and concentrating solar power (CSP) provides an excellent opportunity to provide off-grid electricity, with potential for new industry and job creation.

Due to its location, South Africa receives some of the world's highest levels of annual solar irradiation, making solar energy a highly viable option in contributing to the Department of Energy's 2030 goal (Craig *et al.*, 2017*b*). South Africa's Northern Cape, Free State and Eastern Cape provinces, shown in Figure 1.1, receive annual direct normal solar irradiation (DNI) levels higher than those of Spain and the United States of America, where the prime locations receive an annual average of 2100 and 2700 kWh/m^2 respectively. Both countries also have numerous CSP plants operating at full capacity (Craig *et al.*, 2017*a*). South Africa has therefore been identified as one of the best locations in the world for CSP power generation with an estimated nominal capacity of 547.6 GW (Fluri, 2009).

[1] Combined solar thermal and solar PV

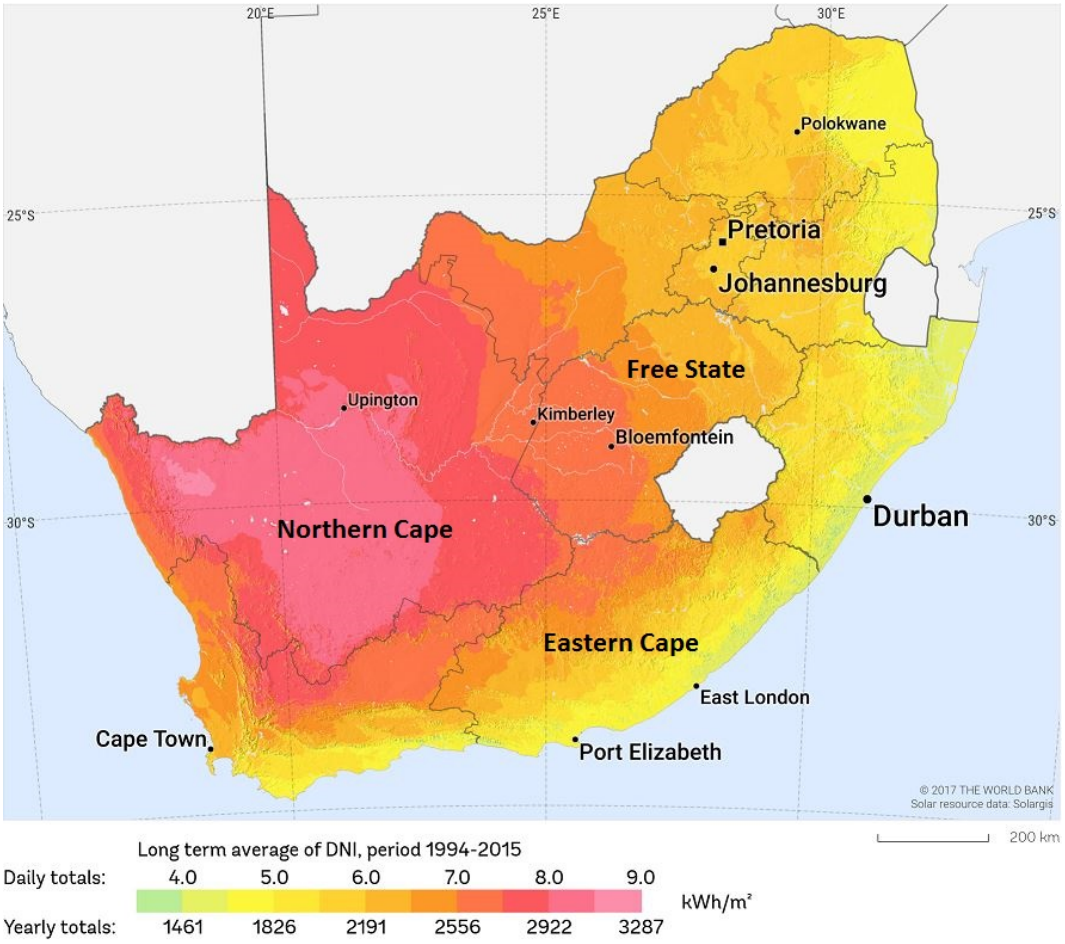

Figure 1.1: Direct normal irradiation: South Africa (SolarGIS)

1.2 Concentrating solar power (CSP) in South Africa

CSP, as it stands in South Africa, is largely centered around two dominating technologies; Solar tower and Parabolic trough (PT). While PT power has long dominated the South African CSP market, a recent shift in technology has brought focus on solar tower receivers for their ability to operate at much higher temperatures with molten salt as heat transfer fluid (HTF). Table 1.1 lists the current operational CSP power plants in South Africa.

PT technology utilizes long parabolically curved mirrors to focus solar irradiation on a central line running the length of the trough. PT systems generally display concentration factors of 30 to 80, using mostly thermal oil as HTF . Maximum achievable HTF temperatures can range anywhere from 250 °C to 400 °C. Figure 1.2a shows the Bokpoort PT CSP plant located in Groblershoop, Northern Cape.

Table 1.1: Operational CSP plants in South Africa

Project	Tech.	Capacity (MW)	Location	Commissioned
Kaxu Solar 1	PT	100	NC, Pofadder	March 2015
Khi Solar 1	Tower	50	NC, Upington	February 2016
Bokpoort CSP	PT	50	NC, Groblershoop	March 2016
Ilanga 1	PT	100	NC, Upington	November 2018
Xina Solar 1	PT	100	NC, Pofadder	December 2018
Kathu Solar Park	PT	100	NC, Kathu	January 2019
Redstone CSP	Tower	100	NC, Postmasburg	TBA

(a) Bokpoort CSP (SolarPACES, 2017)

(b) Khi Solar 1 (Abengoa, 2016)

Figure 1.2: Operational CSP plants in South Africa

Solar tower technology utilizes a field of heliostats which concentrates solar irradiation onto a tower mounted receiver. Heliostat field layouts vary based on the type of receiver used. Figure 1.2b shows the Khi Solar 1 plant located in Upington, Northern Cape. The tower, housing a three-sided cavity receiver, sits towards the far center of a surrounding heliostat field. Solar tower plants can reach concentration factors of up to 1000, depending on the number and type of heliostats used. Solar towers can therefore also provide higher HTF temperatures, generally in the range of 550 °C, using molten salts as HTF.

The HTF is used to generate steam which drives a conventional Rankine cycle to generate electricity. Due to the low concentration factor, PT plants require larger areas to generate the same power as solar tower plants. Their application is also limited to geographical areas with relatively flat terrain. Solar towers have the advantage of being deployed in locations with uneven terrain and have the ability to produce higher quality energy as a result of higher HTF temperatures.

The higher energy quality produced by solar tower systems shows large potential for reducing power generation costs as they have the ability to al-

low many intermediate power cycle steps between integration in a Rankine cycle up to Brayton gas turbine cycles which operate at temperatures of up to 1300 °C. The higher temperatures can result in larger throughput of more efficient cycles. Coupled with thermal energy storage (TES), solar tower plants have the ability to operate more than 4500 hours per year at nominal power (Romero *et al.*, 2002).

1.3 The SUNSPOT cycle

The SUNSPOT cycle (**S**tellenbosch **UN**iversity **S**olar **PO**wer **T**hermodynamic cycle) shown in Figure 1.3, as proposed by Kröger (2012), is an asynchronous combined Brayton-Rankine cycle that aims to increase thermodynamic efficiency by increasing hot end temperature in the Brayton cycle as well as provide TES in the form of a rock bed for dispatchable power generation at night.

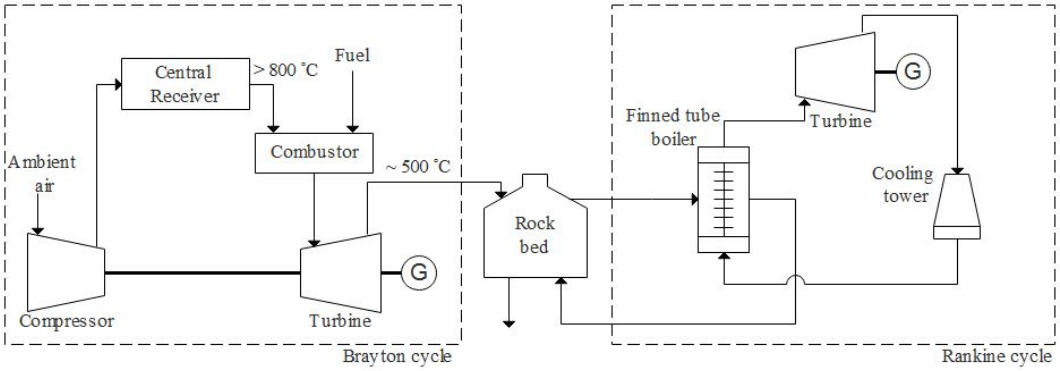

Figure 1.3: The SUNSPOT cycle (Kröger, 2012)

Pressurized air from the compressor is heated to above 800 °C in the central receiver (CR). A combustor located upstream of the turbine allows for additional air heating during times of reduced solar radiation, using natural gas or hydrogen as fuel. Exhaust gas at approximately 500 °C is ducted from the turbine to a packed rock bed TES facility. At night, hot air from the rock bed is blown through a finned tube boiler, generating steam to drive a bottoming Rankine cycle.

1.4 The spiky central receiver air pre-heater (SCRAP)

The CR technology used to heat incoming air from the compressor would need to provide outlet temperatures of above 800 °C, while operating at a low pressure drop to reduce impact on the Brayton cycle efficiency. The **S**piky

Central **R**eceiver **A**ir **P**re-Heater (SCRAP), proposed by Kröger (2008), aims to address the problems faced in current compressed air CR technology. The SCRAP receiver uses "spikes" as tubular absorbers that protrude out from the center of the receiver as shown in Figure 1.4. The spike consists of two concentric tubes with a finned annulus. Compressed air enters the receiver's inner chamber through the central opening, where it travels through the inner tube of the spike. As the cold air exits the inner tube, it is diverted back through the irradiated outer tube and finally collected in the outer chamber of the receiver. The spike internal geometry as well as cross section is shown in Figure 1.5.

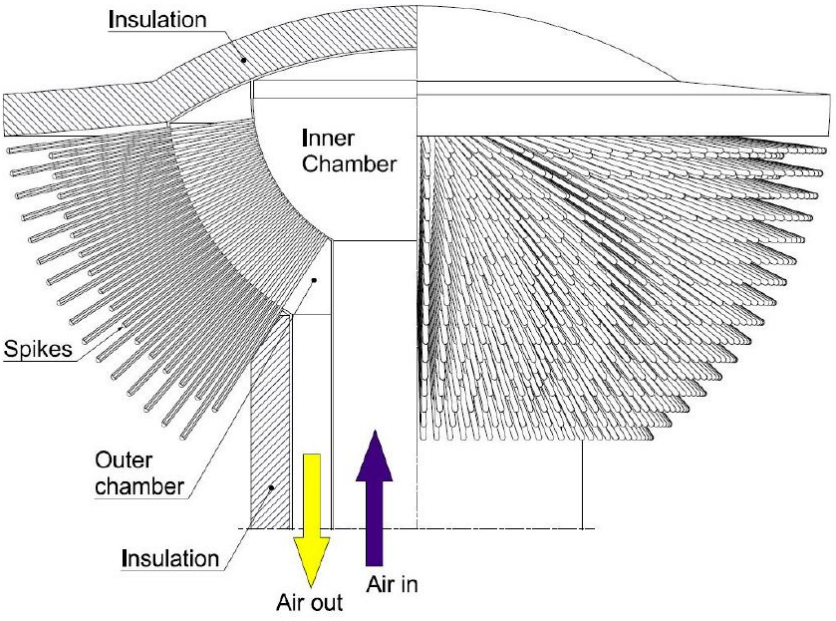

Figure 1.4: Possible layout of SCRAP receiver (Lubkoll *et al.*, 2015)

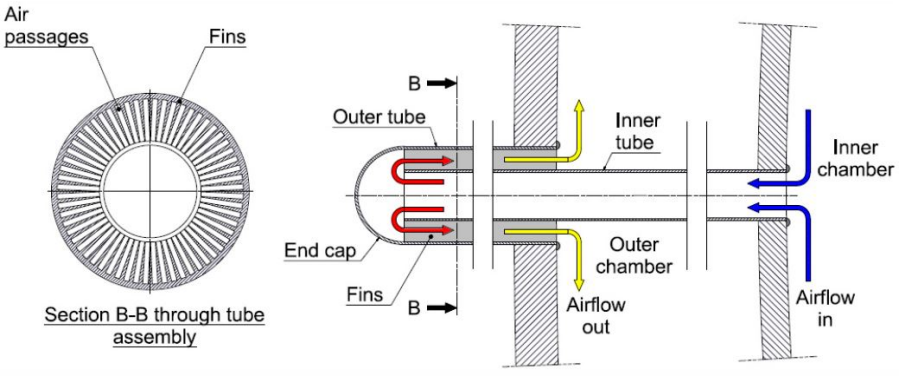

Figure 1.5: Spike internal geometry (Lubkoll *et al.*, 2015)

Incoming cold air is preheated by the exiting air and then further heated as it travels back through the outer tube. Solar irradiation on the base, depending on spike positioning, would also serve to heat the air. Due to the jet impingement cooling at the spike tip, the highest spike cooling is expected at the spike tip, which would avoid overheating of the spike section most readily exposed to solar irradiation.

The SCRAP receiver has been described as an external semi-volumetric tubular pressurized air receiver. This is because the spikes act as a porous surface, where the highest temperatures are expected at the base of the receiver and not the spike tips. Since the highest temperatures occur inside this porous structure with the lowest exposure to the surrounding environment, radiation losses are reduced substantially. Previous work conducted on the SCRAP receiver is discussed in Section 3.8.

Chapter 2

Research objectives and methodology

2.1 Problem statement

To date, several studies have been conducted to analyze aspects of the thermal performance of the SCRAP receiver. The receiver, or part thereof, has not been tested experimentally in conditions that might be close to the real operating conditions. This study aims to build on previous work through testing of a spike cluster in on-sun conditions. The data obtained through experimentation can be used in validating future simulations and development of the SCRAP receiver, should any be carried out.

2.2 Research objectives

The main research outcomes are formulated as;

- Gather experimental data of the performance of a single spike of the SCRAP receiver in on-sun conditions.
- Review existing pressurized air receiver technology and concepts in order to gain an understanding of factors which contribute to the successful operation of the receiver, as well as factors that led to the failure of previous receiver concepts.
- Characterize the solar irradiation distribution on the spike surface in on-sun conditions.
- Investigate the effect of the internal fins on total heat transfer in the spike.
- Predict the thermal performance of a full-length finned spike at conditions experienced during the experimental tests.

2.3 Research methodology

In order to provide suitable answers to the research questions, the methodology starts with the development of an experimental SCRAP receiver based on

previous research work. The experimental model would need to approximate a full-scale receiver, emulating the same convective shielding from, and view factors to the surrounding environment as might be expected in a full-scale receiver.

When developing the experimental receiver, the main driving factors are material availability and cost, manufacturing limitations and manufacturing time. Due to small expected testing windows during the project as a result of seasonal weather limitations, emphasis is placed on getting a receiver manufactured and installed in time to effectively utilize favorable weather conditions.

Based on previous experimental work carried out at the proposed testing facility, a suitable experimental setup is to be designed. The design would need to take into account availability and limitations of measuring instrumentation, while remaining inside the proposed project budget. To gauge the power output from the heliostat field, a field characterization analysis will also be required.

In order to characterize the irradiation distribution on the spike surface, an open annulus spike is to be used. The spike will have a bare surface to ensure minimal blocking of incoming radiation occurs. The spike will have thermocouples mounted along its length, which will need to be shielded from exposure to incoming radiation.

To investigate the effect of the internal fins on the total heat transfer in the spike, a second spike will be constructed from finned sections provided for the project, while maintaining the same overall dimensions of the reference spike. Temperature measurements will be taken at several depths into the fin at different locations on the spike circumference.

Due to potential instrumentation limitations, a 1-D numerical model based on existing theory is to be developed to gain a better understanding of the internal heat transfer characteristics in the receiver and to serve as a tool to predict the performance of a full length finned spike. The model would be verified through CFD analysis of discreet control volumes of the proposed spike configuration and validated using the obtained experimental data from the developed receiver. With this validated model, performance predictions can be made with conditions experienced during testing of the experimental receiver.

Chapter 3

Literature Study

This chapter gives an overview of what comprises a central receiver, its efficiency, the receiver type and absorber type. Different existing pressurized air receiver concepts are also discussed.

3.1 The Brayton cycle

From Çengel and Boles (2006), the ideal Brayton cycle, whose P-v and T-s diagrams are shown in Figure 3.1, consists of an isentropic compression stage across the compressor, followed by an isobaric heat addition stage. The high pressure, high temperature working fluid undergoes isentropic expansion in the turbine, resulting in power generation at the turbine output. The thermal efficiency relationship for the ideal Brayton cycle is given by

$$\eta_{th,Brayton} = 1 - \frac{1}{r_p^{\frac{(\gamma-1)}{\gamma}}} \tag{3.1}$$

where γ represents the fluid specific heat capacity ratio and r_p represents the gas turbine pressure ratio. From the given efficiency relationship, the ideal Brayton cycle thermal efficiency depends only on the turbine pressure ratio and the specific heat capacity ratio of the working fluid. The pressure ratio r_p may also be rewritten as

$$r_p = \left(\frac{T_3}{T_4}\right)^{\frac{\gamma}{(\gamma-1)}} \tag{3.2}$$

where T_3 and T_4 represent the turbine inlet and outlet temperatures respectively and where T_3 is the maximum temperature experienced in the Brayton cycle. T_3 or T_{max}, is largely limited by the temperatures which the turbine materials can withstand, which also limits the pressure ratios that can be used in the cycle. For a constant turbine inlet temperature, power output, w_{net} increases for increasing pressure ratios, reaching a maximum and then decreases. A balance is therefore required between thermal efficiency and power output.

One method of increasing gas turbine efficiency and therefore cycle efficiency is to increase the turbine inlet temperature. In this regard, CRs provide an excellent solution due to their ability to add heat to a pressurized fluid at nearly constant pressure. In integrating the Brayton cycle into large scale CSP power generation systems, the largest factor remains the ability to run a bottoming Rankine cycle (Basson, 2019).

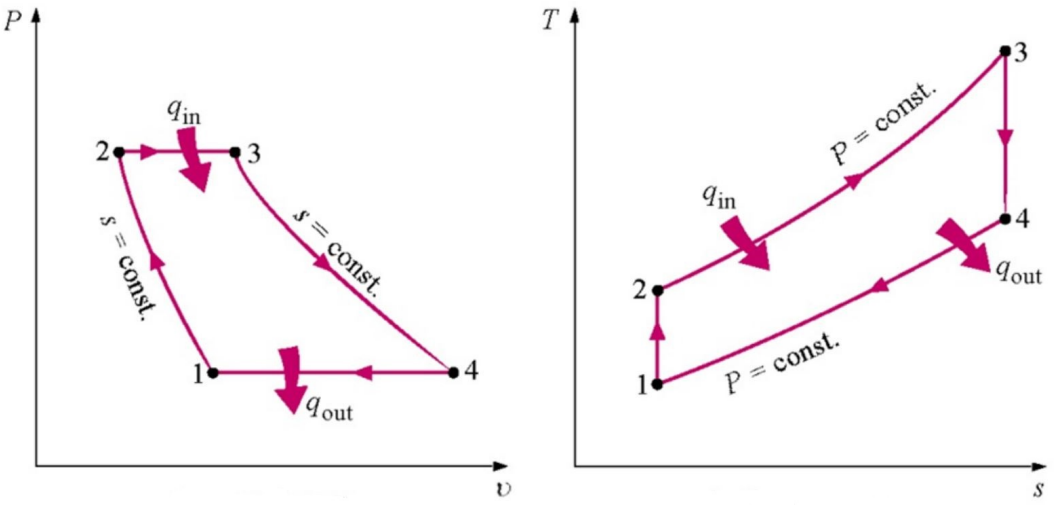

Figure 3.1: The ideal Brayton cycle (Çengel and Boles, 2006)

In order to obtain any economical power from the Rankine cycle, inlet temperatures in excess of 500 °C are required at the steam turbine inlet (Požívil *et al.*, 2014). To achieve these outlet temperatures from the Brayton cycle, gas turbine inlet temperatures of over 1000 °C are required (Allen, 2010). This high temperature requirement places severe stress on upstream components, calling for more temperature resistant materials and ultimately increasing the total cost of the system.

Another determining factor in increasing cycle efficiency is the pressure drop between the turbine and compressor. When using a central receiver to heat incoming turbine air, emphasis is placed on reducing the pressure drop across the receiver in order to maintain an efficient pressure ratio. The allowable pressure drop between the compressor and turbine stage for a solar receiver using air as HTF is typically between 20 kPa to 30 kPa (Heller, 2017). The pressure drop across the receiver remains a function of design geometry and care should be taken to avoid complexity which may hinder manufacturing practicality.

3.2 Receiver efficiency

Receiver efficiency may typically be defined as the product of all its individual contributors, where the individual efficiencies are based on receiver spillage, absorption, radiation, convection and conduction losses, respectively. The individual efficiencies have been summarized by Stine and Geyer (2001), where spillage and absorption are classified as optical losses and radiation, convection and conduction are classified as thermal losses.

Spillage losses are defined as the solar radiation directed at the receiver that does not directly fall on the receiver's absorbing area. Spillage is largely de-

termined by the implemented heliostat aiming strategy. When a more concentrated irradiation distribution is desired, radiation is confined to a small area with a small chance of spillage. The maximum allowable irradiation exposure on a receiver is typically dictated by the maximum working temperature of the construction materials used.

Conversely, if a more uniform distribution is desired, radiation is spread over a larger area with potential for increased spillage. Spillage losses on the receiver may be reduced by increasing the receiver aperture or area which absorbs solar radiation. Second to receiver geometry, the heliostat field also contributes to spillage losses insomuch as tracking accuracy of the heliostat field control system, mirror curve, mirror surface and beam spread.

Absorptive, or inversely, reflective loss is the solar radiation reflected away from the absorber due to the surface coating. Reflective losses may typically be mitigated by the application of a high absorptance paint with absorptance values of roughly 0.95.

Conduction losses arise from physical contact between the receiver and tower structure. Conduction losses typically make up the smallest contribution to overall losses and are mitigated by reducing attachment points and utilizing materials with low thermal conductivities for the mounting structure.

Arguably the most important losses experienced in a solar receiver are attributed to radiation and convection losses. These are primarily determined by the surrounding environment where radiation from the receiver as well as convective losses are a function of the difference between the receiver temperature and temperatures of the environment. Therefore, receiver surface exposure to the surrounding environment and operating temperature dictates the amount of radiative and convective losses experienced.

Considering the above mentioned factors determining receiver efficiency, a problem arises when it becomes difficult to compare efficiencies of receivers with different configurations. In such cases, the thermal efficiency, $\eta_{thermal}$, may also be used to evaluate receiver performance, as only the solar radiation input on the receiver aperture and energy output of the working fluid is accounted for (Lubkoll *et al.*, 2014). This definition does, however, pose some restrictions when the receiver aperture boundaries are not readily apparent.

3.3 Receiver configurations

Central receivers can typically be classified into two categories; external receivers and cavity receivers.

3.3.1 External receivers

External receivers, as shown in the example in Figure 3.2, are widely used due to their simplicity and low cost. Vertical tubes welded together form panels

that are arranged around the outside of the receiver to form a cylinder. HTF passes from a manifold at the bottom, through the tubes where the heated fluid is collected at the top. In a case where molten salt is used as HTF, the receiver may incorporate several tube passes to achieve the required HTF temperature. Depending on application, panels may be also be arranged on a flat panel for use with a polar heliostat field (Stine and Geyer, 2001).

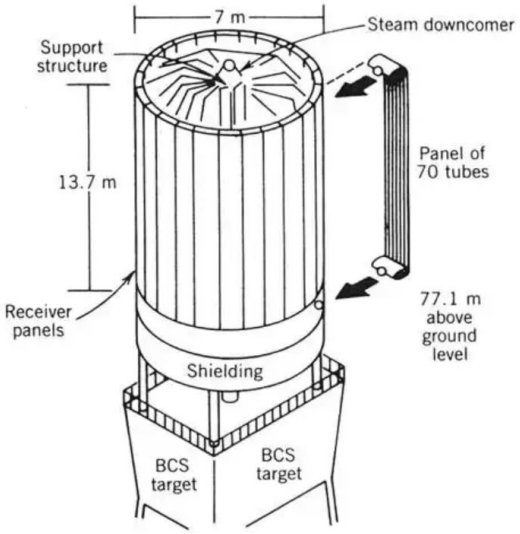

Figure 3.2: External receiver used for direct steam generation (Stine and Geyer, 2001)

Due to its large exposure to the environment, external receivers are highly susceptible to heat loss through convection and radiation. Surface area is therefore kept to a minimum to avoid these losses. External receivers typically do not function well for HTFs with low specific heat capacities as higher tube surface temperatures are required to obtain the same power output as for a high specific heat HTF. These higher temperatures necessarily lead to increased convective and radiative losses. As radiation is a function of T^4, radiative losses will dominate at higher temperatures (Stine and Geyer, 2001).

3.3.2 Cavity receivers

Cavity receivers, as shown in Figure 3.3, aim to reduce convective and radiative losses from the receiver by placing the absorber inside a cavity which protects it from the environment. Cavity receivers are typically better suited for use with HTFs with low specific heat capacities as much higher temperatures are attainable inside the receiver cavity with significantly lower heat loss (Heller, 2017).

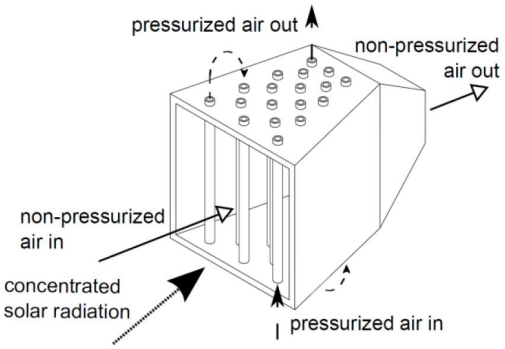

Figure 3.3: The HPAR receiver (Heller, 2017)

3.4 Absorber configurations

Central receiver absorber configurations can commonly be split into two categories; namely tubular and volumetric absorbers.

3.4.1 Tubular absorber

Tubular absorbers, as discussed in Section 3.3.1, are comprised of banks of parallel tubes which are exposed to solar irradiation. They are commonly used due to ease of manufacturing, availability and relatively low cost.

3.4.2 Volumetric absorber

Volumetric absorbers utilize a porous structure for the absorption of solar irradiation. The porous structure allows the radiation to penetrate into the absorber, where the heat is absorbed by the HTF which is pumped through the porous structure. The *volumetric effect* as described by Romero *et al.* (2002) dictates that the temperature of the HTF leaving the absorber is higher than the irradiated side of the absorber.

The radiative losses associated with volumetric absorbers are much lower than those of tubular absorbers as very little solar irradiation is reflected from the absorber surface. Due to the volumetric effect, the hottest part of the absorber is also shielded, which will further reduce convective and radiative losses. Figure 3.4 shows a comparison of the temperature profile along the radial axis for tubular and volumetric absorbers.

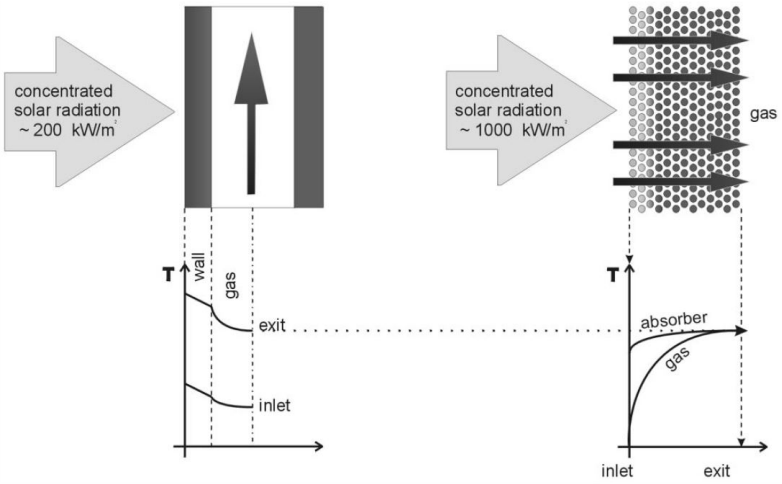

Figure 3.4: Temperature profile along the radial axis for tubular (left) and volumetric (right) absorbers (Romero *et al.*, 2002)

3.5 Receiver material considerations

While receiver topography and design ultimately determine the thermal efficiency and operational performance, the largest limitations are those posed by the construction materials. These limitations include the maximum operating temperature, thermal conductivity, resistance to thermal shock and inertness to oxidation (Požívil *et al.*, 2014).

In categorizing central receivers for specific applications; at temperatures below 800 °C, open loop receivers are used for Rankine cycle power generation or process heat. Here, some stainless steels are suitable but nickel-base super-alloys are preferred for their high temperature resistance and ability to form absorptive oxides. Above 800 °C, open loop receivers are used for indirect Brayton cycle power generation as well as process heat. Closed loop receivers have potential for a variety of uses, from direct Brayton cycle power generation to chemical processes. For these high temperatures, the most suitable materials are both oxide and non-oxide ceramics due to their high melting temperature of around 2000 °C. The main disadvantage is that they suffer from poor optical properties and therefore need to be treated to increase absorptivity (Freudenstein and Karnowsky, 1987).

Failure modes of the respective materials are also of concern. The higher ductility of stainless steels and nickel-base alloys allows for slower onset of failure. This provides some opportunity for mitigating catastrophic receiver failure as failure points may be identified when conducting routine inspection of receiver components. In contrast, due to the brittleness of ceramic materials they are more susceptible to rapid onset failure, or more simply - cracking. As such, steps may be required, depending on receiver geometry, to ensure that

broken absorber components do not damage neighboring components, which may lead to cascade failure of the receiver's internal or external structure (Avila-Marin, 2011).

3.6 Volumetric cavity receiver concepts to date

To date, several volumetric cavity receiver concepts have been explored with varying levels of success. The primary contributors to the development of these receivers have been the Weizmann Institute of Science (WIS) and the German Aerospace Center (DLR).

3.6.1 DIAPR

The Directly Irradiated Annular Pressurized Receiver (DIAPR), shown in Figure 3.5a, developed by the WIS, was initially implemented in the DIAPR project in 1992. The DIAPR's performance was attributed to two components: A *Porcupine* volumetric absorber and a *Frustum-like high pressure* fused silica window (FLHIP). The porcupine, made from alumina-silica pins, functions as a volumetric absorber, transferring heat to the incoming air. The FLIHP separates the absorber from the environment, allowing high temperature operation by admitting solar irradiation and reducing convective losses.

Solar tests were conducted on the DIAPR for over 100 h. Contamination from dirt and ceramic insulation was found to settle on the window surface, increasing the window temperature. This heating was negligible and did not significantly increase radiative losses or create failure-inducing hotspots. The DIAPR achieved thermal efficiencies in the range of 70 % to 90 % with an air outlet temperature range of 870 °C to 1200 °C. Operating pressures also ranged from 1700 kPa to 2000 kPa (Kribus *et al.*, 2001).

3.6.2 DIAPR multistage

In an attempt to reduce thermal losses, a second, multi-stage receiver was also designed by WIS in 1996, shown in Figure 3.5b. The working fluid was pre-heated through tubular cavity receivers made from Inconel 600, situated around the main aperture. The pre-heater locations were matched to the heliostat field, with the intention of absorbing lower solar radiation around the high temperature stage.

The working fluid was split so that air could also be blown over the quartz window while the receiver was in operation. The secondary air stream was passed through the pre-heaters, exiting at roughly 700 °C before entering the high temperature DIAPR stage. Solar testing was conducted for over 40 h, with maximum outlet temperatures reaching 1000 °C at operating pressures of 1600 kPa to 1900 kPa (Avila-Marin, 2011).

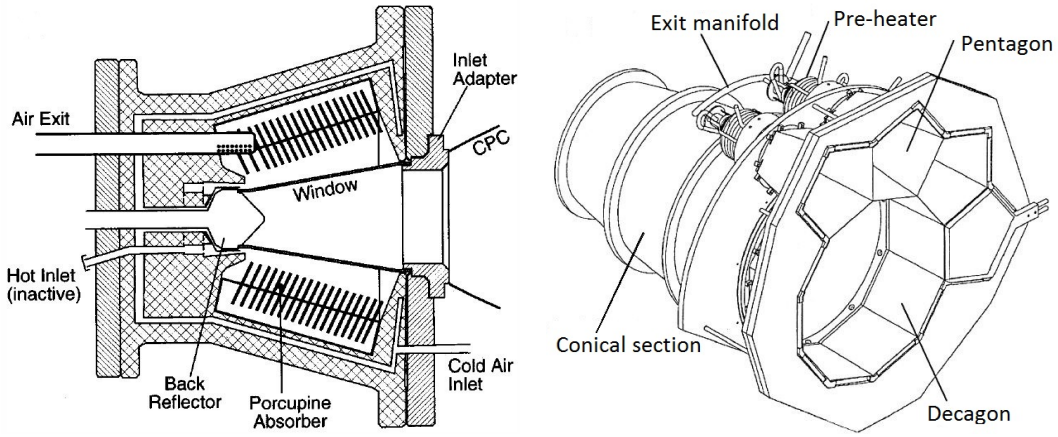

(a) The DIAPR receiver (Kribus *et al.*, 2001)

(b) The DIAPR multistage receiver (Kribus *et al.*, 1999)

Figure 3.5: Volumetric cavity receivers developed by WIS

3.6.3 REFOS

The REFOS receiver, shown in Figure 3.6, was developed by the DLR in 1996.

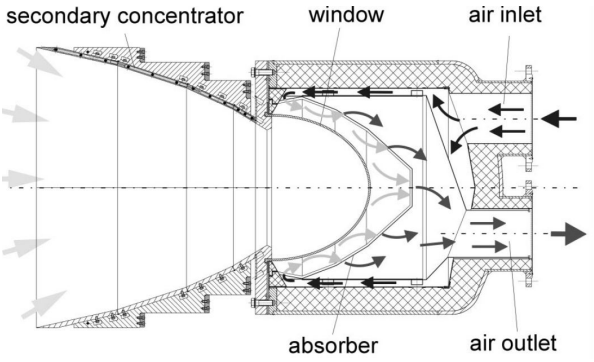

Figure 3.6: The REFOS receiver (Buck *et al.*, 2002)

A volumetric absorber, consisting of multiple layers of heat resistant wire screens is installed inside an internally insulated pressure vessel. An inverted dome shaped quartz window separates the absorber from the environment and admits solar radiation to the absorber. A secondary concentrator mounted on the outside of the absorber serves to concentrate incoming solar radiation, reflecting it towards the quartz window. A reported thermal efficiency of 78 % was achieved with an air outlet temperature of 1030 °C (Buck *et al.*, 2002).

After an operating time of 500 h at air temperatures between 600 °C to 800 °C, observations reported several problems with the quartz glass of the dome shaped window. Surface contamination had burned into the glass, increasing absorptivity and therefore resulting in higher temperatures in the

quartz window. The higher temperatures also served to propagate cracking of microscopic manufacturing defects with thermal cycling (Lubkoll *et al.*, 2014).

3.6.4 ALSTOM

The ALSTOM receiver, shown in Figure 3.7, is currently under development at ETH Zürich. The proposed design features a silicon carbide annular Reticulated Porous Ceramic (RPC) foam, held between two concentric cylinders.

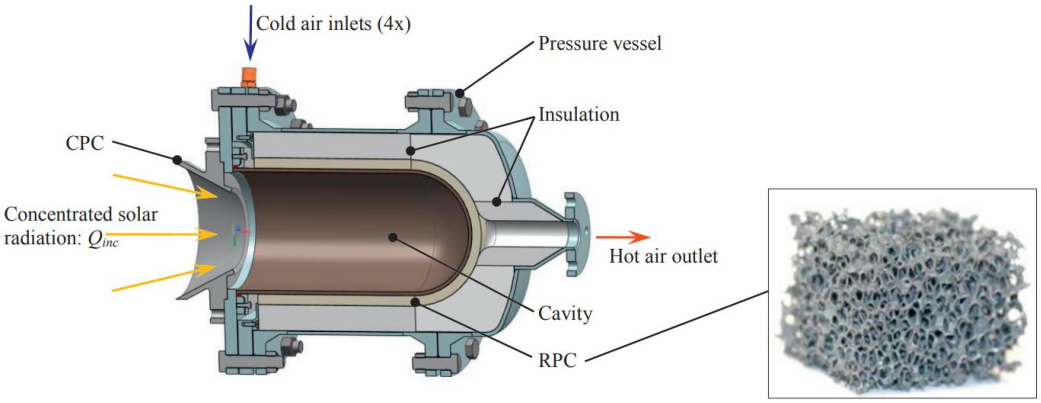

Figure 3.7: The ALSTOM receiver (Požívil *et al.*, 2014)

A compound parabolic concentrator at the aperture intends to concentrate solar radiation onto the silicon carbide inner cavity, while reducing aperture size and radiation losses. Pressurized air moves through the RPC foam, which is heated through conduction from the inner cavity. Peak operating efficiencies of 77% were obtained for air outlet temperatures of 553 °C, while operating at 500 kPa. An optimized design is expected to deliver operating efficiencies of up to 90% with air outlet temperatures of 700 °C (Požívil *et al.*, 2014).

3.7 Tubular cavity receiver concepts to date

The SOlar HYbrid power and COgeneration (SOLHYCO) and SOLar Up-scale GAS (SOLUGAS) receivers were developed from 2006 and 2008 respectively by DLR and Abengoa Solar, along with several others.

3.7.1 SOLHYCO

The SOLHYCO receiver, shown in Figure 3.8a, was to serve as a pre-heating stage for a micro turbine. The tubular absorber consisted of 40 tubes made from three-layer Inconel-Copper-Inconel pipes, which were mounted in a cone formation inside the receiver cavity box. Air enters the tubes from the toroidal

distributor, heating up as it travels through the tubes and then passing into the collector. At its design point of 800 °C outlet air temperature, the receiver was predicted to operate at a thermal efficiency of 77.7 %. The receiver was tested over a period of 100 hours of solar operation. The predicted accuracy could not be verified as cracking in the three layer pipe led to extensive heat leaks inside the receiver cavity box (Amsbeck *et al.*, 2008).

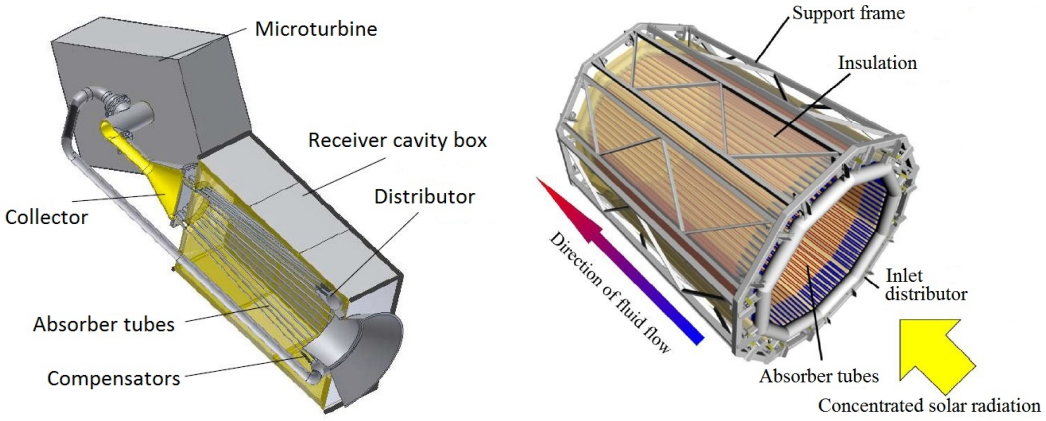

(a) The SOLHYCO receiver (Amsbeck *et al.*, 2008)

(b) The SOLUGAS receiver (Korzynietz *et al.*, 2016)

Figure 3.8: Tubular cavity receivers developed by DLR, Abengoa Solar and several others

3.7.2 SOLUGAS

The SOLUGAS receiver, shown in Figure 3.8b, was to be implemented as a turbine pre-heater for combined cycle power generation. The receiver consisted of 10 tubular absorber panels, with 17 tubes per panel, arranged inside a support frame. The absorber panels were covered with insulation to minimize heat losses from the outer side of the receiver. The tubes were made of Inconel 617, while the inlet distributor was made of stainless steel. Test results show that the receiver achieved a thermal efficiency of 78 % at an outlet temperature of 794 °C. The pressure drop across the receiver was measured at around 20 kPa (Korzynietz *et al.*, 2016).

3.7.3 Coiled tube pressurized air receiver

Another novel coiled tube pressurized air receiver is currently under development at the Key Laboratory of Solar Thermal Energy and Photovoltaic Systems at the Chinese Academy of Sciences. The receiver, shown in Figure 3.9, features a double-spiral tubular absorber shaped into a conical form. The spiral tubes are constructed from stainless steel 310s tube with a 4 mm

inner diameter and a 2 mm wall thickness. By incorporating two flow channels, the flow resistance through the tubes is reduced, as opposed to a single channel coil for the same aperture. It was found that due to the minimum bending radius of the tubes, an opening of 60 mm diameter results at the rear of the conical tube assembly, leading to less exposure of the tubular absorber to incident radiation. The receiver was found to reach air outlet temperatures of 787 °C while operating at a thermal efficiency of 53% and a pressure drop across the receiver of 170 kPa (Chu *et al.*, 2018).

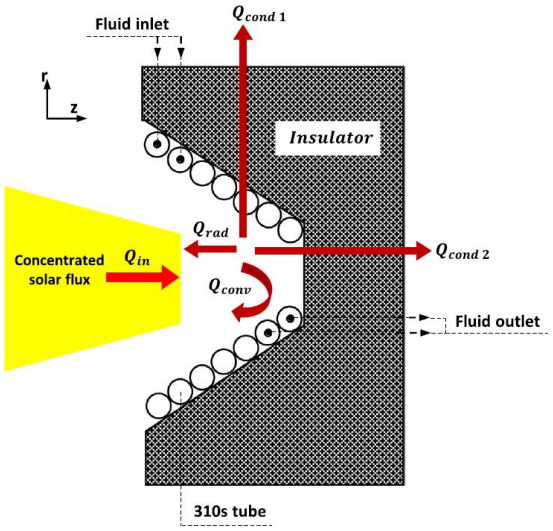

Figure 3.9: Coiled tubular pressurized air receiver (Chu *et al.*, 2018)

3.8 Previous work conducted on the SCRAP receiver

An initial study was conducted by Lubkoll (2017) to develop an understanding of the performance of the SCRAP receiver. The study begins with a ray tracing analysis on a proposed reference receiver geometry, given in Table 3.1, to determine the effects of heliostat field design on the receiver performance. The analysis found that smaller facets produce a more uniform irradiation distribution on the spike with a higher penetration depth . Larger facets led to a higher irradiation concentration at the front of the spike with a lower penetration depth. The analysis also indicated that some energy misses the spike, impinging on the sphere surface. The three cases with different heliostat sizes are presented in Figure 3.10, where all cases exhibit equal energy absorption, within 1.5 %.

Table 3.1: Reference SCRAP receiver geometry (Lubkoll, 2017)

Parameter	Value
Sphere radius	2 m
Spike radius	0.035 m
Spike length	1.0 m to 1.3 m
Tower height	82 m
Spike root spacing	18 mm
Total spikes	496

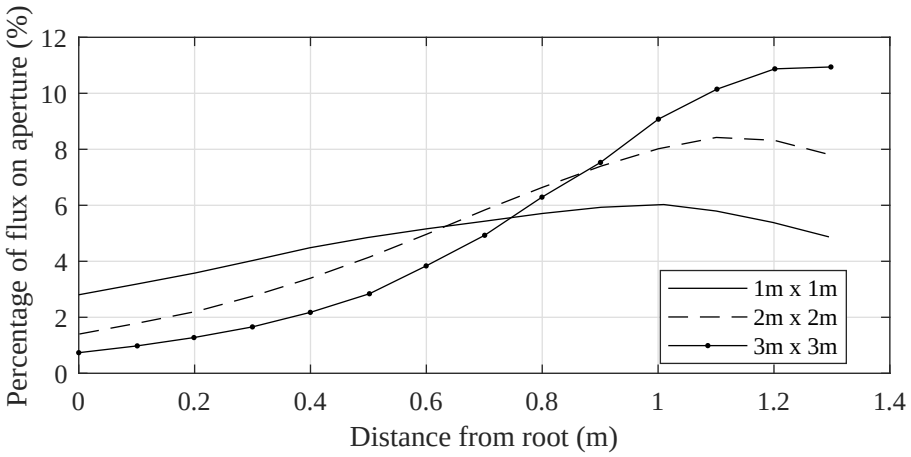

Figure 3.10: Irradiation distribution along spike length (Lubkoll, 2017)

Following the ray tracing analysis, a numerical model was developed to investigate the receiver performance under design conditions. The model was complemented by the development and construction of a laboratory test setup, utilizing steam heating at 100 °C, which would be used to validate the internal heat transfer and air-flow models. A fin geometry similar to that shown in Figure 1.5 was employed, albeit with a smaller number of fins. Spike test sections were manufactured through wire cutting, which allowed for 24 rectangular straight ducts. Good agreement was found between the model predictions and test setup for different air flow rates under laboratory conditions. The validated model predicted that the receiver may operate at thermal efficiencies of 79 % to 85 % with respective air outlet temperatures of 768 °C to 801 °C, where ambient cross wind speed increases from 0 m/s to 5 m/s. Low radiative heat losses were reported due to the dense geometric spacing, however, the receiver would be vulnerable to convective losses due to the large exposed surface area.

Three different irradiation distributions were considered, namely a uniform profile and two linear profiles, with maximum solar irradiation occurring at the

root and tip, respectively. The analysis showed that the peak irradiation locations define the regions with strongest heating caused by the high air-metal differential temperature. For the case with a high irradiation concentration towards the tip, increased losses are experienced due to exposure of high temperature surfaces to the environment. Conversely, for the case with a high irradiation concentration towards the root, the volumetric effect is better utilized, reducing exposure of high temperature surfaces to the environment and decreasing losses. In all cases, the highest material temperatures are experienced at the spike tip which is the most exposed part of the receiver structure. Following high tip temperatures, high root temperatures are also observed due to the reduced interaction with the environment.

Several recommendations were proposed with regard to further work on the SCRAP receiver. First, in an effort to further enhance cooling at the spike tip, Lubkoll (2017) suggested the implementation of jet impingement cooling from the inner tube, whereby a nozzle serves to decrease the flow area and increase air velocity. This was further explored in a CFD study by McDougall (2019). It was found that a nozzle was necessary to achieve sufficient cooling at the tip. A parametric analysis indicated that the nozzle diameter was the most sensitive geometric parameter determining the overall pressure drop across the spike and tip heat transfer capabilities. By decreasing the nozzle diameter, a drastic pressure drop is induced with the benefit of a significant increase in heat transfer.

Another suggestion was the use of helically swirled fins inside the spike annulus instead of straight fins. The proposed benefits include the improvement of heat transfer by inducing secondary air flow patterns as well as allowing the flow stream to pass circumferential positions several times. The latter would mitigate the effects of non-uniform irradiation distribution. It is thought that hotspots caused by non-uniform irradiation distributions will lead to higher heating in some ducts and a subsequent higher pressure drop. This would induce a runaway problem where air increasingly passes through colder ducts, allowing the hot side to further overheat.

The concept of helically swirled fins was further investigated by Grobbelaar (2019). Spike sections manufactured through selective laser sintering and featuring 24 rectangular helically swirled ducts were investigated for heat transfer and pressure drop characteristics. The results were compared to existing empirical correlations as well as a developed CFD model. Experimental and CFD results generally showed good agreement, while empirical correlations were seen to predict heat transfer coefficients with a maximum error of 14 % and pressure drop with a maximum error of 12%. It was found that the helical configuration could increase the average heat transfer coefficient in the ducts by 21% to 29%. The helical configuration also induced a significant increase in pressure drop ranging from 8% to 300% for the respective heat transfer coefficient gains.

3.9 Conclusion on literature review

The literature review investigated the concept a central receiver. Several notable pressurized air receiver concepts that have been explored to date were discussed. From these receivers, the conclusion can be drawn that design simplicity is a strong indication of the long-term operational success of a central receiver. In the case of the discussed volumetric cavity receivers, the more complex inverted dome shaped quartz window of the REFOS receiver induced failure where the FLHIP of the DIAPR receiver did not. Similarly, the three layer pipe utilized in the SOLHYCO receiver also induced failure where the comparative layout of the SOLUGAS receiver operated successfully. In some cases, the degree of design complexity also calls for more "exotic" materials, which would increase the total receiver cost.

Previous work conducted on the SCRAP receiver was also investigated. From the previous work it can be concluded that the SCRAP receiver shows potential for implementation into a solarized Brayton cycle. This is, however, conditional on several factors, primarily the final air outlet temperatures attainable with a given spike geometry and how the spike geometry influences the overall receiver cost. Mitigating steps such as coiled fins and jet impingement tip cooling would also be required to reduce maximum material temperatures to prevent failure, which would have deleterious effects on the total pressure drop across the receiver.

Chapter 4

Theory and modelling

In order to gain a better understanding of the heat transfer mechanisms involved in the SCRAP spike, a 1-D numerical model was developed. The model would lend insight into the thermal performance of the spike under different irradiation exposure and flow conditions. The model would also serve as a platform to compare the effect of the proposed finned annulus on thermal performance, as opposed to an open annulus.

4.1 Model topography

The spike is split into three sections, namely the inner tube, spike tip and open annulus. Figure 4.3 shows the topography for the reference open annulus spike. The inner tube and open annulus are divided into n discreet control volumes. The subscripts i and o denote inner and outer control volume, respectively. General dimensions are provided in Figure 4.2.

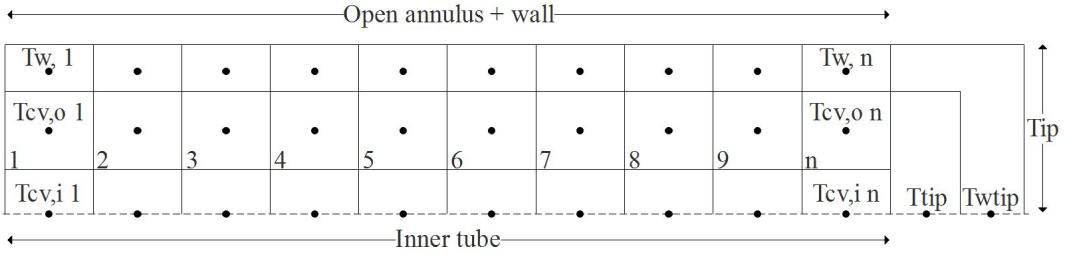

Figure 4.1: Open annulus spike topography

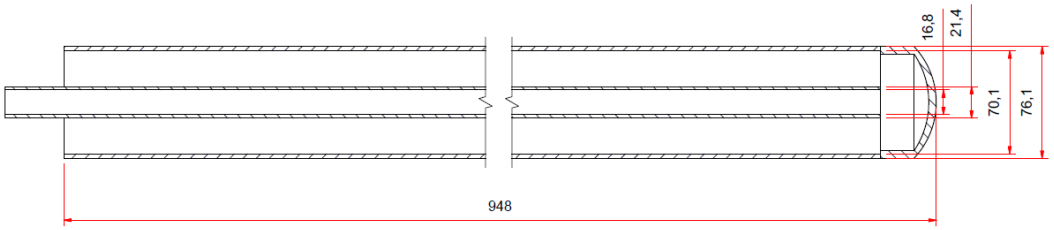

Figure 4.2: Open annulus spike dimensions

Figure 4.3 shows the alternative model topography for the mixed annulus spike. As two 200 mm finned sections were provided for this project, the spike

would be composed of a 400 mm finned annulus section towards the front and an open annulus section towards the rear to make up the remaining length of the spike. General dimensions are provided in Figure 4.4.

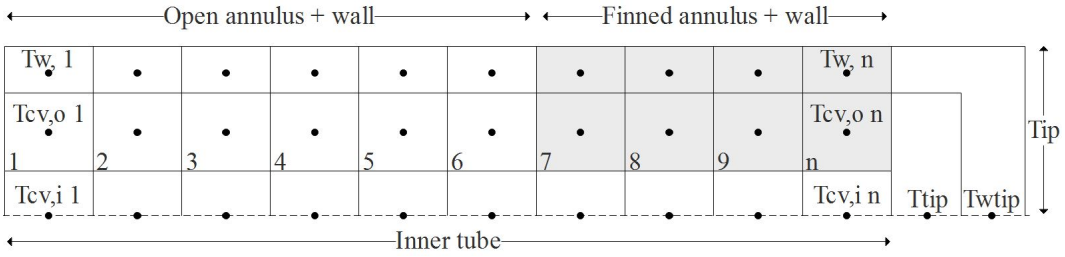

Figure 4.3: Mixed annulus spike topography

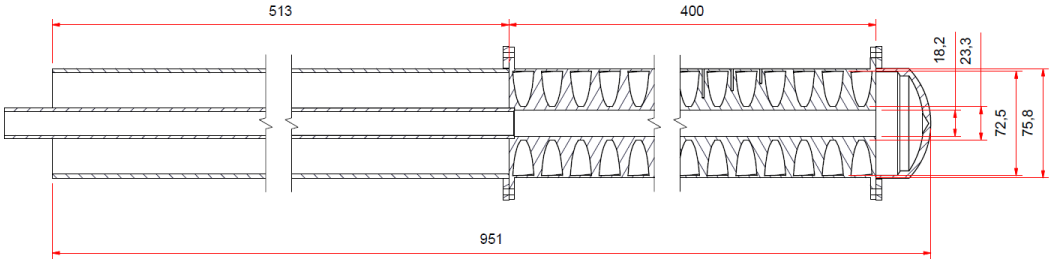

Figure 4.4: Mixed annulus spike dimensions

The numerical model uses an explicit formulation to solve for the control volume and wall temperatures. An explicit formulation is chosen over an implicit formulation primarily for its relative simplicity and ease of implementation. Since an explicit formulation is only conditionally stable, the time step size is determined from the stability criterion:$(\Delta t/\Delta x^2) \leq 0.5$, where Δx is the control volume size. Since the internal flow is strongly convective and moves in one direction only, a 1$^{\text{st}}$-order upwind discretization scheme is used to calculate control volume air temperatures. A 1$^{\text{st}}$-order upwind scheme is chosen for its stability as well as its ability to yield physically realistic solutions (Versteeg and Malalasekera, 2007). Air properties are calculated at the node temperatures and all properties except density are temperature, but not pressure, dependent. Density is calculated from the ideal gas law. Polynomial regression data used to calculate the thermal properties of air and steel are given in Appendix F. Successive control volume temperatures are calculated by the governing equation

$$T_{cv,n}^{t+\Delta t} = T_{cv,n}^{t} + \frac{\Delta t \dot{m}}{c_{p,cv} m_{cv}} (c_p T_{cv}^{t}|_{n-1} - c_p T_{cv}^{t}|_{n}) + \frac{\Delta t \dot{Q}}{c_{p,cv} m_{cv}} \text{ [°C]} \quad (4.1)$$

The spike wall control elements interact with the surrounding environment as well as neighboring elements. Therefore, when calculating the conduction heat transfer between wall elements, a central differencing scheme is used. The spike wall temperatures are calculated by the governing equation

$$T_{w,n}^{t+\Delta t} = T_{w,n}^{t} + \frac{\Delta t \dot{Q}}{c_{p,w} m_w} \qquad [^\circ\text{C}] \quad (4.2)$$

In both the above governing equations, $\dot{Q}$ denotes the total heat transfer to the control elements or volumes. The heat transfer mechanisms involved for interacting control elements and volumes are illustrated in Figure 4.5.

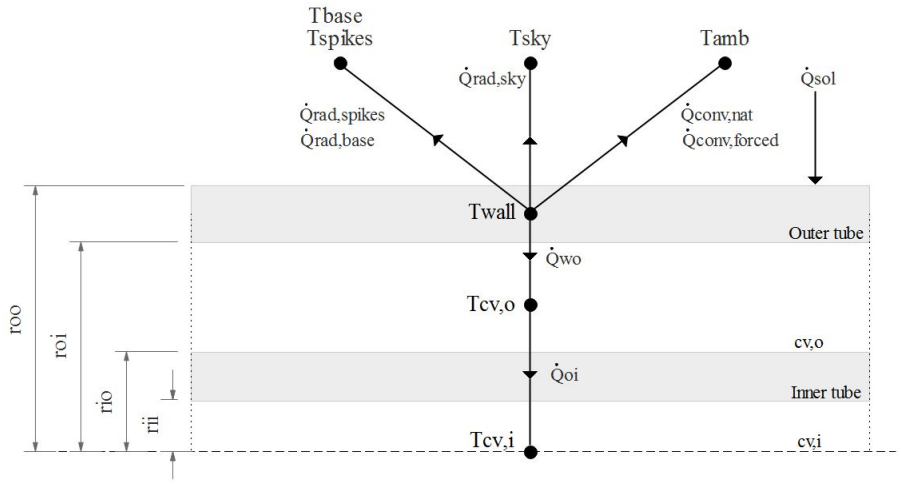

Figure 4.5: Thermal network for interacting control volumes

At the spike surface, the control element first receives solar irradiation from the heliostat field. The control element is subject to both natural and forced convection heat transfer to the surrounding environment, driven by the ambient air temperature, T_{amb}. There is a radiation heat loss to the surrounding environment, driven by T_{sky}. A radiation interaction occurs between the control element and both the surrounding spikes and the receiver base with temperatures T_{spikes} and T_{base}, respectively. Finally, convection heat transfer occurs between the wall element and the outer control volume element. To simplify the numerical model, a radially uniform wall temperature is assumed.

At the outer control volume, the air experiences convective heat transfer from the wall element and convective heat transfer to the inner control volume through the inner tube wall. The inner control volume experiences only convective heat transfer from the outer control volume through the inner tube wall. Since the inner tube is reasonably thin and air mass flow through the inner tube is expected to be high, it is assumed that heat transfer coefficients at the inner tube inner wall will also be high and that subsequently, the inner tube wall temperature would approximate the inner tube air temperature. The

inner tube wall is therefore not modelled explicitly but its thermal resistance is included, given as

$$R_{cond,oi} = \frac{ln(r_{io}/r_{ii})}{2\pi k} \quad \text{[K/W]} \quad (4.3)$$

For the finned annulus outer control volumes, a similar approach is used. Figure 4.6 gives the general dimensions of the finned spike section and illustrates the discretization of the outer control volume and wall. At the wall, all heat transfer mechanism to the surrounding environment applies. As the finned sections are symmetrical, only a single duct is modelled as shown in Figure 4.6b.

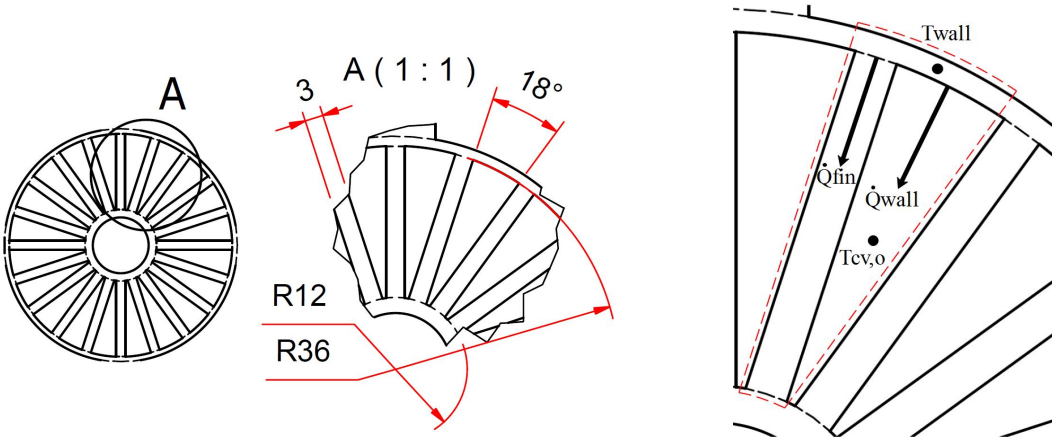

(a) Finned annulus layout (b) Duct discretization

Figure 4.6: Duct topography

The fins are coupled to the spike wall and the assumption is made that the fin tip approximates the same temperature as the inner tube. For a fin with a specified fin tip temperature, the heat transfer to the air is calculated from (Çengel and Ghajar, 2015)

$$\begin{aligned}\dot{Q}_{fin} =& \sqrt{h_{avg} p A_c}(T_w - T_{cv,o}) \\ &\times \frac{\cosh(mr_f) - [(T_{cv,i} - T_{cv,o})/(T_w - T_{cv,o})]}{\sinh(mr_f)} \quad \text{[W]} \quad (4.4)\end{aligned}$$

where

$$m = \sqrt{\frac{2h_{avg}}{k_f t_f}} \quad (4.5)$$

and r_f, t_f and k_f are the the fin height, thickness and thermal conductivity, respectively. p and A_c denote the fin perimeter and cross-sectional area,

respectively. The thermal conductivity of the finned sections is taken from the manufacturer datasheet as 20 W/mK for CL 50WS hot-work steel. At the fin root, the arc length between adjacent fins is roughly equal to 0.66 mm. Compared to the remaining heat transfer surface area, the contact area at the inner tube outer wall can be assumed to be negligibly small. It is then also assumed that convection heat transfer from the outer control volume to the inner control volume through the inner tube wall would also be negligibly small.

4.2 Velocity and pressure

To calculate the air pressure drop inside the spike, the principle of momentum conservation is used. The momentum conservation principle for a stationary control volume, as shown in Figure 4.7, in the x-direction can be expressed as

$$\rho\frac{\delta U}{\delta t} = \left\{\begin{matrix}\text{Momentum flux at the}\\ \text{control volume faces}\end{matrix}\right\} + \left\{\begin{matrix}\text{Sum of forces acting}\\ \text{on the control volume}\end{matrix}\right\} \tag{4.6}$$

where the first term denotes the rate of momentum accumulation in the control volume.

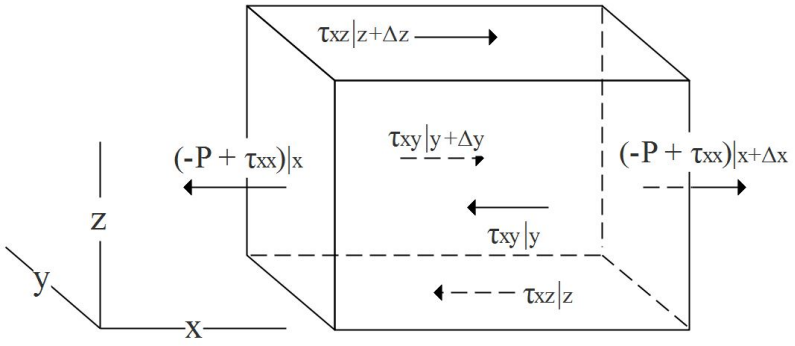

Figure 4.7: Stationary control volume subject to pressure and shear forces

Conducting a momentum balance over the control volume in Figure 4.7 gives

$$\begin{aligned}\Delta x\Delta y\Delta z\rho\frac{\delta U}{\delta t} &= \Delta y\Delta z(\rho UU|_x - \rho UU|_{x+\Delta x}) + \Delta x\Delta z(\rho UV|_y - \rho UV|_{y+\Delta y})\\ &+ \Delta x\Delta y(\rho UW|_z - \rho UW|_{z+\Delta z})\\ &+ \Delta y\Delta z((-P+\tau_{xx})|_{x+\Delta x} - (-P+\tau_{xx})|_x)\\ &+ \Delta x\Delta z(\tau_{xy}|_{y+\Delta y} - \tau_{xy}|_y) + \Delta x\Delta y(\tau_{xz}|_{z+\Delta z} - \tau_{xz}|_z)\end{aligned} \tag{4.7}$$

For a steady flow, where no mass transfer across the y and z faces occurs, the momentum balance can be simplified to

$$\Delta z(\rho UU|_{x+\Delta x} - \rho UU|_x) = \Delta z(P|_x - P|_{x+\Delta x}) + \Delta x(\tau_{xz}|_{z+\Delta z} - \tau_{xz}|_z) \quad (4.8)$$

Substituting $\pi D_h \Delta x$ and $\pi D_h^2/4$ for the surface and flow areas, Δx and Δz, gives

$$(\rho UU|_{x+\Delta x} - \rho UU|_x) = (P|_x - P|_{x+\Delta x}) + \frac{4\Delta x}{D_h}(\tau_{xz}|_{z+\Delta z} - \tau_{xz}|_z) \quad (4.9)$$

where D_h is the hydraulic diameter. Rearranging and applying upwind discretization gives an equation for pressure drop per unit flow length

$$(P|_n - P|_{n-1}) = (\rho UU|_n - \rho UU|_{n-1}) - \frac{4\Delta x}{D_h}(\tau_{xz}|_{\Delta z}) \text{ [Pa]} \quad (4.10)$$

where shear stress, τ is given by

$$\tau = \frac{C_f}{2}\rho U^2 = \frac{f}{8}\rho U^2 \quad \text{[Pa]} \quad (4.11)$$

and bulk fluid velocity, U, is calculated as

$$U = \frac{\dot{m}}{\rho A} \quad \text{[m/s]} \quad (4.12)$$

At the spike tip where air flow turns through 180°, the same formulation is used without the shear stress term. The resulting pressure drop at the spike tip is caused by both the change in flow area as well as the change in flow direction.

At the spike outlet, a pressure drop is induced due to the sudden expansion when travelling from the spike to the air manifold. Similarly, a pressure drop is induced by the sudden contraction when the air flows from the air manifold into the exhaust. As the flow travels through the exhaust, a further friction induced pressure drop is also observed. Finally, as the air exits the exhaust and is vented to atmosphere, a sudden expansion pressure drop is induced. The spike outlet, exhaust inlet and exhaust outlet is, in this case, characterized as a sharp-edged pipe outlet and inlet with loss coefficients of $K_{L,se} = 1.05$ and $K_{L,sc} = 0.5$, respectively (Çengel and Cimbala, 2014). The corresponding total pressure drop from the spike outlet to exhaust outlet can be calculated as

$$\Delta P = K_{L,se}\left(\frac{\rho U_b^2}{2}|_{so} + \frac{\rho U_b^2}{2}|_{eo}\right) + K_{L,sc}\frac{\rho U_b^2}{2}|_{ei} + \frac{f\rho U_b^2}{4D_h}L_{ex}|_{ei} \text{[Pa]} \quad (4.13)$$

where the subscripts *so*, *ei* and *ex* denote "spike outlet", "exhaust inlet" and "exhaust", respectively. A boundary condition of 101.3 kPa is set at the exhaust outlet.

4.3 Internal convection heat transfer

In this section, the selection of the friction factor correlations and Nusselt number correlations used to calculate the pressure drop and forced convection heat transfer coefficients inside the spike are discussed. The forced convection heat transfer is calculated from *Newton's law of cooling*, given by

$$\dot{q}_{conv} = h(T_1 - T_2) \tag{4.14}$$

where $T_1 - T_2$ denotes the temperature difference between participating media. The relation between heat transfer coefficient and Nusselt number is given by

$$Nu = \frac{hD_h}{k} \tag{4.15}$$

where D_h denotes the hydraulic diameter of the particular flow area and k is the fluid thermal conductivity. The implementation of the friction factor and Nusselt number correlations was verified through CFD modelling of discrete flow sections, presented in Appendix B.

4.3.1 Inner tube

To date, turbulent flow in circular tubes has been studied in depth and several correlations for friction factor and Nusselt number have been developed. Some of these correlations have also been developed from experimental data, leading to a high degree of suitability for other practical applications. To calculate the friction factor through the inner tube, the assumption of a smooth wall is made. The *first Petukhov equation* (Petukhov, 1970), valid for $3000 < Re < 5 \times 10^6$, can be used to calculate friction factor, given as

$$f_{ii} = [0.790 \ln(Re_D) - 1.64]^{-2} \tag{4.16}$$

The internal heat transfer Nusselt number is calculated using the *second Petukhov equation* as modified by Gnielinski (Gnielinski, 1976) which produces accurate results for $3000 < Re < 5 \times 10^6$ and $0.5 < Pr < 2000$, given as

$$Nu_{ii} = \frac{(f/8)(Re_D - 1000)Pr}{1 + 12.7(\frac{f}{8})^{1/2}(Pr^{\frac{2}{3}} - 1)} \tag{4.17}$$

4.3.2 Open annulus

Since the geometry and flow through the open annulus varies somewhat from that of the inner tube, Nusselt number correlations for circular tubes cannot be directly applied to calculate the Nusselt number for flow in concentric annuli. Work done by Dirker and Meyer (2004), along with several other studies

by the same authors on the same topic, developed a set of Nusselt number correlations for flow through concentric annuli. The correlations were developed experimentally using several different geometries and verified through CFD modelling. The process used to calculate the Nusselt number at the inner tube outer wall and the outer tube inner wall is followed as set out in Dirker and Meyer (2004). The hydraulic diameter of the open annulus is calculated as

$$D_h = \frac{4A_c}{p} = \frac{4\pi(D_o^2 - D_i^2)/4}{\pi(D_o + D_i)} = D_o - D_i \qquad \text{[m]} \quad (4.18)$$

For the friction factor in the open annulus, the *first Petukhov equation* (Petukhov, 1970) given in Equation (4.16) is also suitable. The inner and outer surface Nusselt numbers are calculated using the experimental correlations where the inner and outer Nusselt numbers are calculated from

$$Nu_{io} = C_i Re_{i,D_h}^{0.8} Pr_i^{\frac{1}{3}} \left(\frac{\mu}{\mu_w}\right)_i^{0.14} \quad (4.19)$$

$$Nu_{oi} = C_o Re_{o,D_h}^{B} Pr_o^{\frac{1}{3}} \left(\frac{\mu}{\mu_w}\right)_o^{0.14} \quad (4.20)$$

where $C_i = 0.027$. B and C_o are given by

$$B = 1.013e^{-0.067a} \quad (4.21)$$

and

$$C_o = \frac{0.003a^{1.86}}{0.063a^3 - 0.674a^2 + 2.225a - 1.1557} \quad (4.22)$$

where a represents the annular diameter ratio. The presented correlations are accurate for $4000 < Re < 30000$ and $1.7 < a < 3.2$.

4.3.3 Finned annulus

Work conducted by Grobbelaar (2019) sought to investigate the effect of coiled ducts on heat transfer and pressure drop through rectangular duct spike sections. Several empirical correlations were compared to a CFD model as well as experimental results from a manufactured test section. From the empirical correlations, it was found that the correlations for friction factor and Nusselt number developed by Kakaç *et al.* (1987) gave the most accurate results, with maximum deviations of roughly 10%. The correlations for friction factor and Nusselt number as developed by Kakaç *et al.* (1987) is therefore used for the finned annulus. The developed correlations rely on modification of the existing *first Petukhov equation* and *Dittus-Boelter equation*.

The hydraulic diameter of a duct in the finned annulus is calculated from

$$D_h = \frac{4A_c}{p} \quad [\text{m}] \quad (4.23)$$

where the flow area and perimeter are given by Equation 4.24 and Equation 4.25, respectively.

$$A_{duct} = \frac{\pi(r_{oi}^2 - r_{io}^2) - n_{duct}(r_{oi} - r_{io})t_{duct}}{n_{duct}} \quad [\text{m}^2] \quad (4.24)$$

$$p_{duct} = \frac{2\pi r_{oi} - n_{duct}t_{duct}}{n_{duct}} + 2(r_{oi} - r_{io}) \quad [\text{m}] \quad (4.25)$$

The *first Petukhov equation*, given in Equation 4.16 is here defined as f_s and the *Dittus-Boelter equation* (Dittus and Boelter, 1930) is given as

$$Nu_s = 0.023Re^{0.8}Pr^{0.4} \quad (4.26)$$

where the subscripts s and c denote "straight" and "coiled", respectively. At $1500 < Re < 8000$, the friction factor for a coiled duct is calculated from

$$\frac{f_c}{f_s} = 0.453 \times 10^{-3} Re^{0.93} \left(\frac{D/2}{a}\right)^{-0.22} \quad (4.27)$$

where D is the mean coil diameter and a is the duct width. For a tubular coil, the mean coil diameter would be measured from the tube centers. For a triangular duct, it is proposed that this distance is taken between duct centroids which, for a roughly triangular duct, would mean the centroid is at roughly 2/3 of the duct height from the duct root. At $Re > 8000$, the friction factor is given as

$$f_c \left(\frac{D}{D_h}\right)^{0.5} = 0.084 \left[Re\left(\frac{D}{D_h}\right)^{-2}\right]^{0.2} \quad (4.28)$$

Similarly, for $1500 < Re < 20000$

$$\left(\frac{Nu_c}{Nu_s}\right) = 1.0 + 3.6\left[\frac{D_h}{D}\right] \quad (4.29)$$

and for $20000 < Re < 150000$

$$\left(\frac{Nu_c}{Nu_s}\right) = 1.0 + 3.6\left[1 - \frac{D_h}{D}\right]\left(\frac{D_h}{D}\right)^{0.8} \quad (4.30)$$

4.3.4 Tip

Previous work by Lubkoll (2017) and McDougall (2019) sought to determine the jet impingement heat transfer characteristics of the spike tip where the work was confined to air mass flow rates of 0.026 kg/s and 0.0326 kg/s, respectively. The proposed heat transfer coefficients correlations are therefore not well suited for this analysis where a range of air mass flow rates will be used. A possible alternative would be to model the tip as purely an energy inlet where heat transfer is not determined by flow characteristics.

To overcome this, a similar process to Lubkoll (2017) and McDougall (2019) was followed where the tip region was modelled using ANSYS Fluent to obtain a correlation for the convection heat transfer coefficient at various air mass flow rates. The fluid domain was chosen as the spike tip, with a section of the spike extending 100 mm behind the tip region. Since the tip region can be described as uniform around the spike axis, the problem can also be simplified to an axi-symmetric model. From the work done in Lubkoll (2017), McDougall (2019) and Grobbelaar (2019), it was found that the realizable $\kappa - \epsilon$ turbulence model yields acceptable results was therefore also used for the spike tip model.

For increasing air mass flow rates, and subsequent increasing Reynolds numbers, it is expected that mesh refinement of the tip wall would be required to model the laminar sub-layer and buffer region. This would mean developing suitable meshes for each flow rate being tested. It is, however, desired that the same mesh be used throughout and, in this case, the use of scalable wall functions offers a suitable alternative. The use of scalable wall functions displaces the mesh to $y^+ \approx 11.225$ without consideration of mesh refinement at the wall, reducing the amount of refinement required to accurately model the laminar sub-layer and buffer region (Grotjans and Menter, 1998).

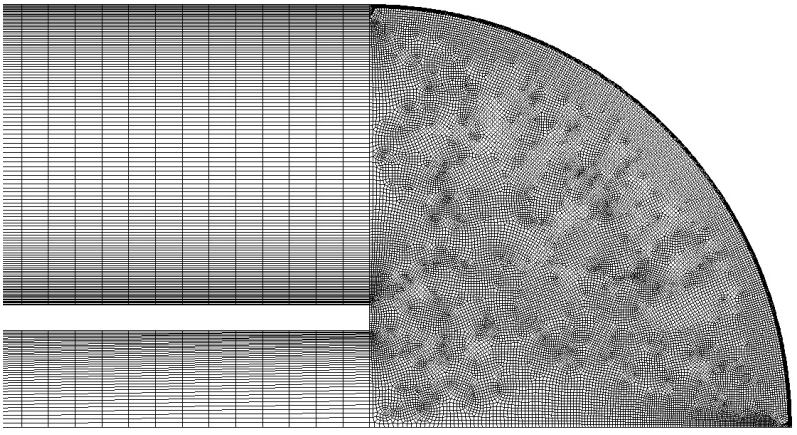

Figure 4.8: Coarse mesh at tip region

Starting from an initial coarse mesh, as shown in Figure 4.8, with total air mass flow rate at 0.11 kg/s, the mesh was successively refined at the tip

region until the average heat transfer coefficient at the tip wall was independent of mesh size and y^+ had reached approximately 11.225. The same mesh was used to obtain a correlation for the heat transfer coefficient with an air mass flow range from 0.01 kg/s to 0.11 kg/s. Mesh independence data can be found in Appendix B. The obtained average heat transfer coefficient values for increasing air mass flow rate are shown in Figure 4.9.

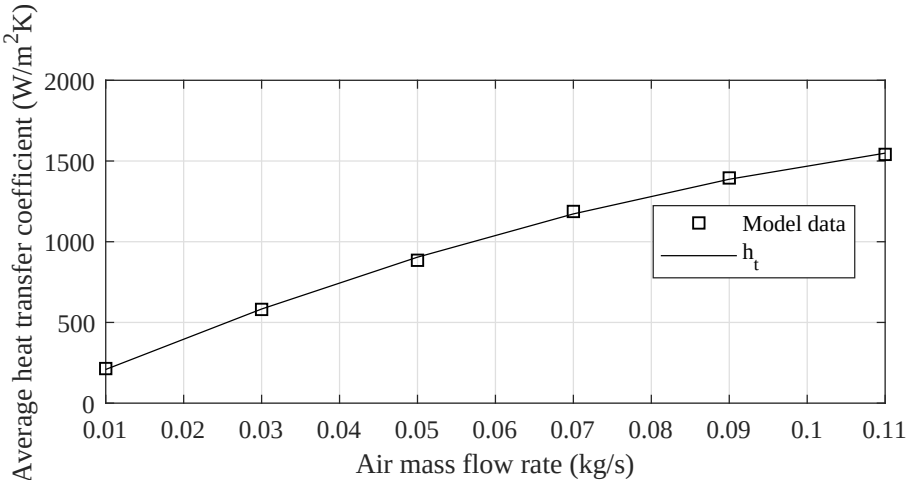

Figure 4.9: Average tip wall heat transfer coefficient for increasing air mass flow rates

The trend can be given by a second order polynomial in the form of

$$h_t(\dot{m}) = -6.65 \times 10^4 \dot{m}^2 + 2.138 \times 10^4 \dot{m} + 1.583 \quad [\mathrm{W/m^2K}] \tag{4.31}$$

4.4 External convection heat transfer

At the spike surface, or outer wall, and spike tip, combined natural and forced convection occurs due to wind and changes in air buoyancy. For a case where both natural and forced convection occurs, a combined Nusselt number approach is used where the combined Nusselt number is given as

$$Nu_{combined} = (Nu^n_{forced} \pm Nu^n_{natural})^{1/n} \tag{4.32}$$

where the $+$ or $-$ are used for assisting and opposing flows, respectively. The parameter, n, also varies from 3 to 4 for vertical and horizontal surfaces, respectively (Çengel and Ghajar, 2015). For this case, an assisting horizontal configuration is assumed. The Nusselt number for external natural convection over a horizontal cylinder and sphere is calculated using the equations provided in Çengel and Ghajar (2015), given as

$$Nu_{nat,cylinder} = \left(0.6 + \frac{0.387Ra_D^{1/6}}{[1+(0.559/Pr)^{9/16}]^{8/27}}\right)^2 \tag{4.33}$$

$$Nu_{nat,sphere} = 2 + \frac{0.589Ra_D^{1/4}}{[1+(0.469/Pr)^{9/16}]^{4/9}} \tag{4.34}$$

where the air properties are calculated at the film temperature, $T_f = 0.5(T_s+T_\infty)$. For the forced convection Nusselt number over a sphere, *Whitaker's equation* (Whitaker, 1972) is used, given as

$$Nu_{forced,sphere} = 2 + [0.4Re^{1/2} + 0.06Re^{2/3}]Pr^{0.4}\left(\frac{\mu_\infty}{\mu_s}\right)^{1/4} \tag{4.35}$$

where the subscripts s and ∞ denote the fluid viscosity at the wall surface and free stream temperatures, respectively. The forced convection Nusselt number over a cylinder is calculated using the equations provided by Žukauskas (1972), given in Table 4.1.

Table 4.1: Forced convection Nusselt number correlations for a cylinder in cross-flow (Žukauskas, 1972)

Reynolds number	Nusselt number
0.4 - 4	$Nu = 0.989Re^{0.330}Pr^{1/3}$
4 - 40	$Nu = 0.911Re^{0.385}Pr^{1/3}$
40 - 4000	$Nu = 0.683Re^{0.466}Pr^{1/3}$
4000 - 40,000	$Nu = 0.193Re^{0.618}Pr^{1/3}$
40,000 - 400,000	$Nu = 0.027Re^{0.805}Pr^{1/3}$

4.5 Thermal radiation heat transfer

At the spike surface, radiation interactions occur with surrounding spikes, the receiver base and the surrounding environment. From the perspective of this work, the surrounding spikes and the receiver base would exhibit higher temperatures than the center spike, which would give a radiative heat input to the center spike. Towards the front of the spike, as the distance between spikes increase, an increasing exposure to the surrounding environment is expected. The tip is, in all cases, completely exposed to the surrounding environment. The radiation interaction from a spike element to the surrounding receiver geometry and the surrounding environment is calculated from

$$\dot{Q}_{rad} = A_{oo}F_{1\to2}\epsilon_s\sigma(T_1^4 - T_2^4) \quad \text{[W]} \tag{4.36}$$

Where T_1 and T_2 denote the center spike element wall temperature and surrounding geometry/environment temperature, respectively. For the surrounding environment, the temperature is taken as $T_{sky} = 7\,^{\circ}\mathrm{C}$. Due to the long weather exposure of the experimental receiver, the thermal emissivity, ϵ_s, is taken as that of steel with a heavily oxidized surface, 0.81 (Çengel and Ghajar, 2015). To date, a multitude of work has been conducted in developing view factor correlations for a variety of common heat transfer configurations. For the view factor from the spike element to the receiver base, the spike is modelled as the surface of a cylinder normal to an annular disk at the end of the cylinder. The formulation given by Howell (1982) can be used, given as

$$F_{1\to2} = \frac{B}{8RH} + \frac{1}{2\pi}\left\{cos^{-1}\left(\frac{A}{B}\right) - \frac{1}{2H}\left[\frac{(A+2)^2}{R^2} - 4\right]^{1/2} \times cos^{-1}\left(\frac{AR}{B}\right) - \frac{A}{2RH}sin^{-1}R\right\} \tag{4.37}$$

where $R = r_1/r_2$, $H = h/r_2$, $A = H^2 + R^2 - 1$ and $B = H^2 - R^2 + 1$. r_1 and r_2 denote the cylinder and annular disk radii, respectively. The rule of superposition can be used to calculate the view factors for successive spike elements, which can be summarized as

$$F_{s,3\to b} = F_{s,(3+2+1)\to b} - F_{s,(2+1)\to b} \tag{4.38}$$

Several correlations exist for calculating view factors between inclined cylinders. None of the correlations, however, exactly match the current scenario and a combination of Hottel's crossed-strings method and the view factor for parallel cylinders is therefore used. The center spike and a neighboring spike is discretized as shown in Figure 4.10.

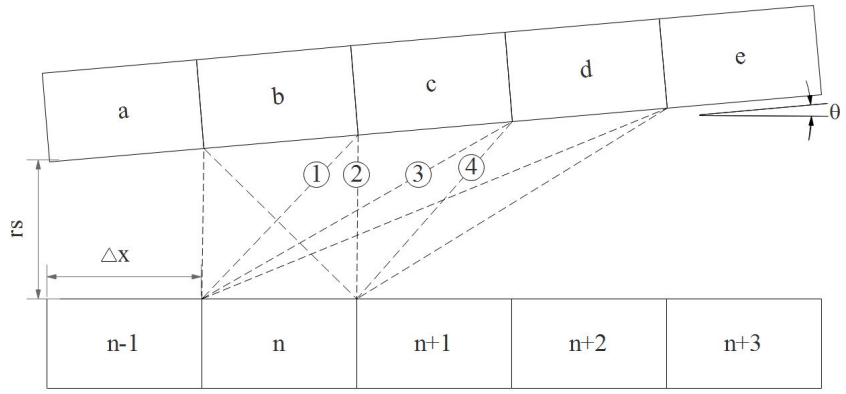

Figure 4.10: Discretization of center and neighboring spike

The uncrossed strings (① and ④) and crossed strings (② and ③) from a center spike element, n, to an element on the neighboring spike, in this case c, can be shown to take the form

$$\begin{aligned}
① &= \sqrt{(P\Delta x)^2 + (r_s + (n + (P-1))\Delta x sin\theta)^2} \\
② &= \sqrt{((P-1)\Delta x)^2 + (r_s + (n + (P-1))\Delta x sin\theta)^2} \\
③ &= \sqrt{((P+1)\Delta x)^2 + (r_s + (n + P)\Delta x sin\theta)^2} \\
④ &= \sqrt{(P\Delta x)^2 + (r_s + (n + P)\Delta x sin\theta)^2}
\end{aligned}$$

where P denotes the position of the neighboring spike element and θ is the inclination angle of the neighboring spike from the center spike. For directly opposing elements, $P = 0$, increasing to the right. For $n \to c, P = 1$. The formulation can be extended to obtain a 2-D view factor from a spike element, n, to every element on the neighboring spike, capturing the relative change in view factor to neighboring elements further away from the center spike element. The formulation of the crossed-strings method is given by

$$F_{i\to j} = \frac{\Sigma(Crossed\ strings) - \Sigma(Uncrossed\ strings)}{2(Strings\ on\ surface)} \tag{4.39}$$

To extend the 2-D view factor to a 3-D space, the assumption is made that between directly opposing elements the view factor can be approximated as that of parallel cylinders. The 2-D view factor between directly opposing elements is scaled to that of parallel cylinders, calculated using (Mills and Ganesan, 1999)

$$F_{1\to 2} = F_{2\to 1} = \frac{1}{\pi}\left[(X^2-1)^{1/2} + sin^{-1}\frac{1}{X} - X\right] \tag{4.40}$$

where $X = 1 + S/d$, as shown in Figure 4.11. The same scale factor is also applied to all other 2-D view factors. The above process is extended to include 6 inner row spikes angled at 3° from the center spike and 6 outer row spikes angled at 6° from the center spike, in accordance with the proposed design for the experimental receiver.

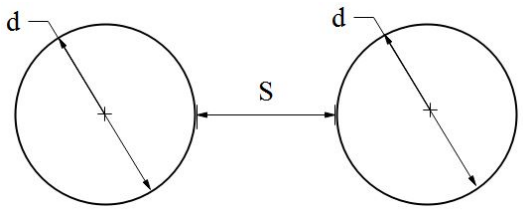

Figure 4.11: View factor between parallel cylinders

The view factor from a spike element to the surrounding environment is calculated using the premise that the total view from the element to all surrounding geometry and environment should be unity. The view factor to the surrounding environment, or sky, is calculated as

$$F_{1\to sky} = 1 - (6F_{1\to inner,spikes}) - (6F_{1\to outer,spikes}) - (F_{1\to base}) \tag{4.41}$$

4.6 Solar irradiation

The solar irradiation at the spike surface is given as

$$\dot{Q}_{rad} = p_{sol} A_{oo} \alpha_s I_{ap} \quad [\text{W}] \tag{4.42}$$

where I_{ap} and p_{sol} indicates the irradiation on aperture and irradiation concentration, as a percentage of the irradiation on aperture for a given position, respectively. The solar absorptance is taken, again as that of steel with a heavily oxidized surface, $\alpha_s = 0.89$ (Çengel and Ghajar, 2015).

4.6.1 Spike aperture

In order to calculate the spike thermal efficiency, the spike aperture is defined as the total area at the outer surface of the receiver that receives solar irradiation. The spikes on the experimental receiver will be angled at 3° from the center spike for each row of spikes. Each spike's aperture therefore spans 3° of arc from the theoretical center-point of the receiver. However, since the outer rows of spikes are not actively cooled and the heliostat field is to be aimed at the center spike, this definition is changed to include the total area between the inner spike row as depicted in Figure 4.12.

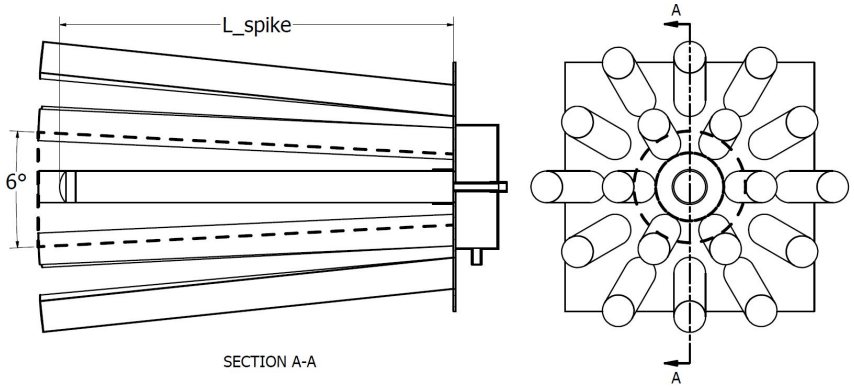

Figure 4.12: Depiction of spike aperture

The aperture area can be calculated from

$$A_{ap} = \pi(L_{spike} \tan 3^\circ + r_{spike} + r_s)^2 \qquad [\mathrm{m}^2] \quad (4.43)$$

where r_{spike} and r_s denote the spike radius and root spacing, respectively.

4.6.2 Irradiation concentration

As discussed previously, a ray tracing analysis using Tonatiuh ray tracing software was conducted by Lubkoll (2017) to determine the effects of heliostat field design on receiver performance. From the variety of existing ray tracing software packages available, only Soltrace (NREL) and Tonatiuh (CENER) are "free-to-use" (Bode and Gauché, 2012). Both packages have been shown to be able to model complex systems efficiently and with good accuracy. The user interfaces for both packages are, however, cumbersome and therefore their use may be hard to justify for simple analyses where the cost of setup time may outweigh the advantage of efficiency and accuracy.

A novel approach to solving the radiative transfer equation using the finite volume method, in particular the discrete ordinate (DO) method, in ANSYS Fluent has been investigated by Moghimi *et al.* (2015) to combine optical and thermal modelling of a linear fresnel collector receiver. The most notable limitations of the DO method, as described by Chai and Patankar (2006), are false scattering and the ray effect. False scattering occurs due to numerical diffusion and leads to smearing of the projected radiation. The ray effect leads to incorrect directions of the projected radiation. These limitations can be overcome by refining the computational mesh, increasing the angular discretizations of the DO model or by increasing the spatial discretization order.

Moghimi *et al.* (2015) found that for increasing mesh size, angular discretization and spatial discretization order, results comparable to the Implicit Monte Carlo method could be obtained. It was further found by Craig *et al.* (2015) that when the computational domain can be said to be symmetric or axi-symmetric, a 2-D formulation could be used whereby the DO model solves for $4(N_\Phi \times N_\theta)$ directions for four octants instead of the more computationally expensive 3-D formulation, $8(N_\Phi \times N_\theta)$ directions for eight octants.

In order to gain a better initial understanding of the irradiation concentration on the spike surface, a DO radiation model using the domain shown in Figure 4.12 was developed. A process similar to Craig *et al.* (2015) was followed where the area between the inner spike row is modelled and an axi-symmetric formulation is used to reduce the computational resource requirements, as shown in Figure 4.13. At the aperture, an arc is used with a center point coinciding on the spike axis behind the tip. The aperture is modelled as a transparent wall with direct specular irradiation of $1000\,\mathrm{W/m^2}$ into the domain. The direction is specified as normal to the boundary using a user defined function.

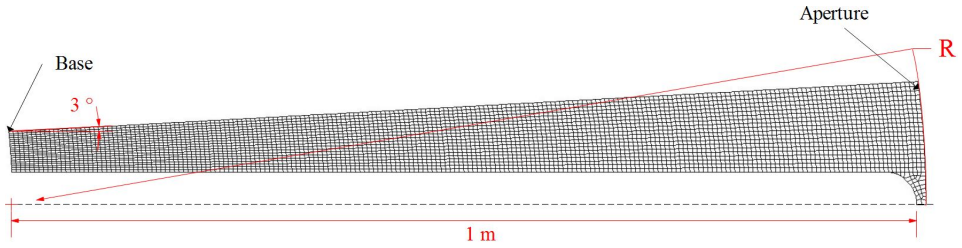

Figure 4.13: DO radiation model intermediate mesh example

The spike wall, tip and top of the domain are modelled as black opaque walls with an emissivity of 1. To induce irradiation reflection from the receiver base to the spike, the base is modelled as a grey surface with an emissivity to solar radiation of 0.92 (Çengel and Ghajar, 2015). Irradiation from the base is defined as purely diffuse. To verify mesh independence, an initial arc center point was set at 1 m behind the tip. In this configuration, the highest amount of false diffusion would be experienced as the irradiation direction would be dis-aligned with the computational mesh.

Mesh density and the amount of angular discretizations was increased until a constant value for average surface incident radiation was obtained on the spike wall. This process was repeated for both 1^{st} and 2^{nd}- order upwind spatial discretization schemes, as discussed in Appendix B.3. The solution was found to be stable for a mesh with 4094 cells, using $N_\theta \times N_\Phi = 70 \times 70$ angular divisions with a 2^{nd}- order upwind scheme.

For a receiver with the reference geometry set out in Lubkoll (2017), the irradiation focal point would be at the center of a sphere with a 2 m radius. For a 1 m length spike, this would coincide with a focal point at 3 m behind the tip. To simulate a constant irradiation at the spike aperture converging to the center point of the receiver, the arc center point was changed to 3 m behind the tip. For the 3 m case, the average surface incident radiation on the spike wall amounted to 70.72 W/m^2. An average base surface incident irradiation of 1857.78 W/m^2 was also recorded. The obtained irradiation profile is shown in Figure 4.14.

From the DO model, it is seen that behind the spike tip the irradiation concentration on the spike wall is roughly 2.3% of the irradiation on aperture. The irradiation concentration increases exponentially towards the spike root, to approximately 22%, where a sharp increase in concentration is experienced due to irradiation reflection from the receiver base. To incorporate the irradiation profile into the 1-D model, a 2-term exponential curve is fitted to the given profile in Figure 4.14, given by

$$p_{sol1} = 0.16e^{-37.48l} + 0.0785e^{-0.8895l} - 0.00945 \tag{4.44}$$

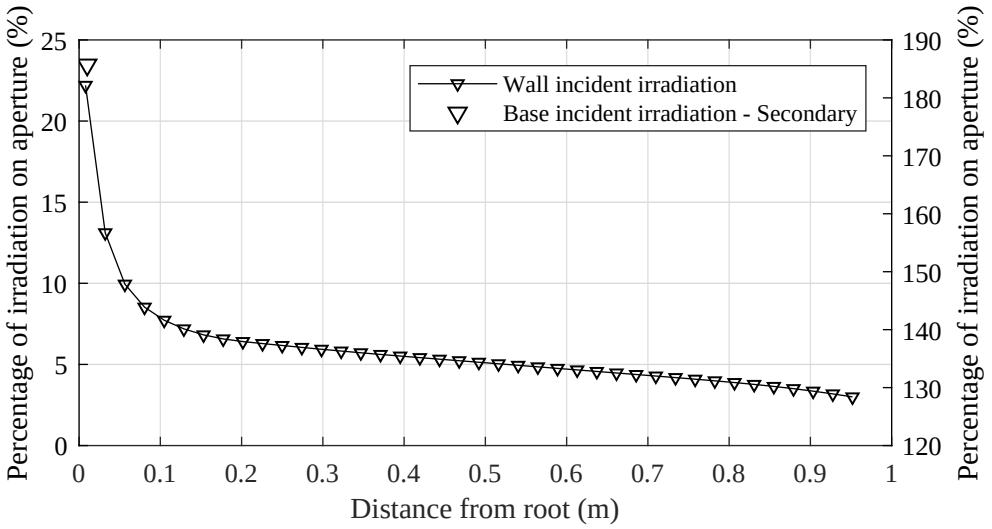

Figure 4.14: Surface incident radiation profile for an aperture focus point at 3 m behind the tip

The irradiation concentration profile obtained from the DO model is considered an ideal approximation that would be exhibited with a perfectly focused heliostat field. It is not expected that this would be the case for the experimental work conducted. Both the DO model irradiation concentration profile, as well as a more realistic formulation will be considered after obtaining experimental data.

4.7 Conclusion

The developed model would be used to gain a better overall understanding of the thermal performance of a SCRAP spike under a variety of external conditions as well as to confirm thermal tendencies due to potential instrumentation limitations. The 1-D model, along with the DO irradiation model would also aid in characterizing the irradiation concentration on the spike surface under realistic operating conditions. Finally, the 1-D model would serve as a platform to predict the performance of a fully finned spike and to compare its thermal efficiency to that of an open annulus spike. The effect of the internal fins on the total heat transfer in the spike will also be investigated.

Chapter 5

Experimental design and setup

Based on the findings of the existing literature and previous work conducted on the SCRAP receiver, an experimental receiver was designed and constructed. The receiver was installed on the Solar Roof Laboratory's lattice tower and tested in on-sun conditions. This chapter covers aspects of the experimental investigation such as the experimental facility, experimental setup and instrumentation locations. Experimental limitations and constraints are also discussed.

5.1 Helio40 facility

The Helio40 solar research facility shown in Figure 5.1, funded by Sasol, is situated on the solar roof of the Mechanical and Mechatronic Engineering building at Stellenbosch University. The length of the solar roof sits at a heading of roughly 293°. It consists of a receiver tower and a heliostat field. The heliostat field is located at the south-eastern end of the roof and houses 18 1.83 m × 1.22 m heliostats with a combined aperture of 40 m^2.

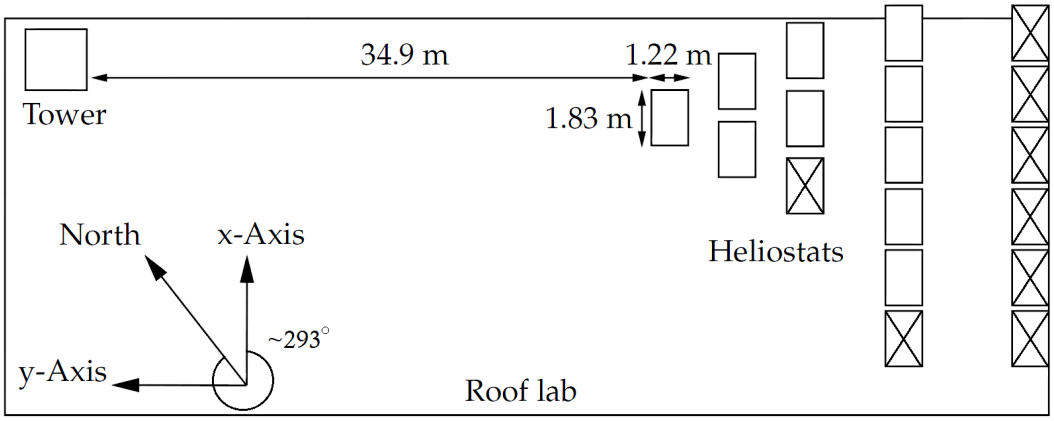

Figure 5.1: Schematic of Helio40 facility (Grobler, 2015)

The 18 m receiver lattice tower sits at the northern corner of the roof and holds a Lambertian target at the bottom, a heliostat calibration target and mounting space for a receiver at the top, as shown in Figure 5.2a. At the time of testing, 12 heliostats had been installed and fitted with control modules. Of these 12, Heliostats 4 and 7 shown in Figure 5.2b had experienced intermittent

failures. As a result, only 10 heliostats were functioning reliably and therefore only 22 m^2 of the 40 m^2 combined aperture was utilized.

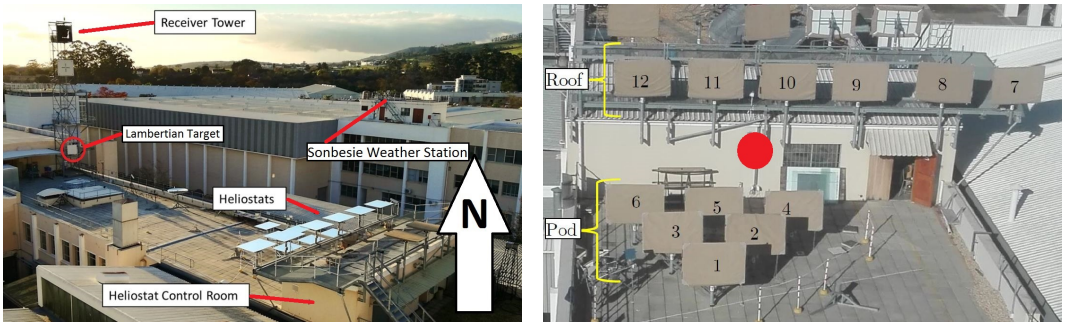

(a) Helio40 layout (Joubert, 2019) (b) Helio40 heliostat field (Basson, 2019)

Figure 5.2: Helio40

5.1.1 Heliostat field characterization

In order to calculate receiver thermal efficiency it is important to have a reliable measurement of incoming solar radiation from the Helio40 heliostat field. To this end a study was conducted to characterize the performance of the heliostat field.

Two Kipp & Zonen CMP11 pyranometers were used to measure DNI and concentrated irradiation. The concentrated irradiation pyranometer was attached to the Lambertian target located at the bottom of the tower, as shown in Figure 5.2a. The DNI pyranometer was positioned 10 m from the base of the tower. Heliostat 1, shown in Figure 5.2b was aimed at the target with the pyranometer at the center of the focal image. To avoid damaging the pyranometer by overheating, this process was repeated over the course of 3 hours with an exposure time of 2 minutes per run. Figure 5.3 shows the measured concentrated irradiation on the target and the corresponding solar DNI over the test period. During the 3 hour period, a maximum and minimum DNI of 850 W/m^2 and 300 W/m^2 was observed, respectively.

From Figure 5.3, for each DNI band a shift in irradiation concentration from an initial maximum value to a final minimum value is observed. Since the heliostat is initially aimed with pyranometer at the center of the focal image and left stationary, the focal image will drift as the sun moves and the relative angle between the sun and target, as viewed from the heliostat, changes. As such, a maximum, minimum and mean value of concentrated irradiation is taken, capturing the Gaussian irradiation distribution of the heliostat focal image. The mean value would give a more realistic approximation of total irradiation on the receiver aperture as the heliostat aiming and tracking errors would mean that peak irradiation is rarely experienced at the initial aim point.

Cosine losses over the course of the test were the primary contributor to variation in the irradiation concentration factor shown in Figure 5.3. Cosine losses are defined as the losses that occur due to the changing angle between the sun and the target, when viewed from the heliostat. Fouling losses would also contribute to overall heliostat efficiency, however, in this case is assumed to be constant as heliostats are cleaned prior to each test during the project. Finally, blocking and shading could also contribute to some losses when the entire heliostat field is used. Blocking losses are, however, difficult to quantify in this setting and were not generally observed during the experimental test as the tests occurred around late morning to early afternoon, where solar altitude is still high. The developed correlation would then serve as a lumped performance prediction which accounts for only cosine and fouling losses.

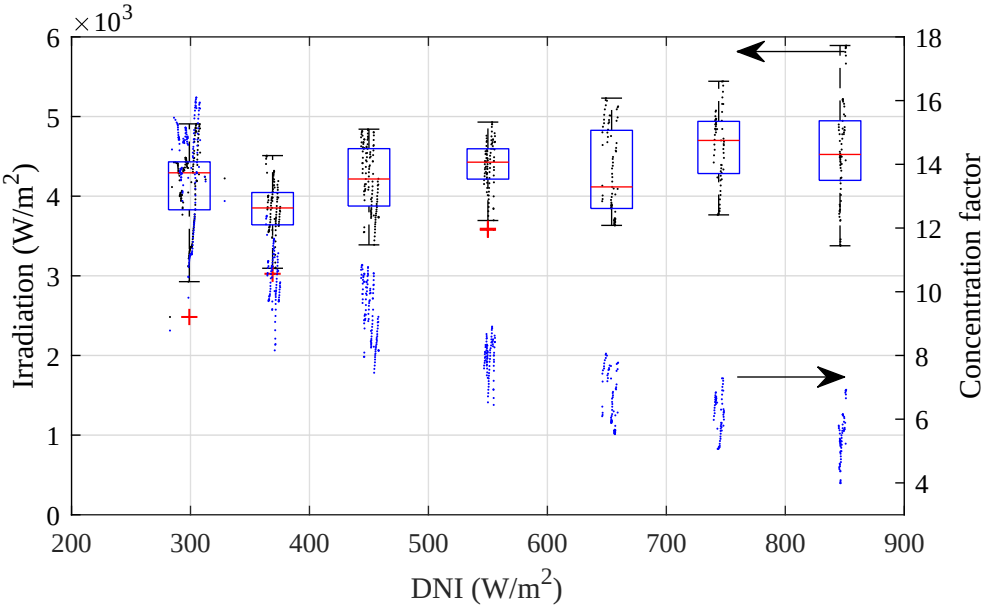

Figure 5.3: Irradiation on target with corresponding solar DNI

In order to calculate the effect of changing solar position on heliostat concentration factor, the relative angle between the receiver and the sun, as viewed from the heliostat needs to be calculated. The process, as outlined by Duffie and Beckman (2006) and Stine and Geyer (2001) is followed. The hour angle is the displacement of the sun from the local time meridian resulting from the rotation of the earth on its axis and is calculated by

$$\omega = 15(t_s - 12) \qquad [^\circ] \quad (5.1)$$

where t_s is the solar time and given in decimal hours from midnight. To compensate for variation in solar time during the year a solar time correction, given in minutes, is added to the solar time and given as

$$Solar\ time = Standard\ time + 4(L_{st} - L_{loc}) + E \qquad [\text{h}] \quad (5.2)$$

where L_{st} and L_{loc} represent the local time meridian longitude and local longitude respectively, measured from east to west ($0 < L < 360$). For South Africa and the Helio40 facility, these longitudes are 337.5 °W and 341.13 °W respectively. E is given by

$$\begin{aligned} E = 229.2(&0.000075 + 0.001868\cos B - 0.032077\sin B \\ &- 0.014615cos2B - 0.04089\sin 2B) \end{aligned} \quad (5.3)$$

and B is given by

$$B = (n-1)\frac{360}{365} \quad (5.4)$$

where n is the number of days since the first of January. The sun's declination angle can be calculated from

$$sin\delta = 0.39795cos[0.98563(n-173)] \qquad [^\circ] \quad (5.5)$$

Finally, solar altitude and azimuth, α and A, can be calculated using

$$\alpha = \arcsin[\sin\delta\sin\phi + \cos\delta\cos\omega\cos\phi] \qquad [^\circ] \quad (5.6)$$

$$A" = \arccos\left(\frac{\sin\delta\sin\phi - \cos\delta\cos\omega\cos\phi}{\cos\alpha}\right) \qquad [^\circ] \quad (5.7)$$

where if $\omega \leq 0, A = A"$ and $\omega > 0, A = 360^\circ - A"$. ϕ is the local latitude. For the Helio40 facility, $\phi = 33.9284\,^\circ$S. The obtained altitude and azimuth angles can be converted to direction vector form using

$$P_s = \begin{bmatrix} \cos\alpha\sin A \\ \cos\alpha\cos A \\ \sin\alpha \end{bmatrix} \quad (5.8)$$

where P_s denotes solar position. Similarly, for a receiver altitude and azimuth of 27.92° and 293.15°, P_r can also be obtained. The final relative angle between the sun and receiver, as viewed from the heliostat is given as

$$\cos\Phi = \frac{P_s \cdot P_r}{|P_s||P_r|} \quad (5.9)$$

The measured concentration factor data was used to correlate concentration factor with relative angle. Figure 5.4 shows the measured data with the proposed correlations given by

$$CF_{max} = 112.3\Phi^{-1.124} + 5.488 \quad (5.10)$$

$$CF_{avg} = 100.8\Phi^{-1.097} + 4.164 \tag{5.11}$$

$$CF_{min} = -1.788\Phi^{0.4226} + 13.16 \tag{5.12}$$

A 20% deviation is indicated around the average concentration factor. Figure 5.4 shows that while the maximum concentration factor stays between these bounds, the minimum concentration factor only stays between the bounds for relative angles between 15° to 40°. It should be noted that the focal image of each heliostat is different, where some heliostats show larger or smaller slope errors than that of Heliostat 1, used for this analysis. This necessarily means that some uncertainty may be present when applying the developed correlations, however, the correlations should still provide a reliable estimate between the maximum and mean values.

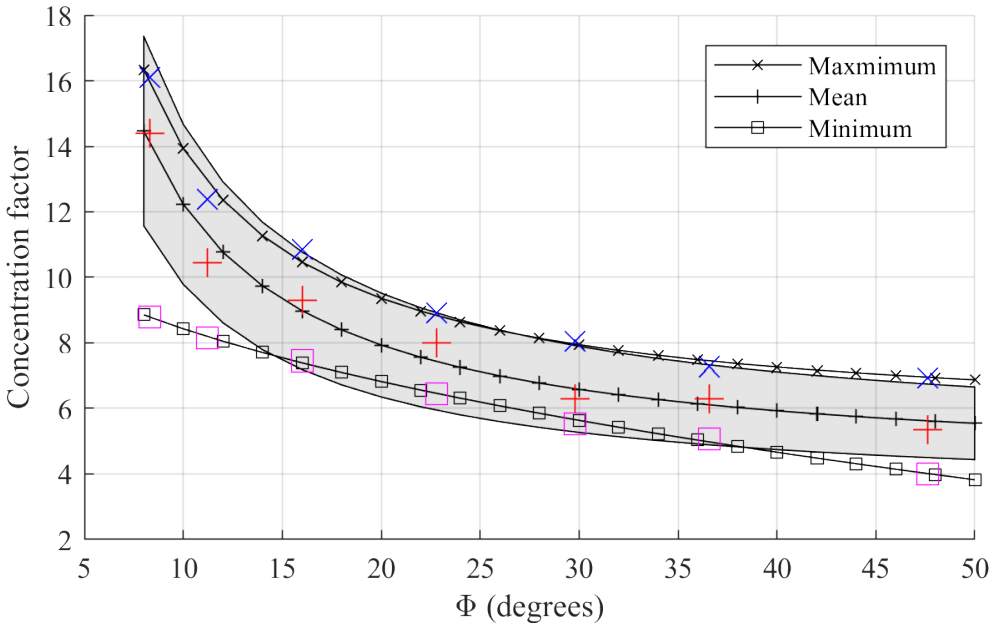

Figure 5.4: Concentration factor prediction

5.2 Receiver

The main objectives in generating a design concept for the receiver were that the spike operate in the same environment as the full scale receiver. The spike would therefore need to be situated between a cluster of spikes so the view factor from the spike to the surrounding spikes and environment as well as convective shielding could be emulated.

A schematic of the built receiver is shown in Figure 5.5. The sizing parameters were centered around the reference design size set out in Lubkoll (2017), with a sphere radius of 2 m and a spike length of 1 m. Manufacturing practicality was of high importance during the design process and therefore the chosen

spike center to center distance at the root was taken as 120 mm and 44 mm of open space between neighboring spikes. This dimension is governed by accessibility when welding the inner and outer spike rows to the receiver base, insomuch as the welding torch would need to fit between neighboring spikes at the root. At the root, the spikes are positioned on a tessellated triangular grid. Based on a 2 m sphere radius and the chosen center to center distance of neighboring spikes, the first and second row of spikes incline at 3° and 6° respectively from the center spike.

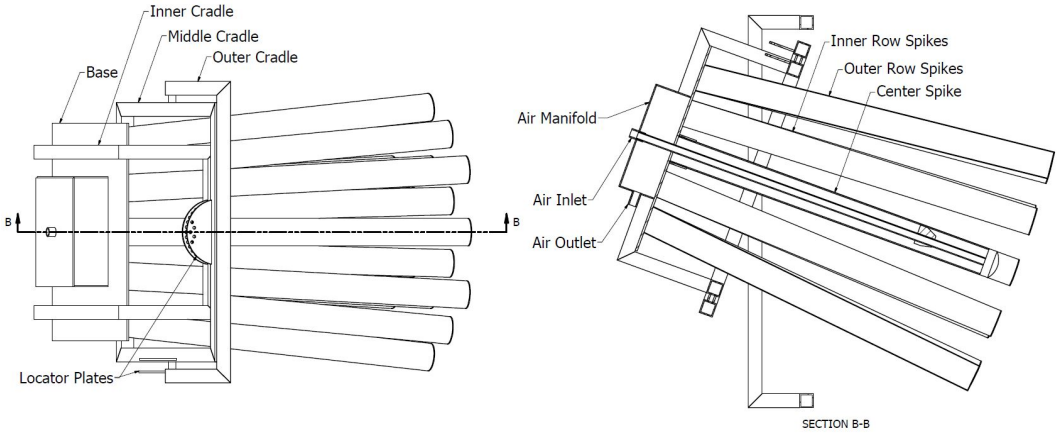

Figure 5.5: Schematic of built SCRAP receiver

Since two spike configurations would need to be tested, a threaded collar was fitted to the receiver base so that the center spike could be screwed in, instead of a more complicated bolting arrangement. This would also allow for a simpler manifold assembly as access to the rear of the center spike would not be required. It follows that, for a threaded spike attachment and a manifold welded to the receiver base, any sealing requirements such as specialized gaskets are also eliminated, reducing the overall financial cost.

While designing the experimental receiver, the largest considerations were material availability, cost and manufacturing time. The design was therefore centered around commercially available materials, particularly mild steel for its low cost. The finned spike sections provided for this project were 3-D printed from CL 50WS hot-work steel, with an outer diameter of 75.8 mm. Consequently, 65 NB (or 2 1/2") mild steel pipe was selected for the center and surrounding spikes. To match the finned sections, the inner tube was chosen as a 1/2" pipe with a wall thickness of 2.3 mm. For the open annulus spike, fins were attached to the inner tube to ensure its concentricity inside the spike.

The outer row spikes serve only a cosmetic role, in terms of shielding, for the experimental receiver and was therefore selected with a wall thickness of 1.6 mm, the lowest available thickness, in order to reduce the overall receiver

weight. The center spike would need to be threaded with either 2 1/2" BSPP or BSPT thread, depending on manufacturing capability. With a thread minor diameter of 72.226 mm (Oberg *et al.*, 2008), the center spike was selected with a wall thickness of 3.6 mm to ensure adequate material thickness (min≈1.8 mm), when accounting for material tolerance, to maintain the spike's structural integrity. The added material thickness would also allow for a flange to be fitted to mount the finned sections.

Welding the finned sections together, as well as to the rear open annulus section was considered. Tool steel is, however, typically highly susceptible to cracking when welded due to its high hardenability. From a risk perspective, welding was deemed a non-feasible option as the facilities to ensure proper welding and post-weld heat treatment were not available. The finned sections would also be too expensive to replace should irreparable damage occur.

As the inner and outer spike rows are uncooled, it is expected that these spikes would reach higher temperatures than both the base and center spike. Combined with the comparably low thermal mass, these spikes may also be susceptible to higher rates of expansion and contraction with changing irradiation concentration. The outer rows are therefore only tack-welded to the receiver base to allow for some expansion during the tests. Tack welding would also limit the amount if heat input to the base while assembling the receiver, reducing the amount of warping experienced by the base. The outer spikes were capped off with flat laser-cut circles to ensure that irradiation does not penetrate to the base.

Since the base would have all the functioning components welded to it, it would need to support its own weight as well as the spikes and manifold. The base would also be welded to the mounting cradle. The base would need to withstand the heat from welding without significant warping as well as withstand high solar irradiation during the tests. The base was therefore chosen as 5 mm thick mild steel plate with a dimension of 600 mm × 600 mm to fit the inner and outer row spikes at the determined spacing. To save on cost and material purchasing, the base was laser-cut by an external contractor, along with the manifold and inner/outer row spike caps.

The manifold at the rear of the receiver was constructed from 3 mm thick mild steel sections. From previous experience in the faculty workshop, when welding dissimilar thickness materials or lower thickness materials around 2 mm or less, weld over-penetration frequently occurs leading to leaky welds or significant material warping. A leak free weld would be required for the manifold where it is attached to the base as well as at the inlet/inner tube coupling. The manifold was therefore oversized to mitigate the risk of weld over-penetration and subsequent corrective re-welding.

The receiver was mounted inside a three-piece gyroscopic cradle. The outer section, mounting the assembly to the tower is offset at 180 mm and allows for elevation adjustment of the receiver face. The middle section allows for azimuthal adjustment. The inner section is offset a further 300 mm and holds

the receiver assembly. Semicircular plates attached at the swivel points with 5° increment holes serve to fix the receiver in its aimed position. The cradle was constructed from 38 mm × 3 mm mild steel square tubing to match the existing tower frame.

The combined offset ensures that the receiver's center of mass stays inside the tower structure while balancing the receiver on the mounting points. As the receiver is balanced inside the cradle, little effort is required to make final aiming adjustments. In order to get uniform irradiation exposure along the circumference of the spike, the center spike was aimed at the red marker indicated in Figure 5.2b. This would place the receiver aim point at the center of the remaining operational heliostats. Figure 5.6 shows the installed receiver.

(a) Receiver in operation with focal image drift

(b) Installed receiver with center spike removed after long weather exposure

Figure 5.6: Experimental receiver

5.3 Instrumentation and locations

The exposed nature of the SCRAP receiver poses a variety of challenges with respect to data measurement. First, the experimental receiver would be mounted on the tower for months at a time, exposed to a variety of weather conditions. The functional end of the receiver is also inaccessible once the receiver is installed. Any instrumentation mounted on the spike would need to be able to withstand long exposure to wind, rain and sunlight as it cannot be installed and removed before and after tests. The second and more pertinent challenge is that equipment would need to withstand exposure to concentrated solar irradiation and consequently high heat flux. The main properties required

to characterize the performance of the SCRAP spike are temperature, mass flow, pressure and irradiation.

5.3.1 Temperature

To measure temperature on the spike wall, a selection of J-type thermocouples was used. In order to withstand the high heat flux on the exposed side of the receiver, thermocouples were chosen with fiberglass insulated, stainless steel braided cables. On the open annulus spike surface, 6 mm diameter thermocouples were used. These thermocouples were mounted inside a cup with a bayonet fitting so that they could be easily removed when changing spike configurations. The cup would also serve to shield the thermocouple tip from irradiation which could affect temperature measurements. Figure 5.7 shows the open annulus spike construction with thermocouple distribution on the spike surface.

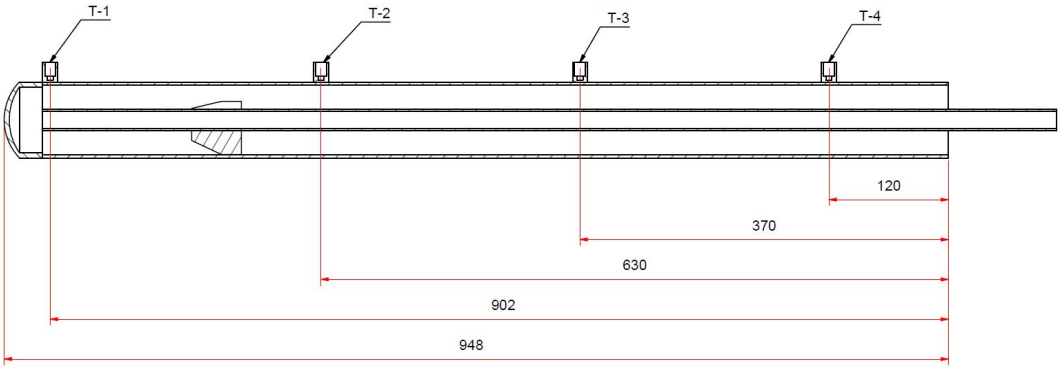

Figure 5.7: Open annulus spike construction with thermocouple locations

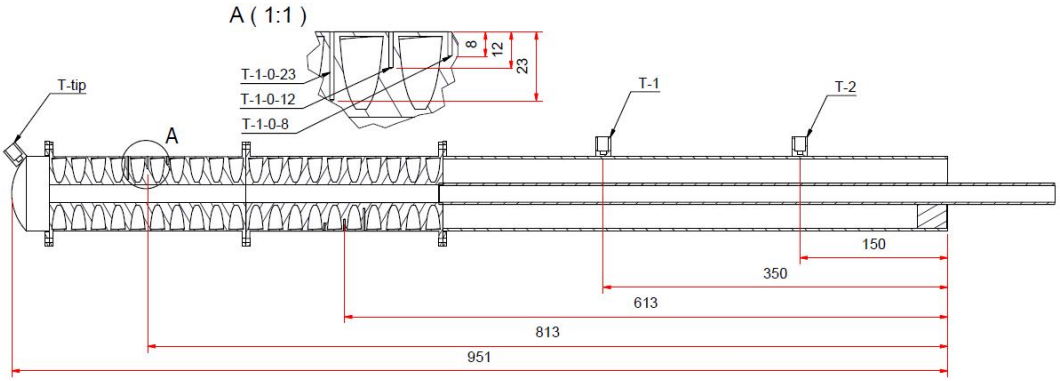

Figure 5.8: Finned annulus spike construction with thermocouple locations

The finned annulus spike is made up of two 3-D printed internally finned sections towards the front, with an open annulus section toward the rear.

Tip temperature and surface temperatures on the open annulus section are measured with the same 6 mm diameter thermocouples. The finned sections each have two rows of holes, 90° apart, with one row containing 8 mm, 12 mm and 23 mm deep holes. These holes are spaced to measure temperature along the height of the internal fin.

The holes are sized to fit 1.5 mm diameter thermocouples. Figure 5.8 shows the finned annulus spike construction with thermocouple distribution on the spike surface. As discussed, the finned sections are printed from tool steel, which poses a set of challenges when welded. Mounting a thermocouple cup on the outer surface would require post-welding heat treatment and the facilities for this heat treatment were not readily available. It was therefore decided not to measure surface temperature on the finned sections.

Air inlet temperature is measured as shown in Figure 5.5. The air inlet tube extends 200 mm from the rear of the receiver to ensure that the measurement is not affected by conduction from the air manifold. Spike outlet temperature is measured at 10 mm adjacent from the air inlet, where the thermocouple extends from the air manifold into the open annulus of the spike. Manifold temperature is measured at 50 mm above the air inlet where the thermocouple extends 50 mm into the air manifold. Receiver outlet temperature is measured at the manifold exhaust outlet, which extends 1.5 m from the manifold outlet.

5.3.2 Mass flow

Due to financial limitations, purchasing an application specific air flow meter for the experimental setup was deemed unfeasible. In order to reduce manufacturing costs and installation time, it was decided to implement a rudimentary obstruction type flowmeter in the form of a rigid u-bend pipe. The pipe would be situated at the bottom of the tower between the connecting flexible hose lines. Various calibration strategies were utilized in order to obtain an accurate estimate of pressure drop across the pipe for a corresponding volumetric flow rate. The process followed is outlined in Appendix E.5.

5.3.3 Pressure

In order to measure the static pressure drop across the spike, it would be required to install a pressure sensor, or pressure tap, at the root of the spike on the irradiated side of the receiver, as well as at the air inlet. While installing a pressure tap at the air inlet is a relatively straightforward process, installing a pressure tap at the spike root is somewhat more complicated. Here the transducer, or pressure lines - depending on the case, would need to be able to withstand the same high heat flux as experienced by the thermocouples.

At the time of designing the experimental receiver, suitable pressure sensors or suitable high temperature pressure lines could not be obtained before starting the manufacturing work. The static pressure drop across the spike

is therefore not monitored. Here, a suitable solution would have been to use metallic tubing such as automotive brake lines, which are widely available and reasonably priced.

5.3.4 Solar radiation

DNI was measured using the Kipp & Zonen CMP11 pyranometer as mentioned in section 5.1.1. The pyranometer was positioned 10 m from the base of the receiver tower, with care being taken to ensure that no shadows from the surrounding experimental setups, equipment or buildings obstructed irradiation. Using the concentration factor correlations obtained from the heliostat field characterization, the incident solar radiation can be calculated as

$$I = DNI \cdot CF \cdot n \qquad [\mathrm{W/m^2}] \quad (5.13)$$

where n is the number of heliostats operating during the test. When calibrating the heliostats, an aimpoint was set to the center of the inner row of spikes. This would ensure that the majority of the solar irradiation fell on the center spike.

5.3.5 Environmental variables

A thermocouple located under the data-logger, behind the receiver, was used to measure ambient air temperature. The thermocouple was placed under the data-logger to shield the thermocouple tip from irradiation which could affect temperature measurements. Wind speed and direction measurements were obtained from the Sonbesie weather station, shown in Figure 5.1, which is situated roughly 50 m away from the receiver on the neighboring building.

5.4 Experimental limitations and constraints

The primary limitations and constraints experienced during the experimental work pertained to the heliostat field as well as the location of the receiver. The receiver, along with data logger was installed on top of the 18 m high tower. This limits accessibility to the receiver should sensor malfunction occur as supervision is required to climb the tower to investigate. Due to the exposed nature of the tower, the experimental setup can also not be accessed during the tests. A particular problem proved to be the fiberglass insulation of the shielded thermocouples. During periods where the receiver was not operational, the insulation would absorb moisture, either from dew or rain, which would wick to the probe ends and cause erroneous temperature readings. The receiver would then need to be run for several hours for the moisture to dissipate where complete datasets could not be obtained.

The heliostat field control system is Wi-Fi based, where the graphical user interface is hosted off-site. Since the heliostat field utilizes the central Wi-Fi network, performance of the field is directly related to the volume of traffic across the network, where high traffic volumes would slow communications to the off-site location causing a slow response from the heliostats. Practically, this translates to increased tracking errors during operation or difficulty calibrating the field before the start of a test. Due to the small aperture of the experimental receiver, tracking errors would cause difficulty in obtaining steady state operation. In extreme cases, individual heliostats would time-out and stow in accordance with their emergency shut-down protocol or be "lost" during a tracking update, in which case the rest of the field would need to be defocused while recovering the lost heliostat.

5.5 Error analysis

To quantify the overall system measurement error, the instrumentation was calibrated and the calibration error was recorded. Where the instrumentation could not be directly calibrated, calibration errors were obtained from the manufacturer data sheets and the instrumentation was compared to other units available to check for probable readings. If neither of the above was possible, the maximum error was included in the overall error estimation. Further discussion on the calibration processes is included in Appendix E. The total system measurement error was calculated to be 7.68%.

5.6 Conclusion

To satisfy the objectives set for this study, an experimental receiver was constructed which approximates a full-scale SCRAP receiver. An experimental setup was also designed which would be used to characterize the receiver's performance in on-sun conditions. This includes the total air flow through the receiver, the air inlet, outlet and surface temperatures as well as the irradiation on aperture. To determine the receiver's susceptibility to convective losses, wind data is also measured.

Chapter 6

Experimental results, analysis and discussion

The receiver was installed on the Helio40 tower by the end of May, 2019, at the start of the winter season in Stellenbosch. Inclement weather during the project dictated that only small windows of opportunity were available in which complete data sets could be obtained with favorable weather. This chapter presents the results of the final tests for each spike configuration. A discussion on the experimental data is given to conclude this chapter where the practical impact of the results are discussed.

In Figure 6.1, the receiver orientation relative to north and relative to the prevailing wind direction experienced during the tests is shown. For both tests, wind direction was only experienced inside the $200° - 300°$ sector.

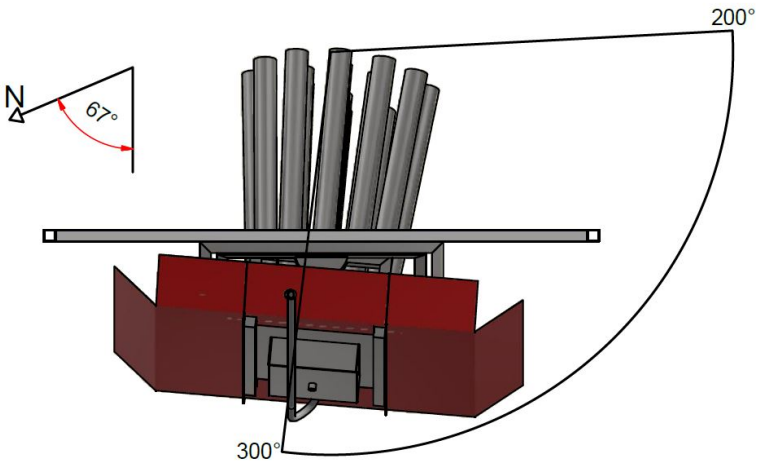

Figure 6.1: Prevailing wind direction relative to installed receiver

6.1 Open annulus spike test data

Temperature and air mass flow rate data for the final open annulus spike test are shown in Figure 6.2. During the test, air mass flow rates ranged from 0.022 kg/s to 0.133 kg/s. Air inlet temperatures remained reasonably constant, fluctuating between 34.9 °C to 33.9 °C. A maximum and minimum air outlet temperature of 67.01 °C and 45.2 °C was obtained at air mass flow rates of 0.042 kg/s and 0.107 kg/s, respectively.

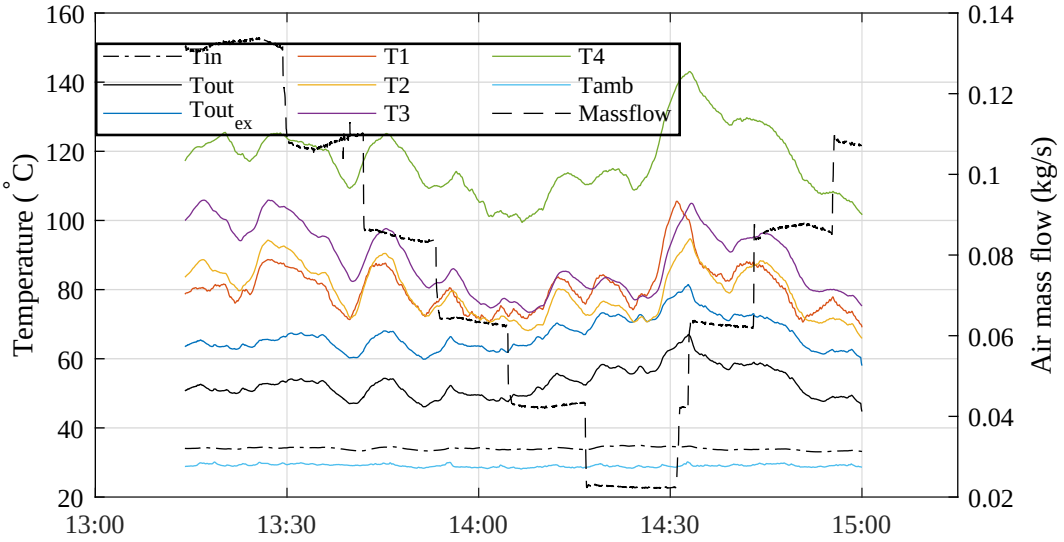

Figure 6.2: Open annulus spike surface temperatures and air mass flow rates

During the test, the highest surface temperature obtained was 142.5 °C at $T4$, while the lowest surface temperature obtained was 68.17 °C, at $T2$. Considering the lowest surface temperature did not occur at $T1$, behind the tip, this indicates that irradiation concentration towards the front of the spike is relatively low. Here, $T1$ would be influenced by the tip temperature through axial conduction, when the mass flow rate is too low to provide sufficient tip cooling. Thermal images taken from the receiver aim point showed that the receiver base surface temperature between the inner row spikes varied between approximately 140 °C to 180 °C for the air mass flow rate range. At high air mass flow rates, the base temperature would reach approximately 20 °C above $T4$, whereas this would increase to 40 °C for low air mass flow rates.

Irradiation and wind data are given in Figure 6.3. During the test, DNI decreased from 917 W/m^2 at the start of the test to 701 W/m^2 at the end of the test. Due to the changing solar angle and subsequent change in concentration factor, this resulted in an initial estimated irradiation on aperture of 51.47 kW/m^2, peaking at 53.44 kW/m^2 and decreasing to 51.75 kW/m^2 at the end of the test. Wind speed ranged from 0.86 m/s to 3.78 m/s, which can generally be regarded as a light breeze or a Beaufort number of 2. Wind direction fluctuated between $200° - 260°$. Referring to Figure 6.1, wind direction for the open annulus test can be considered as a dominantly cross wind. Due to the large variance in both wind speed and direction, a 5-minute running average is taken. For the following analysis, only the crosswind component of the wind speed is used, where the normal direction of the spike is taken as 210°.

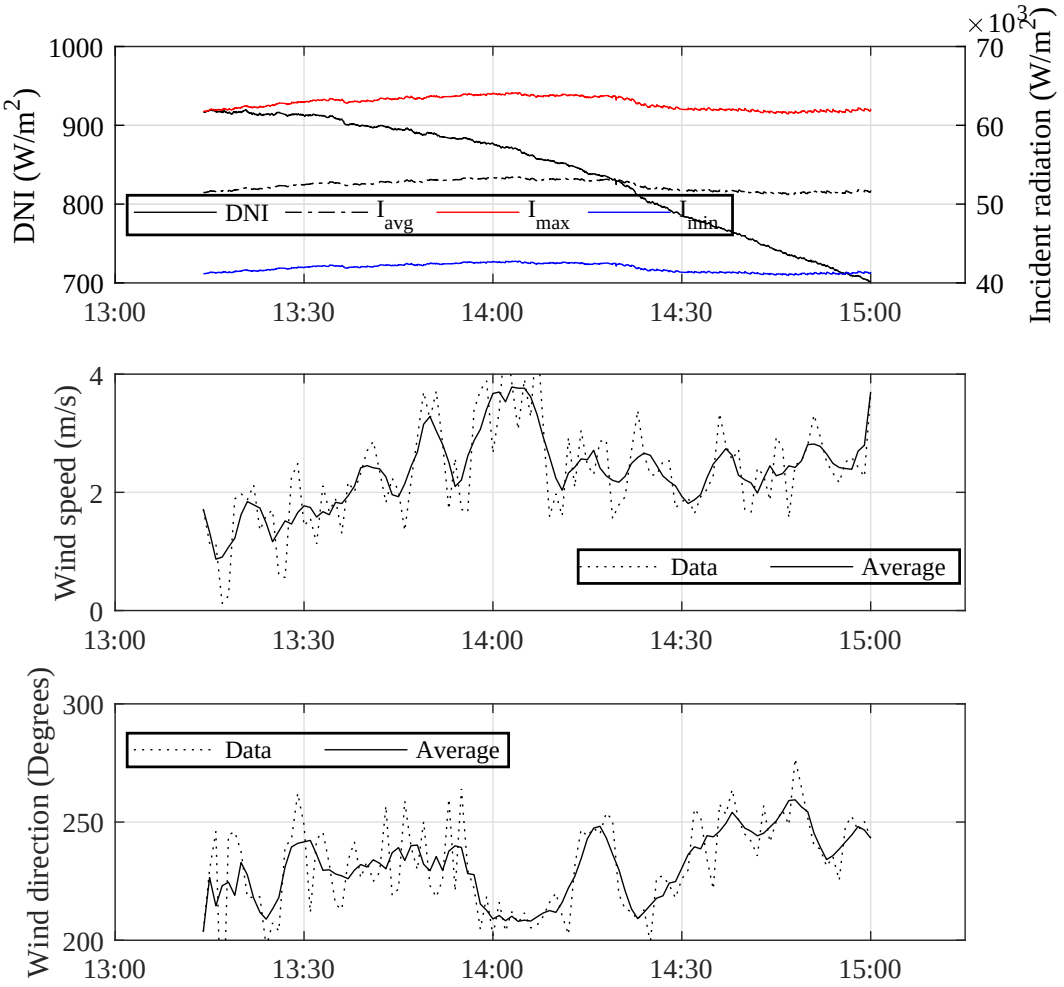

Figure 6.3: Irradiation and wind data for open annulus spike test

6.2 Finned annulus spike test data

Temperature and air mass flow rate data for the final finned annulus spike test are shown in Figure 6.4. During the test, air mass flow rates ranged from 0.022 kg/s to 0.133 kg/s. Air inlet temperatures fluctuated between 31.01 °C to 34.48 °C, following a similar ambient air temperature variation. A maximum and minimum air outlet temperature of 55.58 °C and 43.55 °C were also obtained at air mass flow rates of 0.0226 kg/s and 0.129 kg/s, respectively. Thermal images of the receiver base indicated similar temperatures as those experienced during the open annulus spike tests.

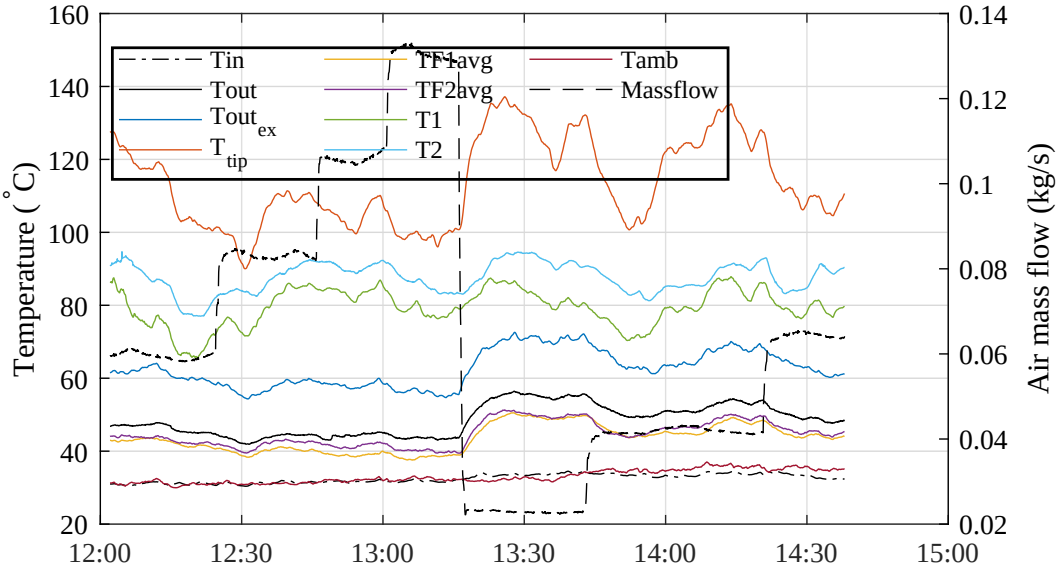

Figure 6.4: Finned annulus spike surface temperatures and air mass flow rates

From Figure 6.2, the rear surface temperatures, $T1$ and $T2$ remain significantly colder than those experienced on the open annulus spike. This is due to, firstly; the mounting flange blocking irradiation penetration to the rear of the spike and secondly; a lower finned section wall temperature and a corresponding axial conduction heat loss. As indicated in Appendix B, for the same air mass flow rate, the internal forced convection heat transfer coefficient is much higher for the triangular ducts than the open annulus, which would cause a corresponding lower wall temperature. It is also seen that the tip temperature generally approximates the same rear-most open annulus spike surface temperatures, indicating a comparatively high irradiation exposure. At low air mass flow rates, a maximum tip temperature of 137.2 °C is recorded, which is expected with a low internal forced convection heat transfer coefficient. The average finned section fin temperatures are also given, where $TF1$ and $TF2$ denote the 1st (front) 2nd (rear) finned sections, respectively.

Irradiation and wind data are given in Figure 6.5. During the test, a start, peak and end DNI of 1007 W/m^2, 1030 W/m^{2}and 840 W/m^2 are observed. A corresponding estimated irradiation on aperture of 52.73 kW/m^2, increasing to 59.27 kW/m^2 is also observed. Wind speed ranged from 0.48 m/s to 2.7 m/s, fluctuating around 2 m/s. Wind direction fluctuated between $300° - 200°$. Referring again to Figure 6.1, wind direction for the finned annulus test impinges on the rear of the receiver more frequently than the open annulus spike test. For the following analysis, only the crosswind component of the wind speed is used, where the normal direction of the spike is taken as roughly 210°.

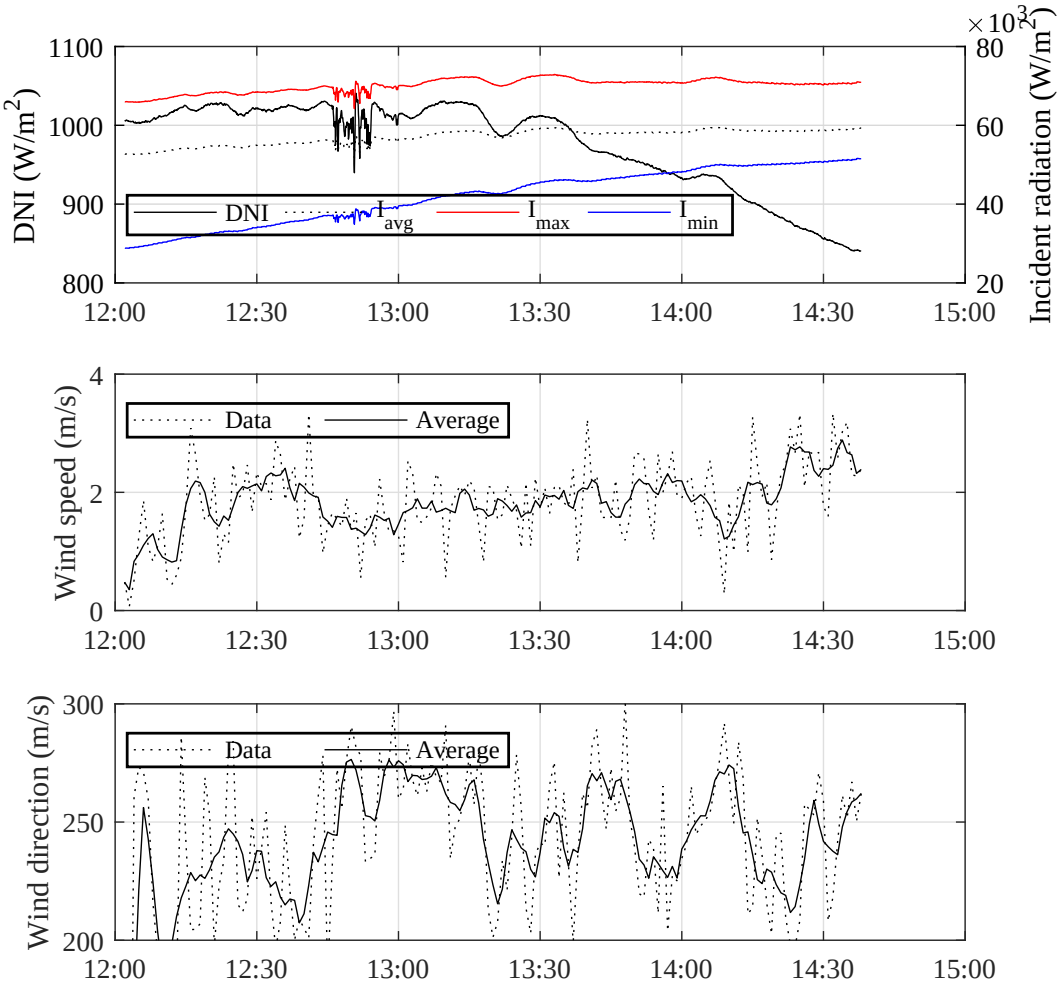

Figure 6.5: Irradiation and wind data for finned annulus spike test

6.3 Sensitivity analysis

To develop a better understanding of the impact of changing wind speed, air mass flow rate and irradiation concentration on receiver thermal efficiency, multivariable linear regression is applied to the experimental data. It is understood that radiative losses would also have an effect on thermal efficiency. Radiative losses are, however, difficult to characterize in this context and are not included in this sensitivity analysis. A general equation for thermal efficiency is generated as

$$\eta_{thermal} = \dot{m}^a V_{wind}^b \dot{Q}_{irrad}^c \tag{6.1}$$

Taking the natural logarithm of both sides of Equation 6.1 and separating the terms using the rules of logarithms yields

$$\ln(\eta_{thermal}) = a\ln(\dot{m}) + b\ln(V_{wind}) + c\ln(\dot{Q}_{irrad}) \tag{6.2}$$

which can be written in linear form as

$$y = ax_1 + bx_2 + cx_3 \tag{6.3}$$

The obtained coefficients are given are given in Table 6.1. From the coefficients for air mass flow rate, a, it first observed that increasing mass flow has the largest effect on increasing thermal efficiency, where increasing mass flow would yield an increased Reynolds number and better internal convection heat transfer from the spike wall. Comparing the open annulus and finned annulus coefficients for a, it is observed that the open annulus spike shows a better response to increased mass flow rates than the finned annulus spike. Increasing internal forced convection heat transfer coefficients in the finned annulus would lead to a reduction in fin efficiency - this is to say that where the open annulus spike might experience a linear efficiency increase, the finned annulus spike might experience a non-linear efficiency increase, where efficiency gain at higher flow rates are reduced.

Table 6.1: Linear regression model coefficients

Coefficient	Open annulus spike data	Finned annulus spike data
a	0.7469	0.6781
b	-0.3515	-0.0257
c	0.1792	0.1553
R^2	0.9037	0.9524

Comparing the coefficient b for both spikes, it is observed that the open annulus spike is increasingly sensitive to convective losses. In this context, the open annulus spike experienced more cross winds during the tests compared to the finned annulus spike test, where wind impingement was primarily on the rear of the receiver. Since the convective loss is also a function of the difference between spike surface temperature and ambient air temperature, lower spike wall temperatures would necessarily yield lower convective losses.

Comparing the coefficient c for both spikes, it is observed that a generally similar response to increasing irradiation is observed. Here, increasing irradiation concentration would lead to higher surface temperatures and, following from the previous argument, a higher temperature differential between internal air flow and spike wall. For both open annulus and finned annulus models, R^2 values of 0.9037 and 0.9524 were obtained, indicating a reasonable goodness-of-fit.

6.4 Open annulus spike surface temperature distribution

The temperature distribution on the open annulus spike surface for increasing air mass flow rates is given in Figure 6.6. The temperatures at the first three positions, namely $T1$, $T2$ and $T3$ are given as a fraction of the rear-most surface temperature, $T4$. Air outlet temperature is also given as a fraction of $T4$, where the air inlet temperature averaged around 34.5 °C.

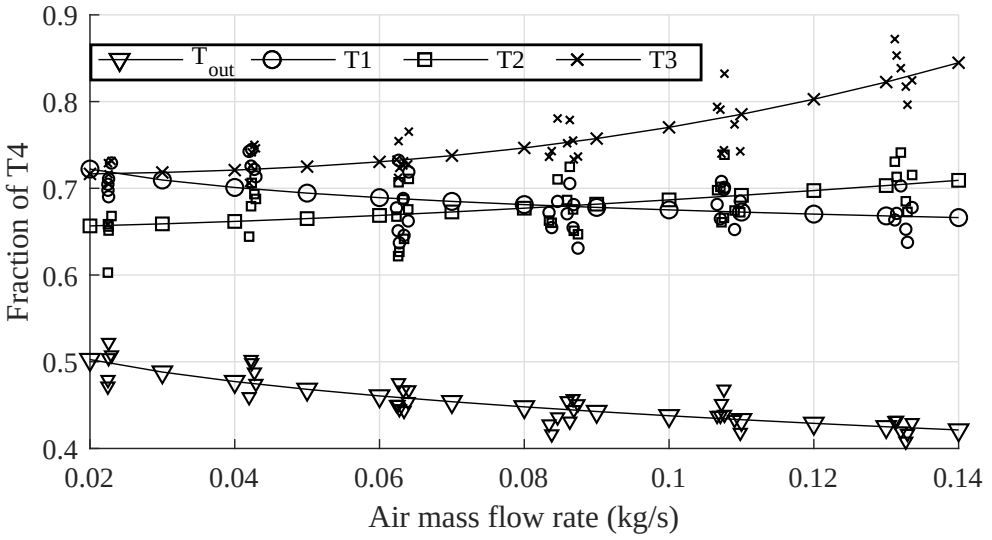

Figure 6.6: Average open annulus spike surface temperatures with second order power series trendlines

At low mass flow rates, an uneven temperature distribution is observed where the front-most surface temperature, $T1$, is hotter than the successive temperature behind it, $T2$. Since $T1$ is directly behind the tip, this indicates a high degree of axial conduction from the tip at low flow rates. This trend continues for mass flow rates below 0.085 kg/s, where an inflection occurs above 0.085 kg/s. This indicates that at mass flow rates above 0.085 kg/s, a sufficiently high convection heat transfer coefficient is reached at the tip inner wall such that the tip wall is sufficiently cooled. From Equation 4.31, this amounts to an average tip wall heat transfer coefficient of approximately 1340 $\mathrm{W/m^2K}$.

At high mass flow rates, where axial conduction from the tip is sufficiently reduced, the first two surface temperatures, $T1$ and $T2$, remain colder than the two rear surface temperatures, $T3$ and $T4$. This indicates a lower irradiation concentration on the front half of the spike surface. This is also observed for $T2$ at low flow rates. Here, $T2$ would not be as greatly influenced by axial conduction and consequently also shows low temperatures due to low irradiation concentration. The small temperature difference at higher mass

flow rates between $T1$ and $T2$, when compared to $T3$, also indicate similar levels of solar irradiation at $T1$ and $T2$.

Conversely, $T3$ and $T4$ remain the highest surface temperatures, indicating a higher irradiation concentration towards the rear of the spike. Since the receiver base also receives direct irradiation from the heliostat field, as opposed to the spike surface which receives irradiation at an oblique angle, the receiver base would also reach high temperatures. The high base temperature would also translate into axial heat conduction into the spike.

6.5 Irradiation concentration on spike surface

For the irradiation concentration profile, two options, shown in Figure 6.7, are investigated. The first profile, p_{sol1}, was obtained from the DO irradiation model presented in Section 4.6.2 for the case with a focal point 3 m behind the spike tip. A second profile, p_{sol2}, is derived from both the DO irradiation model and the experimental surface temperature data. p_{sol2} is given as

$$p_{sol2} = 0.16e^{-6.287l} + 0.023 \tag{6.4}$$

For a uniform irradiation on aperture from the DO irradiation model, an initial value of 2.3% is assumed at the front of the spike. The exponential term is obtained by fitting a curve to the average surface temperature growth from $T1$ to $T4$, shown in Figure 6.6, starting from $T1$. The final value of 16% is obtained when both curves are set to exhibit the same total irradiation input to the spike surface, within 1%.

The two given irradiation concentration profiles were tested using the open annulus spike 1-D model where validation data points were taken as the average values between two time points for the same air mass flow rate. To ensure that changes in thermal inertia due to changes in air mass flow are reduced, the time points are taken as the 5 minutes preceding an increase in air mass flow rate where the operation was closest to a perceived steady-state. For the open annulus model, the first case was chosen between 14:38 to 14:42 for an average air mass flow rate of 0.062 kg/s. Experimental data for the first case is given in Table 6.2. The 1-D model outputs for both irradiation concentration profiles are given in Table 6.2, Figure 6.8 and Figure 6.9. The 1-D model base and neighboring spike temperatures are set to assume the same temperature as the spike root.

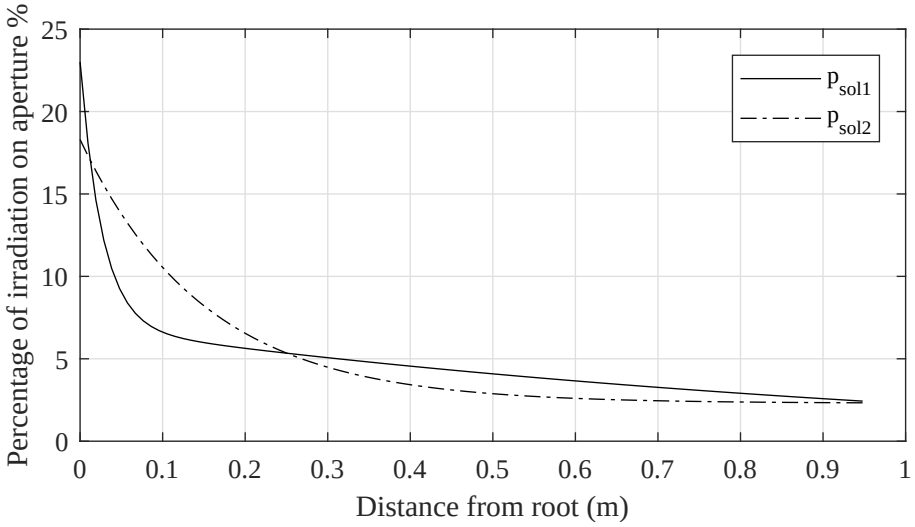

Figure 6.7: Comparison of irradiation concentration profiles, p_{sol1} and p_{sol2}, on spike surface

Table 6.2: Comparison of model output to measured experimental data for open annulus spike: Case 1

Parameter	14:38	14:42	Average	Model (p_{sol1})	Model (p_{sol2})
T_{amb} (°C)	29.18	29.35	29.26	-	-
$T_{air,in}$ (°C)	33.57	33.72	33.64	-	-
$T_{air,out}$ (°C)	56.93	58.83	57.88	59.85	56.62
T_1 (°C)	82.47	87.98	85.22	101.8	90.24
T_2 (°C)	79.39	87.25	83.32	112.7	69.61
T_3 (°C)	90.87	95.01	92.94	119.6	102.8
T_4 (°C)	127.60	128.90	128.30	132.6	129.4
$\dot{q}_{ap}$ (kW/m^2)	51.59	51.39	51.49	-	-
V_w (m/s)	2.625	1.987	1.779	-	-
V_θ (°)	254.1	245	-	-	-
$\dot{m}$ (kg/s)	0.0623	0.0617	0.062	-	-

For the first irradiation concentration profile, p_{sol1}, large variation is seen between the 1-D model and the experimental data, where maximum surface temperature variations of approximately 30 °C are seen at the spike center. This is primarily due to the high irradiation concentration at the spike root, which then also causes a large amount of axial conduction as well as thermal radiation from the base and neighboring spikes, increasing the average spike wall temperature. For p_{sol2}, less variation is seen, where the 1-D model surface temperatures vary with a maximum of approximately 10 °C. A second case

with an average air mass flow rate of 0.086 kg/s was also considered. It was found that p_{sol1} showed equal over and under prediction of wall temperatures of approximately 13 °C and p_{sol2} showed a maximum wall temperature over prediction of approximately 6 °C. The second case is presented in Section C.

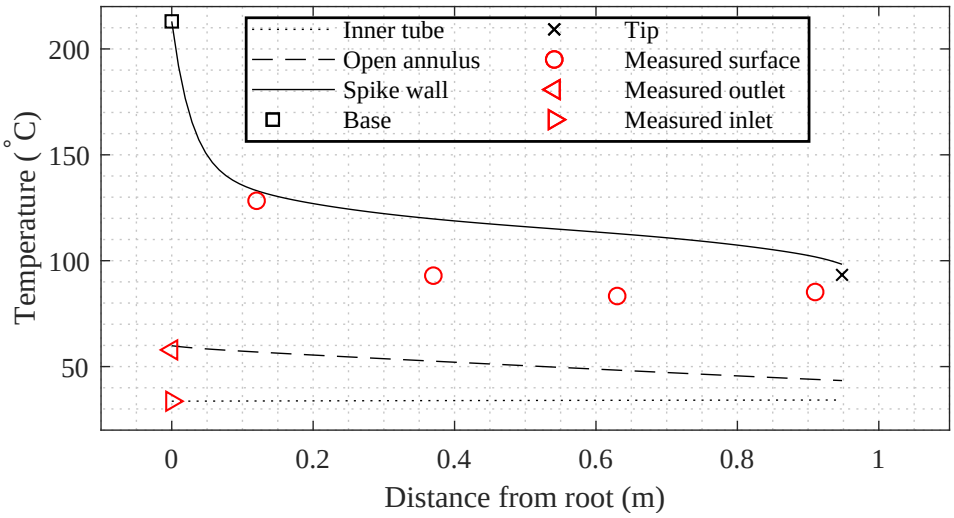

Figure 6.8: Open annulus 1-D model output with irradiation concentration profile p_{sol1}: Case 1

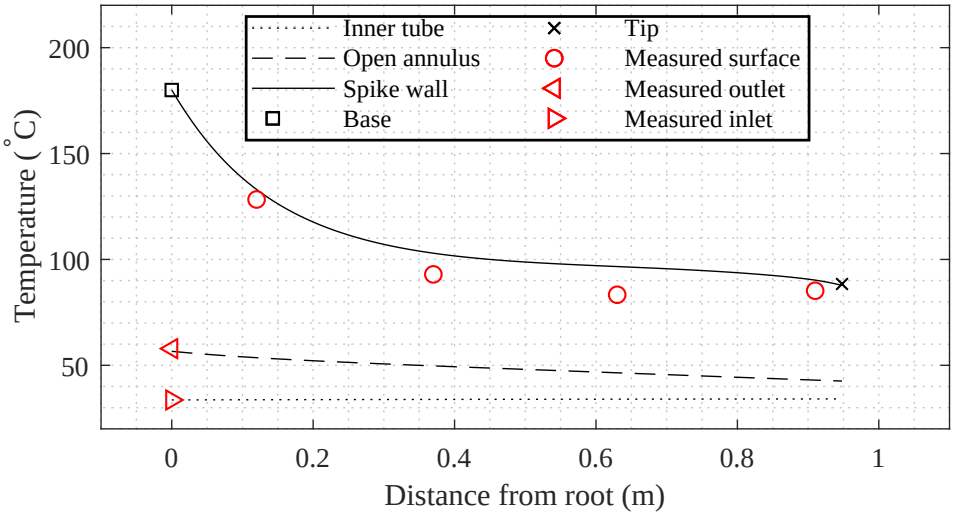

Figure 6.9: Open annulus 1-D model output with irradiation concentration profile p_{sol2}: Case 1

From both cases presented, it is seen that the irradiation concentration profile given by p_{sol2} gives a better approximation of the spike wall temperatures

and consequently air outlet temperature when used in the 1-D model, compared to p_{sol1}. Considering that p_{sol1} is based on an ideal case with a perfectly focused heliostat field, and that the two irradiation concentration profiles are not significantly different, it can be concluded that p_{sol2} is an appropriate approximation of the real irradiation concentration profile. Since the heliostat field cannot be perfectly focused during the tests, a lower irradiation concentration would be observed at the spike root due to lower irradiation reflection from the receiver base.

A higher irradiation input towards the rear of the spike would also be experienced as all the heliostats are not aimed directly at the ideal focal point. Irradiation reflection from the neighboring spikes would also contribute to some of the irradiation concentration at the rear of the spike. From the DO model, where the receiver base experiences 185% of the irradiation on aperture, the spike root experiences 22% of the irradiation on aperture. If a linear relationship is assumed, a conservative estimation can be made that the experimental receiver experiences approximately 153% of the irradiation on aperture at the base, giving 18.3% of the irradiation on aperture at the spike root.

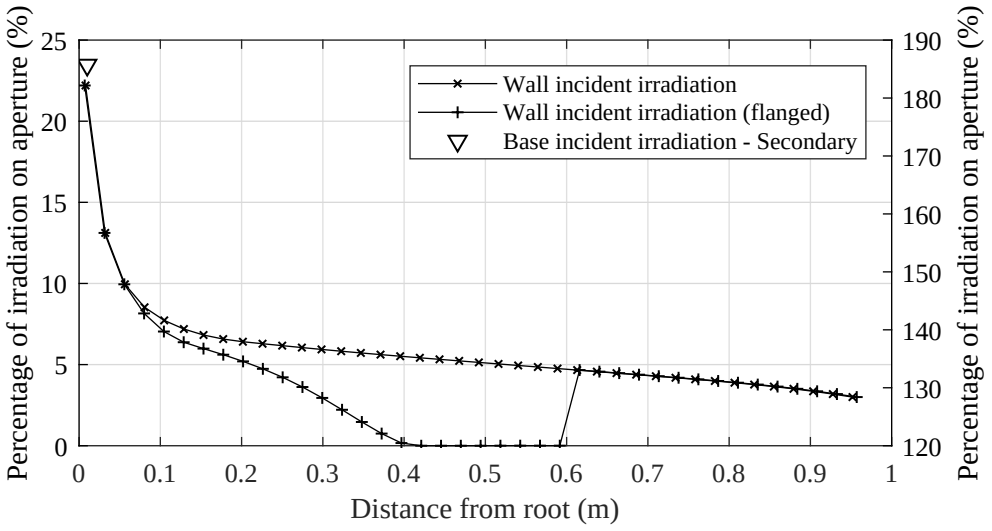

Figure 6.10: Surface incident radiation profiles for aperture focus points at 3 m behind the tip for the open and finned annulus spikes

To address the irradiation blocking of the finned annulus spike, the DO model was adapted to include a 15 mm high obstruction at the same position as the experimental spike. The irradiation concentration profile for the finned spike is shown in Figure 6.10. Here it is seen that the rear of the spike sees significantly less surface incident irradiation. For this case, an average surface incident irradiation of 42.87 W/m^2 is recorded, which amounts to 60.6% of the total un-flanged surface incident irradiation. By scaling the experimental

data accordingly, a more objective comparison between the two spike configurations is possible. Similar to the open annulus spike, two test cases were also considered with the flanged irradiation concentration profile as well as a discontinuous form of p_{sol2}. These cases are presented in Appendix C.

6.6 Spike fin temperature distribution

Temperature measurements inside the spike fins were taken at 4 circumferential positions. For the front finned section, closest to the tip, measurements were taken at 0° and 90°, where 0° is at the top of the spike and 90° is anticlockwise when facing the front of the receiver. For the rear finned section, measurements were taken at 90° and 180°. Temperature positions are depicted in Figure 6.11 and Figure 5.8. Temperatures were measured at depths of 23 mm, 12 mm and 8 mm into the fin, as measured from the spike wall. The naming convention used is: *T - (1st or 2nd) - (angular position) - (depth)*. Since the fins are coiled, each temperature measurement position corresponds to a different duct.

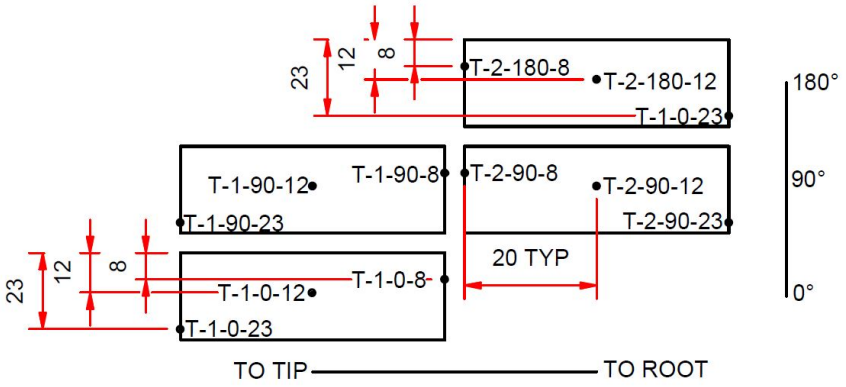

Figure 6.11: Depiction of fin temperature positions

The finned sections used in this project feature helically coiled fins, where the duct channel completes one half rotation for each finned section. This serves to increase heat transfer in the duct by inducing secondary flow patterns in the air as well as to avoid hotspots on the spike surface caused by non-uniform circumferential irradiation distribution. As described by Lubkoll (2017), these hotspots could cause a greater pressure drop in a particular duct, where choking occurs and leads to increased air flow in colder ducts, allowing the hot side of the spike to further overheat.

Figure 6.12 shows the fin temperature distribution for the front (1st) finned section. Air inlet temperature during the test fluctuated between 31.01 °C to 34.48 °C. It is initially observed that, for increasing mass flow, the average fin temperature decreases significantly where the maximum fin temperature at

$T-1-0-8$ decreases from 53 °C to 40 °C for mass flow rates of 0.02 kg/s to 0.14 kg/s, respectively. Also apparent is the increasing fin height temperature gradient. At a mass flow rate of 0.02 kg/s, a temperature difference of 3 °C is observed between the maximum and minimum fin temperatures whereas at 0.14 kg/s, a temperature difference of 5 °C is observed.

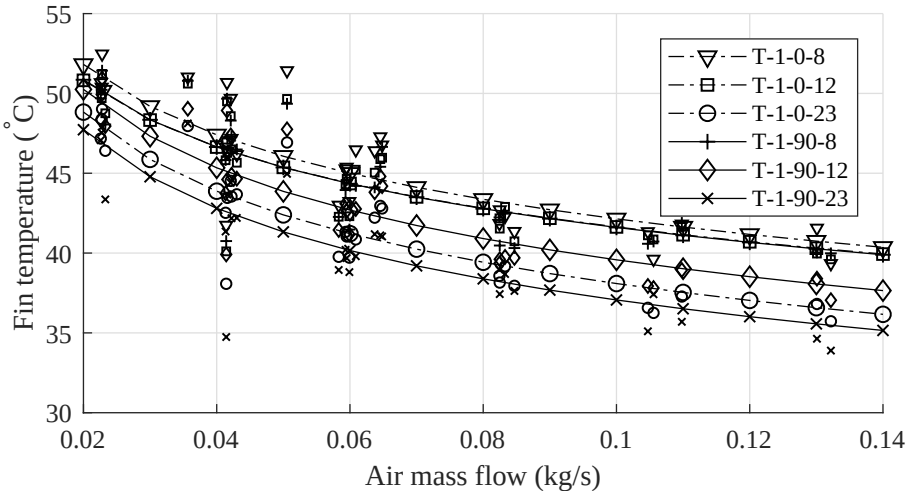

Figure 6.12: Fin temperature distribution in front finned section

Comparing both 0° and 90° temperature positions, slightly higher temperatures are observed for the 0° position, suggesting a higher irradiation concentration on the top of the spike. Comparing both 12 mm positions, it is observed that the fin at 0° shows a higher temperature than the fin at 90°, where $T-1-0-12$ generally approximates the same temperature as $T-1-90-8$. The higher temperature at $T-1-0-12$ indicates either a low mass flow in the particular duct or a higher irradiation concentration on the top of the spike.

Figure 6.13 shows the fin temperature distribution for the rear(2^{nd}) finned section. Comparing the fin circumferential temperature differences for the front and rear finned sections, smaller temperature differences are observed for the 90° and 180° positions for the rear finned section compared to the 0° and 90° positions for the front finned section. Since the rear finned section is further from the duct inlet, this indicates a more developed flow inasmuch as similar convection heat transfer coefficients would be observed, leading to similar temperature profiles. Higher temperatures are also observed for the 180° position, indicating a higher irradiation concentration at the bottom of the spike, compared to the side of the spike at 90°. Since the rear finned section would also experience higher irradiation concentrations, an increase in average fin temperatures is also observed. Figure 6.14 shows the fin height average temperature profiles for the rear finned section at 180°.

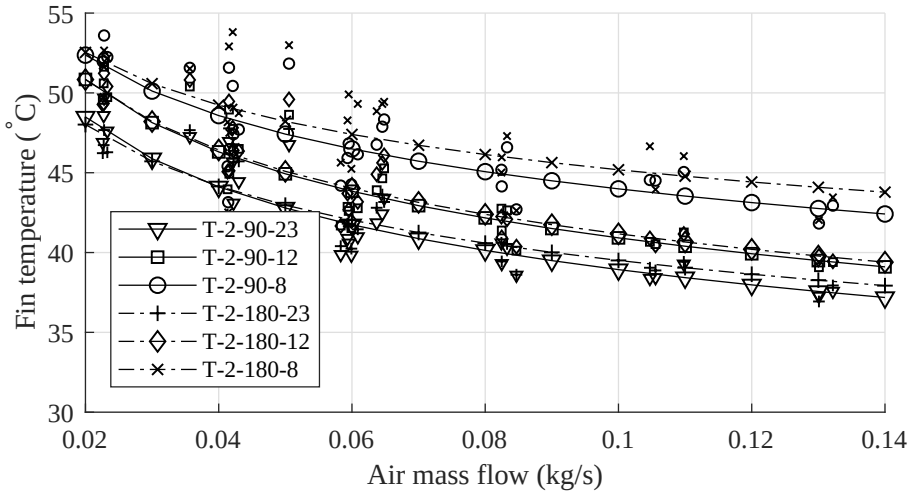

Figure 6.13: Fin temperature distribution in rear finned section

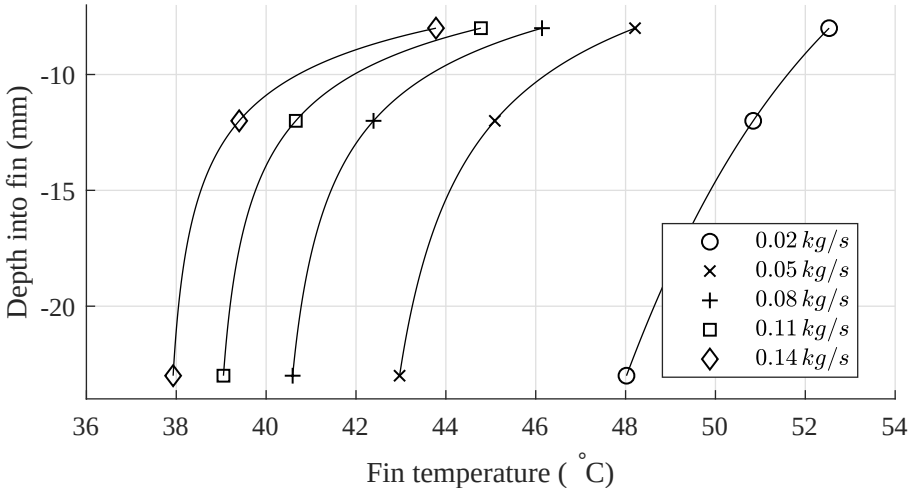

Figure 6.14: Fin height temperature profiles for increasing air mass flow rates

As air flow develops, the induced centrifugal force caused by the coiled duct pushes the air towards the spike wall. This leads to higher convection heat transfer coefficients at the wall surface and fin section closest to the wall. For the finned sections used here, the duct centroid, where the highest flow velocities would occur is at approximately -10 mm. As shown in Figure 6.14, a significant temperature difference is experienced by the fin between -8 mm and -12 mm at higher mass flow rates, indicating that the bulk of the heat removal from the fin occurs around the duct centroid. Since most of the heat is removed from the fin close to the spike wall, conduction into the fin is significantly reduced and the remaining fin surface area is underutilized.

While it is difficult to comment on the circumferential irradiation exposure on the spike surface during the tests, Figure 6.12 and Figure 6.13 show

that both the front and the rear finned sections experience reasonably similar temperatures at the respective circumferential positions. Where it may be expected that the highest circumferential temperature variations would be observed at low mass flow rates, where an uneven irradiation would be most evident, this is not the case and therefore the conclusion can be made that the coiled ducts show to be effective at equalizing the circumferential wall temperature distribution.

6.7 Thermal efficiency

From the definition of the spike aperture given in Section 4.6.1, the thermal efficiency can be calculated using

$$\eta_{thermal} = \frac{\dot{Q}_{out}}{I_{ap} A_{ap}} \tag{6.5}$$

where $\dot{Q}_{out}$ is the energy gain by the air and I_{ap} is the calculated irradiation at the aperture. For the finned spike data, the irradiation on aperture is scaled by 60.6%, as found from the developed DO radiation model. Figure 6.15 shows the thermal efficiency as a function of air mass flow rate. The bands around the average efficiency trend lines indicate the 20% variation in concentration factor, as shown in Figure 5.4.

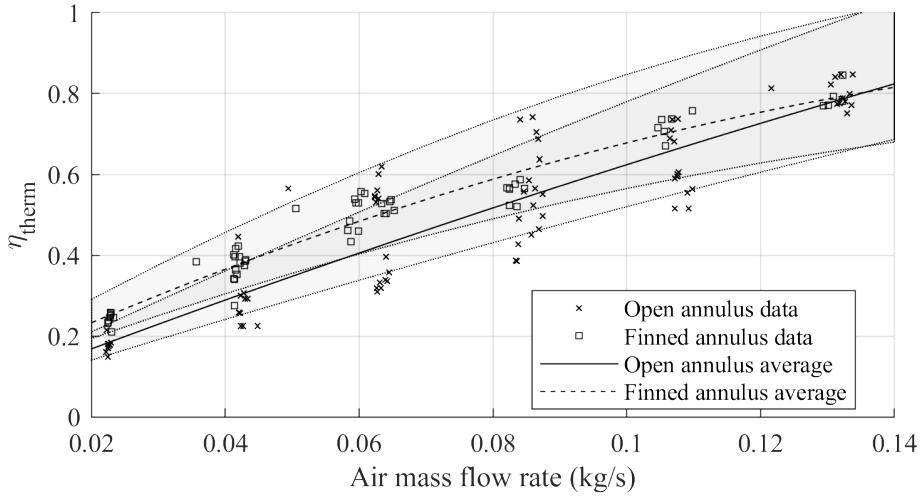

Figure 6.15: Spike thermal efficiency with increasing air mass flow rates

For the open annulus spike, the average thermal efficiency increases almost linearly, from 16% at 0.02 kg/s, to 82% at 0.14 kg/s. Distinct data clusters are seen above and below the average thermal efficiency trend line. These clusters represent the different thermal efficiencies at the wind speeds experienced during the test. For the finned annulus spike, a non-linear thermal efficiency

increase is seen, where the thermal efficiency increases from 23% at 0.02 kg/s, to 81% at 0.14 kg/s. It is seen that, as air mass flow increases, the spike fin efficiency decreases and that at 0.135 kg/s, both finned and open annulus spikes exhibit an 80% thermal efficiency. Due to the lower crosswind speeds experienced during the finned annulus spike test, less variation in thermal efficiency is observed.

Figure 6.16 shows the thermal efficiency as a function of cross wind speed. Trends are represented by least-squares fits. For the open annulus spike, the highest thermal efficiencies were obtained at low cross wind speeds, with a maximum thermal efficiency of 84% at a cross wind speed of 0.46 m/s. At increasing cross wind speeds, a significant decrease in thermal efficiency is seen, where a maximum thermal efficiency of 30% is observed at cross wind speeds of 3.95 m/s. It is also seen that below cross wind speeds of 1.5 m/s, the maximum thermal efficiency stays fairly constant at 84%, suggesting that an asymptotic efficiency is reached.

For the finned annulus spike, a minor reduction in thermal efficiency is seen for increasing cross wind speeds. This is due to, firstly; wind generally impinging on the rear of the receiver and secondly; lower overall surface temperature due to irradiation blocking at the rear of the spike.

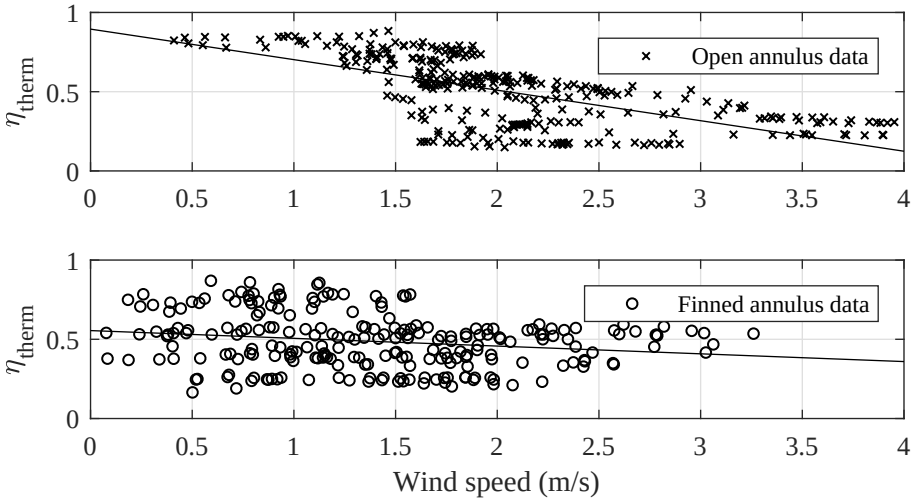

Figure 6.16: Spike thermal efficiency with increasing cross wind speeds

6.8 Conclusion on experimental results

From the experimental results it was found that, for a SCRAP spike in on-sun conditions, thermal efficiencies of above 80% are obtainable for both the open annulus and mixed finned/open annulus spikes. These efficiencies are, however, only attainable at low cross wind speeds, as it was shown that the spike is particularly susceptible to convective losses. By replacing the front 40% of

the spike with coiled fin sections, an average thermal efficiency increase of 8% was obtained at lower air mass flow rates. With increasing air mass flow rates, this efficiency gain is diminished where, at 0.135 kg/s both spike configurations assume the same thermal efficiency. This low efficiency gain is only due to the low irradiation concentration at the front of the spike. It would be expected that for a fully finned spike, the higher convection heat transfer in the ducts would be better able to remove heat from the spike wall closer to the root, resulting in a higher thermal efficiency.

From the developed DO model, it was found that for a perfectly focused heliostat field, irradiation concentration at the receiver base was significantly higher than the average irradiation at the receiver aperture. The high irradiation concentration at the receiver base would lead to high material temperatures, as well as increased thermal radiation and irradiation reflection to the spike root. During the test, the exhaust temperature averaged around 10 °C to 15 °C above the spike outlet temperature, and in some cases, contributing around 50% of the total heat transfer between air inlet and exhaust outlet, indicating base surface temperatures higher than those experienced on the spike surface. Flow separation from the base inside the manifold would also lead to poor cooling of the base.

In the context of the implementation of a full-scale receiver, the sensitivities to convective losses due to wind and high irradiation concentration at the receiver base poses some practical problems. From the presented temperature data for both spikes, the tip and spike root generally assume the highest temperatures on the spike. When exposed to changing wind speeds and direction, large swings in material temperature would be observed leading to unintended thermal cycling of the material and fatigue over long term operation.

In the case of the spike root, this would be problematic as the root would be considered a critical structural component. Another concern is the high cooling rate at the tip. Where convective losses will inevitably affect the tip, changes in irradiation exposure are also of concern, which may arise from tracking errors from the heliostat field, wind loading on the heliostats or, more trivially, cloud cover. In the case where irradiation is unexpectedly removed from the tip, the high cooling rate would rapidly cool the tip material which would induce more severe thermal cycling than that seen at the spike root.

If the same tip heat transfer philosophy is applied to the receiver base inside the manifold, in the sense that high cooling rates are required so as not to exceed the material temperature limits, similar cooling rates would be required inside the manifold, if not higher, than those obtained at the tip. This would negatively affect the total pressure drop across the receiver when a sub-30 kPa pressure drop is desired.

A practical solution to mitigating the high temperature swings at the spike root and receiver base may be to firstly implement baffles between spikes at different locations on the receiver. This would result in a "honeycomb-like" structure, where it would be entirely possible to eliminate the majority of the

convective losses by reducing wind speeds close to the spike root and receiver base. Since the baffles would not be considered a structural component, it could be manufactured from reasonably thin materials to reduce the overall receiver weight. The only concern in this case would be increased wind loading on the receiver which would also negatively affect the requirements for the receiver tower. Secondly, the root and base could be coated with a reflective paint that would limit the irradiation absorption. In this scenario, more irradiation would also be reflected to the spike surface.

Also of interest is the scalability of manufacturing finned spikes. For the finned sections used in Lubkoll (2017), wire cutting was used where manufacturing costs for 314 mm of finned section totaled to ZAR 18,639 excluding material cost. For the finned sections used in this work, 3-D printing was used where the total material and manufacturing costs amounted to approximately ZAR 120,000 for 400 mm of finned section. Both wire cutting and 3-D printing are unsuitable for large scale manufacturing as well as prohibitively expensive for manufacturing the amount of spikes required for a full scale receiver. Another viable, large scale manufacturing alternative would be metal extrusion. It is uncertain, however, if the same coiled duct configurations would be obtainable, as well as whether the use of high temperature nickel-base alloys such as Inconel would be suited to metal extrusion.

A final concern is the practical manufacturability and maintainability of a full-scale SCRAP receiver. Owing to the general inaccessibility of the manifold system, a high degree of modularity would be required in the final receiver design so that the receiver could be assembled and serviceable. The high degree of modularity would invariably increase manufacturing costs as well as complexity of the final design. In the case of previous pressurized air receivers discussed in Section 3, it is advisable that manufacturing and design complexity be avoided where possible as complex aspects of the receiver design generally exhibit the first failure points.

Chapter 7

Performance of a SCRAP spike in on-sun conditions

After validating the 1-D numerical model in Section 6.5 and Appendix C, a prediction can be made of the performance of a fully finned spike under the experimental conditions experienced. The finned spike's thermal efficiency is also compared to that of an open annulus spike under experimental conditions. A sensitivity analysis is conducted on the finned spike geometry to determine how to best improve spike performance.

7.1 Spike performance

An air mass flow rate of 0.08 kg/s at an inlet temperature of 30 °C is used with an average irradiation on aperture of 50 kW/m^2. The ambient air temperature is set at 30 °C with a cross wind speed of 2 m/s. Both the base and surrounding spike surface temperatures are fixed at 150 °C. An outlet pressure of 101.3 kPa is specified at the exhaust outlet.

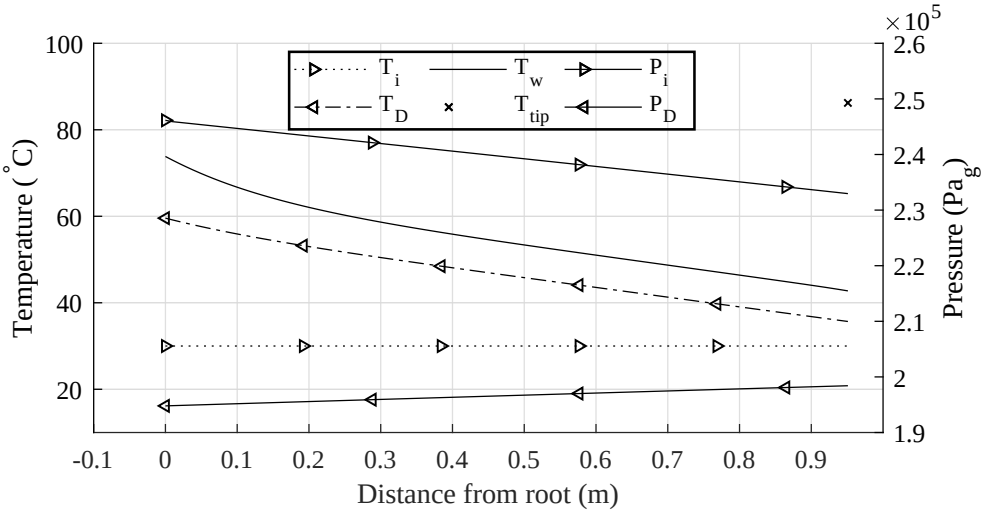

Figure 7.1: Temperature and pressure distribution inside finned annulus spike

Figure 7.1 shows the air temperature distribution inside the spike as well as the spike wall temperature. Air enters the spike at 30 °C, with no increase in temperature as it travels to the tip, due to the low contact surface at the triangular duct root. At the tip, the air temperature increases to 35.67 °C, where

the tip temperature is 86 °C. As the air travels through the triangular duct, it experiences a further increase in temperature, exiting the spike at 59.57 °C. At the spike wall just behind the tip, the wall temperature is 42.75 °C. For the front 70% of the wall, temperature increases almost linearly which is also seen in the duct air temperatures. At the rear of the spike, temperature starts to increase exponentially, where the spike root temperature is at 73.83 °C, due to the higher irradiation concentration at the root as well as thermal radiation from the base and neighboring spikes. The exponential air temperature increase is also observed, although not as notable as the spike wall.

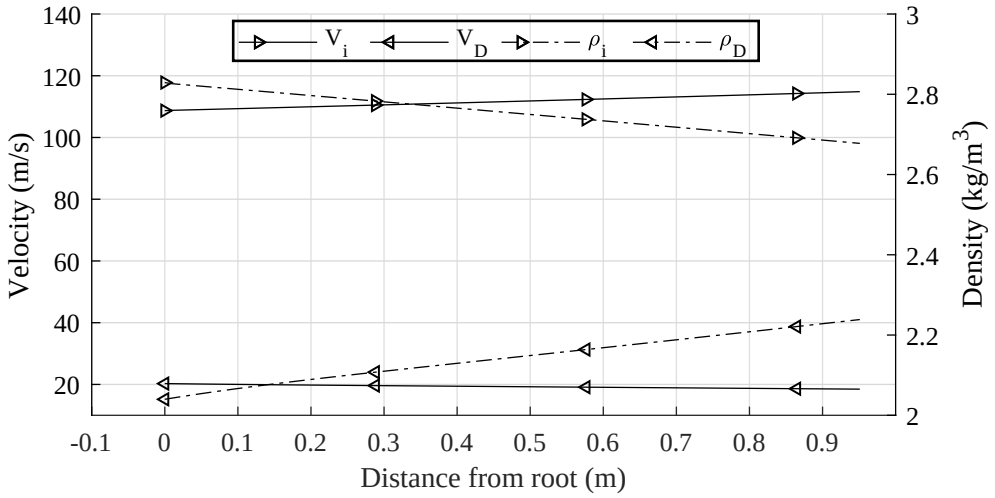

Figure 7.2: Velocity and density distribution inside finned annulus spike

Air enters the inner tube at a total pressure of 246.61 kPa with a velocity of 108.7 m/s and density of 2.829 kg/m^3, as shown in Figure 7.1 and Figure 7.2. Due to the small diameter of the inner tube, and consequently high flow velocity, a large pressure drop due to wall friction occurs across the inner tube. As the pressure in the inner tube decreases, a decrease in air density also occurs which leads to an increase in flow velocity. Air exits the inner tube at 233 kPa with a flow velocity of 114.8 m/s and density of 2.678 kg/m^3. At the tip, the air turns through 180°. The combined change in direction and temperature increase leads to a pressure drop at the tip from 233 kPa to 198.4 kPa. The pressure drop at the tip leads to a change in density from 2.678 kg/m^3 to 2.239 kg/m^3.

Due to the higher combined flow area of the outer annulus, air enters the triangular duct with a flow velocity of 18.74 m/s. As air flows through the triangular ducts, it experiences a pressure drop due to wall friction. It is also heated, which leads to further expansion and a corresponding reduction in density. The combined friction pressure drop and heating causes the air to accelerate, exiting the triangular ducts at a flow velocity of 20.27 m/s at 194.8 kPa

and a density of 2.04 kg/m^3. The remaining pressure drop of 93.5 kPa is experienced across the air manifold and exhaust where the air exits at atmospheric pressure.

With an air mass flow rate of 0.08 kg/s and cross wind speed of 2 m/s, the spike operates at a thermal efficiency of 89.9%. Figure 7.3 shows the thermal efficiency of the finned spike at changing cross wind speeds. With no cross wind, a maximum thermal efficiency of 94% is reached. At a cross wind speed of 4 m/s, an 8% reduction is seen where thermal efficiency is 86.2%. Compared to the open annulus spike which operated at thermal efficiencies in the range of 73% to 42% for cross wind speeds of approximately 0.5 m/s to 2 m/s, the finned annulus spike shows a significant increase in thermal efficiency.

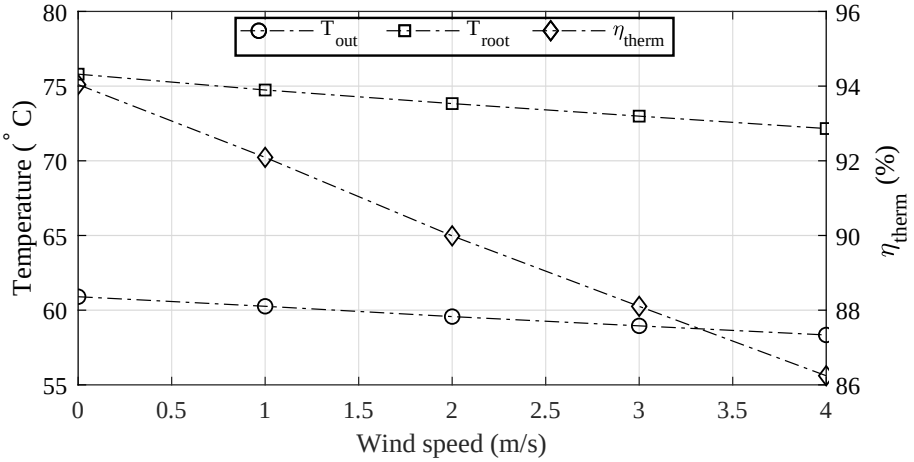

Figure 7.3: Sensitivity to wind speed

7.2 Sensitivity analysis

At the conditions given for the finned annulus spike performance case, the total pressure drop across the spike is 51.3 kPa with an air outlet and spike root temperature of 59.57 °C and 73.83 °C, respectively. Using the 1-D model, changes can be made to the spike internal geometry to determine the best way to reduce the total pressure drop across the spike, while also increasing the air outlet temperature and reducing the spike root temperature.

Figure 7.4 shows the pressure and temperature variation inside the spike for increasing and decreasing the number of fins from 20 fins. The pressure drop at the inner tube, duct and tip is given as a ratio of the total pressure drop across the spike. The total pressure drop is expressed as a fraction of the pressure drop across the spike with 20 fins. By increasing or decreasing the number of fins, a near linear pressure relationship is observed, where an increase in fins would yield higher frictional pressure losses due to the increased surface area as well as increased flow velocity. By reducing the number of fins, the heat

transfer surface at the wall increases where the air is increasingly exposed to the hotter wall surfaces as opposed to the colder fins.

The remaining fins would still serve to induce swirl so as to force the air flow closer to the wall. The larger exposed wall surface leads to a higher heat transfer rate, increasing the air outlet temperature as well as reducing wall surface temperature. By increasing the number of fins, a similar increase in air outlet temperature is seen, however, since the fin surfaces would be colder than the wall, the rate of heat transfer from the fins is lower than that at the wall. As a result, heat is not removed from the wall as effectively and an increase in wall temperature is observed. It is seen that increasing or reducing the number of fins does not significantly affect the overall performance of the spike, and it may therefore be more effective to use only enough fins that would induce the necessary air flow swirl.

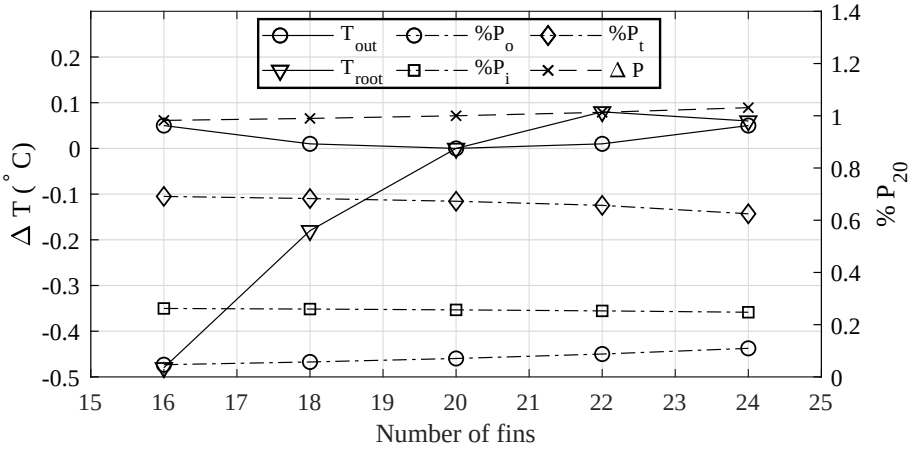

Figure 7.4: Sensitivity to number of fins

Figure 7.5 shows the pressure variation inside the spike for increasing inner tube diameter. By increasing the inner tube diameter, a significant pressure drop reduction is observed initially. At the initial inner tube diameter of 18.2 mm, the majority of the pressure drop occurs across the tip, due to the large velocity gradient between the inner tube and outer annulus. The second largest pressure drop occurs across the inner tube, due to the high flow velocity and consequent high frictional pressure loss. Increasing the inner tube diameter would necessarily also decrease the triangular duct flow area, however, since the flow velocity in the triangular duct is initially quite low the increase in flow velocity would not immediately equate to a great increase in pressure drop. The lowest total spike pressure drop occurs with an inner tube diameter between 36 mm 42 mm, where the total pressure drop across the spike is 8.52 kPa. Here, the majority of the pressure drop occurs across the triangular ducts and the pressure drop across the inner tube and tip is almost equal.

Further increasing the inner tube diameter leads to an increase in pressure drop in the ducts that would increase the total spike pressure drop.

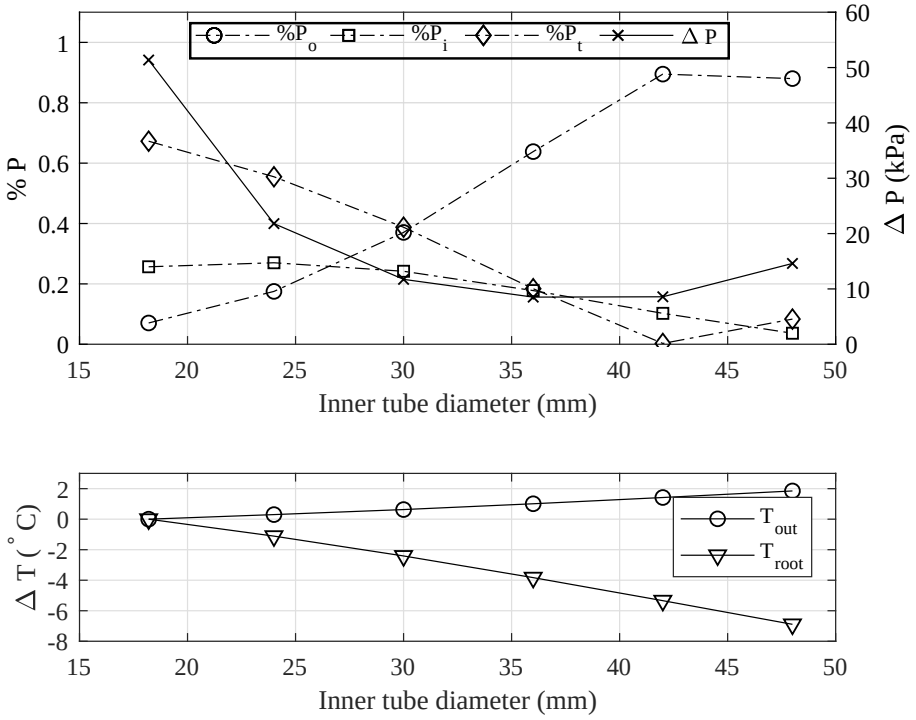

Figure 7.5: Pressure and temperature sensitivity to inner tube diameter

Consequently, by increasing the inner tube diameter, higher heat transfer coefficients occur in the duct, increasing air outlet temperature and reducing wall temperatures. Compared to increasing the amount of fins, increasing the inner tube diameter has a much greater positive effect on overall spike performance.

7.3 Conclusion

At similar operating conditions, the finned annulus spike outperforms an open annulus spike by a significant margin. Due to the lower surface temperatures on the finned annulus spike, the spike shows less sensitivity to convective losses. A sensitivity analysis on the spike geometry showed that by increasing the inner tube diameter, the highest gains are achieved where a significant pressure drop reduction is obtained across the spike with lower spike root temperatures and increased air outlet temperatures. The lower pressure drop across the spike would be beneficial in obtaining a sub-30 kPa pressure drop across the receiver and the higher heat transfer coefficients could reduce the wall temperatures to below the maximum material operating limits.

Chapter 8

Conclusions and recommendations

The experimental investigation conducted sought to test a single spike of the SCRAP receiver in on-sun conditions. To this end, an experimental receiver approximating a full scale receiver was developed and tested on-sun at the Helio40 facility at the Department of Mechanical and Mechatronic Engineering at the University of Stellenbosch.

Conclusions

A review of existing pressurized air receivers was conducted to gain a broader insight of what factors lead to the successful operation of past receivers. The experimental receiver was tested in on-sun conditions and a set of experimental data was obtained for the spike performance with a range of environmental variables.

Using an empty annulus spike configuration, along with the developed 1-D numerical model and a DO irradiation model, a correlation was found that would characterize the irradiation concentration on the spike surface. From thermal images of the receiver at operating conditions, as well as the DO radiation model and irradiation concentration correlation, the irradiation concentration at the receiver base could be quantified.

Using finned annulus spike sections provided for this project, the effect of the internal fins on total heat transfer was investigated. Finally, the developed 1-D numerical model was used to predict the performance of a full-length finned spike at the conditions experienced through the experimental tests.

Key findings

It was found that the irradiation concentration on the spike surface could be characterized as

$$p_{sol} = 0.16e^{-6.287l} + 0.023 \tag{8.1}$$

given as a percentage of the irradiation at the spike aperture where l is defined as 0 at the spike root. The exponent value is determined by irradiation reflection from neighboring spikes as well as the aiming accuracy of the heliostat field. The initial and final concentration values would be dependent on heliostat size and curvature as well as the aiming accuracy of the heliostat field. The total irradiation at the base of the receiver could be estimated as 153%

of the irradiation at the spike aperture. When coupled with flow separation from the receiver base inside the receiver manifold, this would lead to high temperatures exceeding the material operating range in a full-scale receiver. Further, it was found that the SCRAP spike is sensitive to convective losses, where the highest thermal efficiencies could only be obtained below cross wind speeds of 1.5 m/s

The internal finned sections used for this project were capable of increasing the total thermal efficiency of the spike by approximately 8% at low air mass flow rates. With a reduction in fin efficiency at increasing air mass flow rates, both open annulus and finned annulus spikes exhibit the same thermal efficiency at 0.135 kg/s. Due to the centrifugal force induced by the coiled ducts, the highest flow velocities and heat transfer coefficients would be observed closer to the duct centroid and spike wall. As the bulk of the heat is removed from the spike wall and the fin section closest to the wall, the remaining fin length is underutilized. It was found, however, that the swirled ducts did serve to equalize the spike circumferential temperature distribution. This is quite significant as it would serve to reduce hotspots along the spike length, preventing overheating and subsequent choking, as described by Lubkoll (2017).

From the prediction of the full length finned spike it was found that air outlet temperatures of approximately 60 °C are attainable for an irradiation on aperture of 50 kW/m^2 with a cross wind speed of 2 m/s and an air mass flow rate of 0.08 kg/s. This equates to a thermal efficiency of 89.9%, which is a significant improvement in performance compared to the open annulus spike. A sensitivity analysis on the spike geometry showed that with increasing the number of fins, a small increase in air outlet temperature was obtained, at the expense of an increased pressure drop across the spike. The sensitivity analysis also showed that by increasing the inner tube diameter, the total spike pressure drop could be reduced significantly, which would be beneficial in reaching a sub-30 kPa receiver pressure drop for implementation in a solarized Brayton cycle. By increasing the inner tube diameter, higher heat transfer coefficients are obtained in the duct. This serves to increase the outlet air temperature and reduce the spike wall temperatures. Increasing the inner tube diameter will also decrease fin height, which will decrease the underutilization of fin surface area with the benefit of less material usage.

Future work

In the South African context of solar power, the advantages of CSP have been outweighed by the lower cost of PV over recent years, and this will likely be the case for the short to mid-term future. In the current CSP market, PT technology is also favored for its simplicity when compared to Central Tower technology. It is therefore of interest that Central Tower CSP research focusses on cost effective and practical solutions to advancing the CSP field.

In its thermally efficient form, the SCRAP receiver struggles to meet the financial and practicality benchmark, where tubular cavity receivers such as the SOLUGAS receiver discussed in Section 3.7.2 would yield comparable levels of thermal performance at a lower financial cost, with the benefit of having been proven to be commercially viable. Here, resources may be better invested in investigating similar concepts with less prohibitive design constraints than that of the SCRAP receiver. Therefore, before further work is conducted on the SCRAP receiver, it is recommended that an objective discussion is required by the relevant shareholders of the SCRAP concept to determine its practical and economical feasibility.

In the interest of research continuity, some of the ideas discussed in Section 6 could be further investigated. This would include;

- Investigation into suitable ways to minimize the convective losses from the SCRAP spikes. Baffles between spikes at different locations on the receiver are suggested. The effectiveness of this method would need to be verified through CFD modelling of a sector of the SCRAP receiver with a range of impingement angles. The effects of wind loading on the receiver tower would also need to be investigated.

- Investigation into a suitable method to reduce spike root and receiver base temperatures. It was suggested that the use of reflective paint may be effective in limiting irradiation absorption by the base, serving to reflect irradiation back to the spike surface. It would need to be verified whether this has an overall negative effect on total receiver performance and whether the desired results are obtained.

- Optimization of fin/duct geometry to enhance heat transfer while maintaining a low pressure drop across the ducts. The coiled duct configurations work in tandem with the fins, where the fins provide a larger heat transfer surface area as well as force airflow towards the spike wall. An investigation is required to find the optimum amount of fins required, as well as fin shape and coil pitch, to utilize both of these mechanisms to their maximum potential.

- Investigation into cost effective methods of manufacturing thermally efficient SCRAP spikes. The possibility of metal extrusion has been suggested, however, further research would be required to determine whether this is possible with high temperature nickel-base alloys envisaged for use in the full-scale receiver.

List of References

Abengoa, 2016 (2016). Abengoa, idc and khi community trust commence commercial operation of khi solar one, the first solar tower plant in africa. [Online] [Accessed on 01.08.2019].
Available at: `http://www.abengoa.com/web/en/noticias_y_publicaciones/noticias/historico/2016/02_febrero/abg_20160205`

Allen, K.G. (2010). *Performance characteristics of packed bed thermal energy storage for solar thermal power plants*. Master's thesis, Stellenbosch University.
Available at: `https://scholar.sun.ac.za`

Amsbeck, L., Buck, R., Heller, P., Jedamski, J. and Uhlig, R. (2008). Development of a tube receiver for a solar-hybrid microturbine system. In: *Proceedings of 14th SolarPACES Conference, Las Vegas, NV, March*, pp. 4–7.

Avila-Marin, A.L. (2011). Volumetric receivers in solar thermal power plants with central receiver system technology: a review. *Solar energy*, vol. 85, no. 5, pp. 891–910.

Basson, E.J.J. (2019). *Development and testing of an externally finned tube cavity receiver for Brayton cycle preheating purposes*. Master's thesis, Stellenbosch University.
Available at: `https://scholar.sun.ac.za`

Bode, S.-J. and Gauché, P. (2012). Review of optical software for use in concentrating solar power systems. In: *Proceedings of South African Solar Energy Conference*.

Buck, R., Brauning, T., Denk, T., Pfander, M., Schwarzbozl, P. and Tellez, F. (2002 February). Solar-hybrid gas turbine-based power tower systems (refos). *Journal of Solar Energy Engineering (Transactions of the ASME)*, vol. 124, no. 1, pp. 2–9. ISSN 0199-6231.
Available at: `http://search.proquest.com/docview/20865059/`

Çengel, Y. and Cimbala, J. (2014). *Fluid mechanics: fundamentals and applications*. McGraw-Hill Higher Education.

Çengel, Y. and Ghajar, A. (2015). *Heat and mass transfer: fundamentals and applications*. McGraw-Hill Higher Education.

Çengel, Y.A. and Boles, M.A. (2006). *Thermodynamics : an engineering approach*. 5th edn. McGraw-Hill Higher Education.

Chai, J. and Patankar, S. (2006). Discrete-ordinates and finite-volume methods for radiative heat transfer. In: *Handbook of Numerical Heat Transfer*, 2nd edn. John Wiley & Sons.

Chu, S., Bai, F., Zhang, X., Yang, B., Cui, Z. and Nie, F. (2018). Experimental study and thermal analysis of a tubular pressurized air receiver. *Renewable energy*, vol. 125, pp. 413–424.

Craig, K., Meyer, J.P. and Le Roux, W.G. (2015). Computational fluid dynamics analysis of parabolic dish tubular cavity receiver. 3rd Southern African Solar Energy Conference, South Africa, 11-13 May, 2015.

Craig, T.O., Brent, A.C. and Dinter, F. (2017*a*). *Concentrated solar power (CSP) innovation analysis in South Africa*. Southern African Institute for Industrial Engineering.

Craig, T.O., Brent, A.C. and Dinter, F. (2017*b*). *The current and future energy economics of Concentrating Solar Power (CSP) in South Africa*. Southern African Institute for Industrial Engineering.

Department of Energy (2015). Strategic plan: 2015-2020. [Online] [Accessed on 02.06.2018].
Available at: `http://www.energy.gov.za/files/aboutus/DoE-Strategic-Plan-2015-2020.pdf`

Department of Energy (2019). Integrated resource plan (irp2019). [Online] [Accessed on 11.1.2019].

Dirker, J. and Meyer, J. (2004). Convection heat transfer in concentric annuli. *Experimental heat transfer*, vol. 17, no. 1, pp. 19–29.

Dittus, F. and Boelter, L. (1930). University of california publications on engineering. *University of California publications in Engineering*, vol. 2, p. 371.

Duffie, J.A. and Beckman, W.A. (2006). *Solar engineering of thermal processes*. 3rd edn. Wiley, Hoboken, N.J. ISBN 0471698679.

Fluri, T.P. (2009). The potential of concentrating solar power in south africa. *Energy Policy*, vol. 37, no. 12, pp. 5075 – 5080. ISSN 0301-4215.
Available at: `http://www.sciencedirect.com/science/article/pii/S0301421509005308`

Freudenstein, K. and Karnowsky, B. (1987). Volumetric ceramic receiver cooled by open air flow-feasibility study. In: *Solar Thermal Energy Utilization*, pp. 1–55. Springer.

Gnielinski, V. (1976). New equations for heat and mass transfer in turbulent pipe and channel flow. *Int. Chem. Eng.*, vol. 16, no. 2, pp. 359–368.

Grobbelaar, D. (2019). *Improving the heat transfer characteristics of a Spiky Central Receiver Air Pre-heater (SCRAP) using helically swirled fins*. Master's thesis, Stellenbosch University.
Available at: `https://scholar.sun.ac.za`

Grobler, A. (2015). *Aiming strategies for small central receiver systems.* Master's thesis, Stellenbosch University.
Available at: `https://scholar.sun.ac.za`

Grotjans, H. and Menter, F. (1998). Wall functions for industrial applications. *Computational fluid dynamics*, vol. 98, no. 1, pp. 1112–1117.

Heller, L. (2017). *Development of a dual-pressure air receiver system for the SUNDISC cycle.* Ph.D. thesis, Stellenbosch University.
Available at: `https://scholar.sun.ac.za`

Howell, J.R. (1982). *A catalog of radiation configuration factors.* McGraw-Hill.

International Energy Agency (2015). South africa: Electricity and heat for 2015. [Online][Accessed on 02.06.2018].
Available at: `http://www.iea.org/classicstats/statisticssearch/`

Joubert, H. (2019). *Development of a Web-based Control System for a Heliostat Test Facility.* Master's thesis, Stellenbosch University.
Available at: `https://scholar.sun.ac.za`

Kakaç, S., Shah, R.K. and Aung, W. (1987). Handbook of single-phase convective heat transfer.

Korzynietz, R., Brioso, J., del RÃo, A., Quero, M., Gallas, M., Uhlig, R., Ebert, M., Buck, R. and Teraji, D. (2016). Solugas - comprehensive analysis of the solar hybrid brayton plant. *Solar Energy*, vol. 135, pp. 578 – 589. ISSN 0038-092X.
Available at: `http://www.sciencedirect.com/science/article/pii/S0038092X16301992`

Kribus, A., Doron, P., Rubin, R., Karni, J., Reuven, R., Duchan, S. and Taragan, E. (1999). A multistage solar receiver:: The route to high temperature. *Solar Energy*, vol. 67, no. 1-3, pp. 3–11.

Kribus, A., Doron, P., Rubin, R., Reuven, R., Taragan, E., Duchan, S. and Karni, J. (2001 February). Performance of the directly-irradiated annular pressurized receiver (diapr) operating at 20 bar and 1,200 [degrees] c. *Journal of Solar Energy Engineering*, vol. 123, no. 1. ISSN 0199-6231.

Kröger, D.G. (2008). Spiky central receiver air pre-heater (scrap). Tech. Rep., Stellenbosch University.

Kröger, D.G. (2012). Sunspot - the stellenbosch university solar power thermodynamic cycle. Tech. Rep., Stellenbosch University.

Lubkoll, M. (2017). *Performance characteristics of a spiky central receiver air preheater (SCRAP).* Ph.D. thesis, Stellenbosch University.
Available at: `https://scholar.sun.ac.za`

Lubkoll, M., von Backström, T., Harms, T. and Kröger, D. (2015). Initial analysis on the novel spiky central receiver air pre-heater (scrap) pressurized air receiver. *Energy Procedia*, vol. 69, pp. 461 – 470. ISSN 1876-6102. International Conference on Concentrating Solar Power and Chemical Energy Systems, SolarPACES 2014. Available at: `http://www.sciencedirect.com/science/article/pii/S1876610215003598`

Lubkoll, M., von Backström, T.W. and Kröger, D.G. (2014). Survey on pressurized air receiver development. In: *2nd Southern African Solar Energy Conference 2014*, vol. 27.

McDougall, D. (2019). *Numerical simulation of jet impingement cooling of the inside of a hemisphere with application to SCRAP.* Master's thesis, Stellenbosch University.
Available at: `https://scholar.sun.ac.za`

Mills, A. and Ganesan, V. (1999). *Heat transfer*. 2nd edn. Pearson.

Moghimi, M., Craig, K. and Meyer, J.P. (2015). A novel computational approach to the combine optical and thermal modelling of a linear fresnel collector receiver. 3rd Southern African Solar Energy Conference, South Africa, 11-13 May, 2015.

Oberg, E., Jones, F., Horton, H. and Ryffel, H. (2008). *Machinery's Handbook*. 28th edn. Industrial Press.

Petukhov, B. (1970). Heat transfer and friction in turbulent pipe flow with variable physical properties. In: *Advances in heat transfer*, vol. 6, pp. 503–564. Elsevier.

Požival, P., Aga, V., Zagorskiy, A. and Steinfeld, A. (2014). A pressurized air receiver for solar-driven gas turbines. *Energy Procedia*, vol. 49, pp. 498–503.

Romero, M., Buck, R. and Pacheco, J.E. (2002 May). An update on solar central receiver systems, projects, and technologies.(abstract). *Journal of Solar Energy Engineering*, vol. 124, no. 2. ISSN 0199-6231.

SolarGIS (2013). Poster maps (wall maps) for solar energy. [Online] [Accessed on 07.5.2018].
Available at: `https://solargis.com/maps-and-gis-data/`

SolarPACES, 2017 (2017). Bokpoort breaks a solar thermal energy production record - solarpaces. [Online] [Accessed on 20.07.2019].
Available at: `https://www.solarpaces.org/`

Stine, W.B. and Geyer, M. (2001). *Power from the Sun*.
Available at: `http://www.powerfromthesun.net/book.html`

Versteeg, H.K. and Malalasekera, W. (2007). *An introduction to computational fluid dynamics: the finite volume method*. Pearson education.

Whitaker, S. (1972). Forced convection heat transfer correlations for flow in pipes, past flat plates, single cylinders, single spheres, and for flow in packed beds and tube bundles. *AIChE Journal*, vol. 18, no. 2, pp. 361–371.

Žukauskas, A. (1972). Heat transfer from tubes in crossflow. In: *Advances in heat transfer*, vol. 8, pp. 93–160. Elsevier.

Appendices

Appendix A

Grid dependence of 1-D numerical model

In order to determine the effect of number of control volumes on simulation output resolution, a grid dependence analysis was conducted by running the model at constant input conditions with increasing control volumes. The inputs are arbitrary and do not reflect the conditions experienced during the experimental tests. An inlet air mass flow rate of 0.1 kg/s at 30 °C was specified. A constant irradiation at the spike wall was specified as 2.5 kW/m^2. An exhaust outlet pressure was set as 101.3 kPa. Convergence error was set to 1e-6 for air and wall temperatures as well as inlet pressure. Figure A.1 shows the respective outlet air and root temperatures and total pressure drop across the receiver as a fraction of the output value at 10 control volumes.

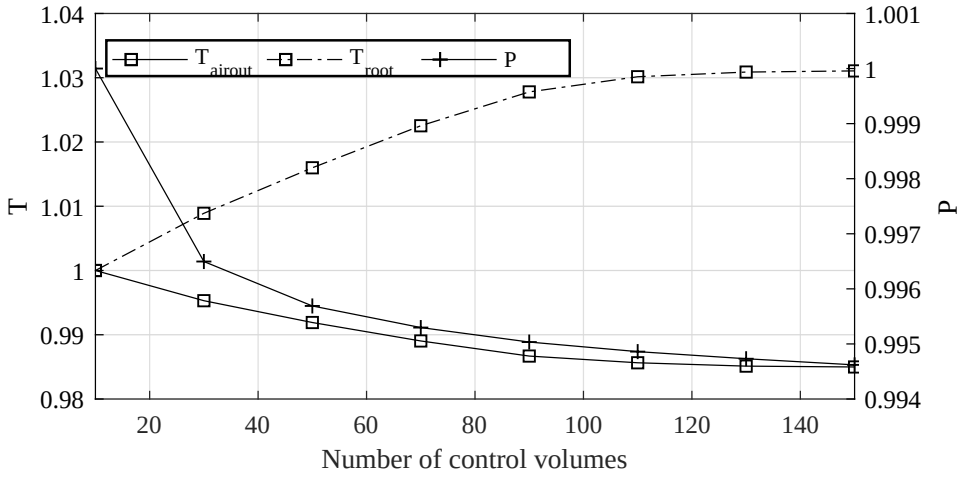

Figure A.1: Temperature and pressure variation for increasing control volumes

From Figure A.1, above 100 control volumes, minor variation is seen in the temperature and pressure data. For increasing control volumes, changing air outlet temperatures are observed due to better resolution of the 1st-order upwind discretization scheme as well as changes in wall temperatures. Here, wall temperatures are primarily affected by the view factor calculation. Figure A.2 shows the average sum of view factors to the surrounding receiver geometry with increasing control volumes. At lower control volumes, the 1-D model gives lower values for the view factors to the surrounding receiver geometry,

leading to lower radiative heat input to the spike and, consequentially, lower wall temperatures. Above 100 control volumes, the view factor calculation shows little variation. Figure A.3 shows the total view factors from a spike element to the components of the surrounding receiver geometry at increasing distance from the spike root for 100 control volumes.

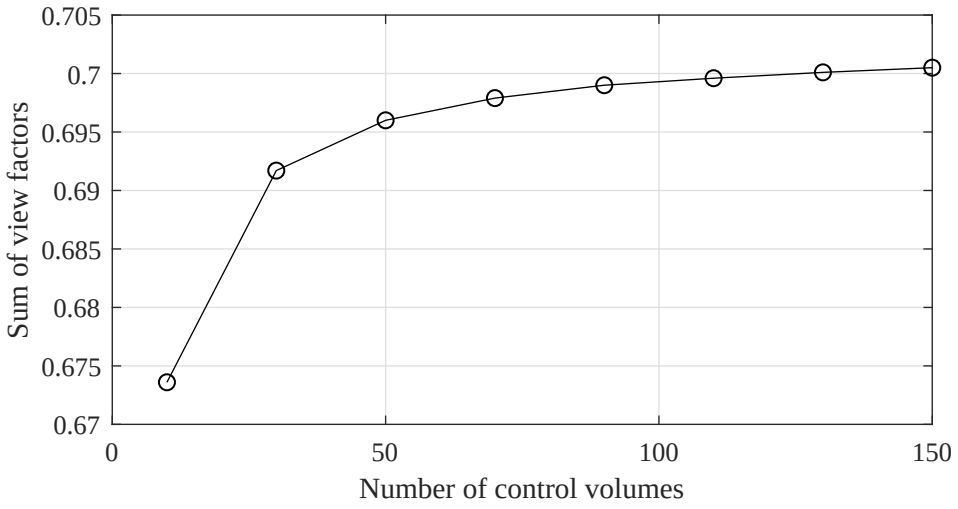

Figure A.2: Sum of view factors for increasing control volumes

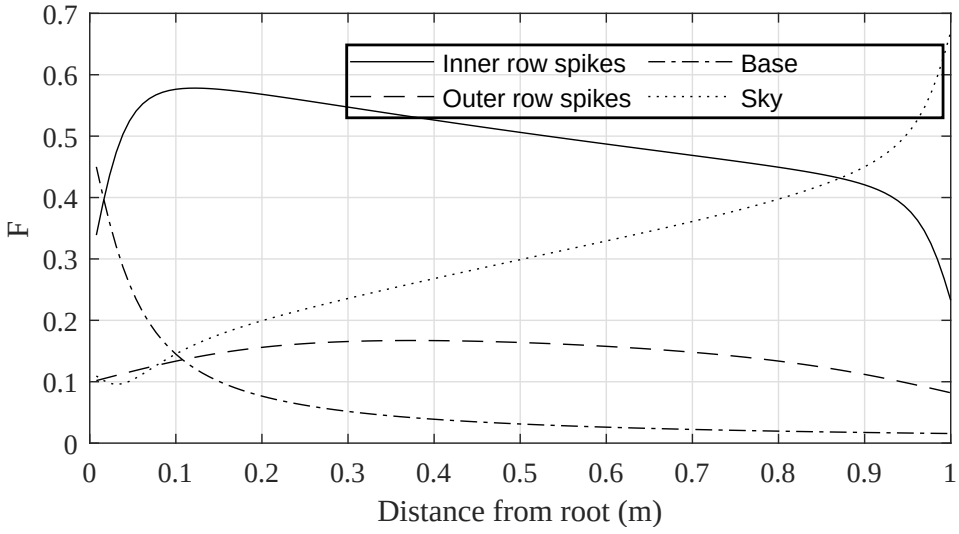

Figure A.3: View factor from a spike element to surrounding receiver geometry and surrounding environment

Appendix B
Numerical model verification

This section discusses the CFD modelling conducted in ANSYS Fluent throughout this work.

B.1 Verification of internal convection heat transfer correlations

In order to verify the internal forced convection heat transfer correlations as set out in Section 4.3, a CFD analysis was conducted in ANSYS Fluent for discrete flow elements of both the open and finned annulus. In this case, 100 mm sections were used. The same reasoning with regards to turbulence model and wall functions as discussed in Section 4.3.4 is applied. For the 1-D model, 100 control volumes were used and external heat transfer from the spike wall was turned off. For both the CFD model and 1-D model, the Fluent default constant fluid properties for air were used.

As with the model in Section 4.3.4, the meshes were refined to give an average wall y^+ value of approximately 11.225, or as close as possible, for a total air mass flow rate of 0.1 kg/s. In both CFD models, a velocity inlet boundary condition was specified to yield the corresponding total mass flow rate. Since it is expected that no recirculation occurs at the outlet, and that the flow is steady and incompressible (due to a constant density), an outflow boundary at the outlets is appropriate. An inlet air temperature of 300 K was specified. To check for convergence of the solution, monitors for average wall y^+ and average heat transfer coefficient was set up. The final residuals for energy, velocity and turbulence parameters was also set to $1e-6$. The average heat transfer coefficients were calculated from

$$h_{avg} = \dot{q}_{wall}(T_{wall,avg} - T_{bulk}) \qquad [\mathrm{W}] \quad \text{(B.1)}$$

B.1.1 Open annulus

For the open annulus model, the spike wall and inner tube temperatures were set to 363 K. Due to the symmetry of the spike around the longitudinal axis, the model can be reduced a 2-D axi-symmetric problem, where the mesh is offset from the longitudinal axis. An example of the coarse mesh is shown in Figure B.1. A bias is applied towards the walls as well as the inlet and

refinement is controlled by changing the number of divisions on the respective faces. Details of increasing mesh sizes is given in Table B.1

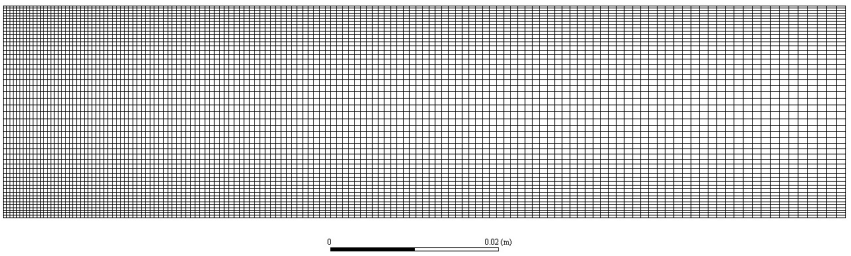

Figure B.1: Coarse mesh example for the open annulus CFD model

Table B.1: Mesh details for open annulus CFD model

Mesh	Cells	Faces	Nodes
1	7150	14493	7344
2	16800	33884	17085
3	27054	54523	27470

The final mesh consisted of 16800 cells and showed an average wall y^+ of 11.51. Further refinement of the mesh did not yield any appreciable difference in average heat transfer coefficient, as shown in Figure B.2.

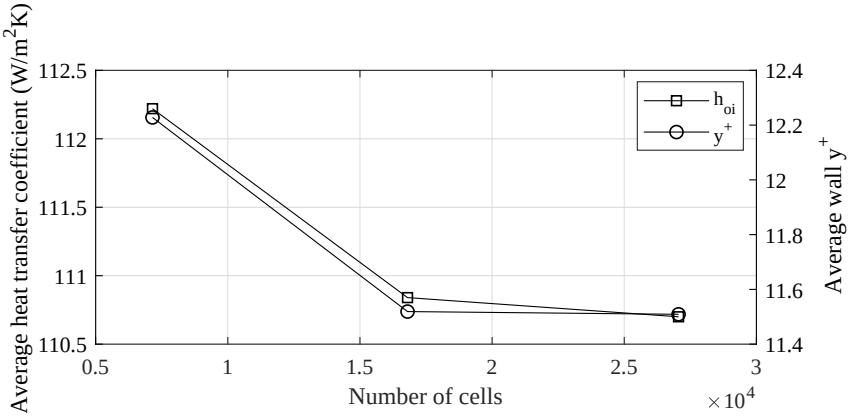

Figure B.2: Average spike wall heat transfer coefficient and y^+ history for increasing mesh resolution

A comparison of the open annulus 1-D and CFD model results is given in Figure B.3. For both the spike wall and inner tube wall heat transfer coefficients, reasonable agreement is shown where small variations occur at lower flow rates. From the temperature increase data, the disparity between the 1-D

1st-order upwind and the CFD 2nd-order upwind solutions are readily apparent. The consistent variation does however show that a physically realistic solution is possible. At higher flow rates it is also shown that the 1-D model increasingly gives larger friction factors and a subsequent increased pressure difference.

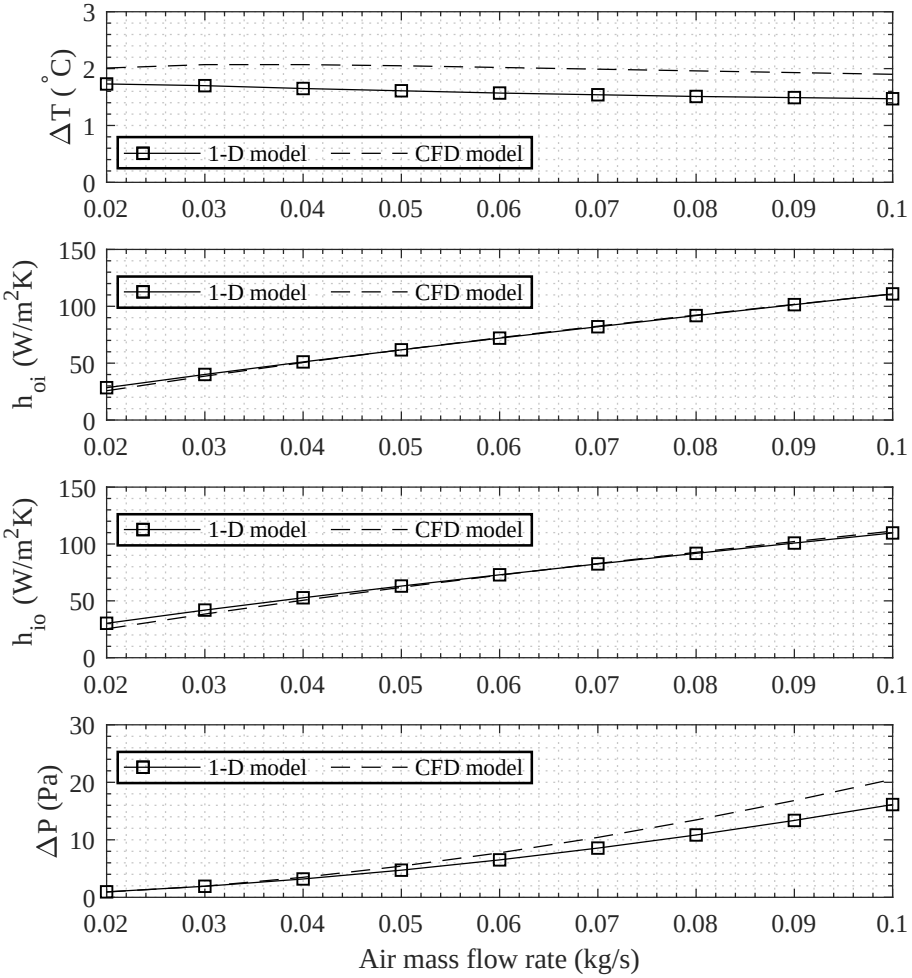

Figure B.3: Comparison of open annulus 1-D and CFD model results for increasing air mass flow rates

B.1.2 Finned annulus

For the finned annulus model, the spike wall and fin temperatures were set to 363 K and 318 K, respectively. Referring to Figure 4.6a, the duct flow area can be said to be symmetric, allowing the use of a symmetric boundary condition and only modelling half of the flow area. Due to the more complex geometry of the duct, fitting a structured cartesian mesh such as the open annulus example is not possible. A quadrilateral-dominant hybrid mesh is therefore used where the mesh is well structured at the edges. As can be seen in Figure B.4, where

the wall, fin and symmetry zones meet, an unstructured mesh is generated. An inflation layer is also applied at the wall and fin surfaces. Mesh refinement was controlled through the global mesh element size as well as the number of longitudinal divisions as shown in Figure B.5. Details of increasing mesh sizes is given in Table B.2

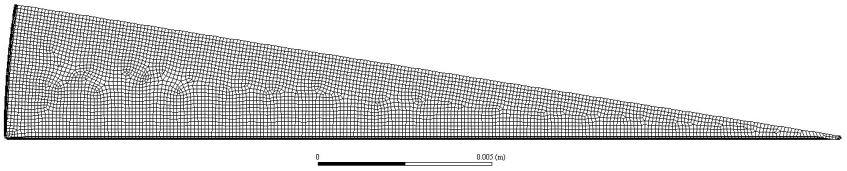

Figure B.4: Intermediate mesh at duct inlet

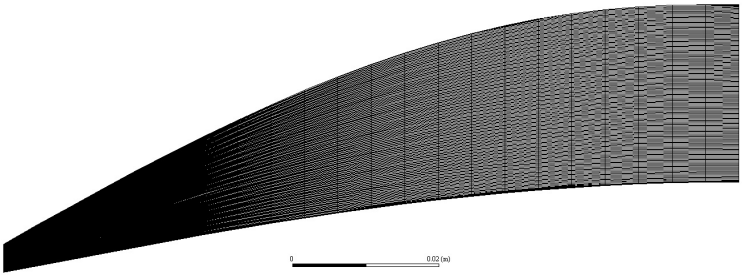

Figure B.5: Longitudinal view of duct mesh

Table B.2: Mesh details for finned annulus CFD model

Mesh	Cells	Faces	Nodes
1	27456	86454	31694
2	54340	169450	609450
3	107228	332190	118013
4	214258	660543	232415
5	426844	1311198	458045

The final mesh consisted of 214258 cells and showed an average wall y^+ of 11.54. Further refinement of the mesh did not yield any appreciable difference in average heat transfer coefficient, as shown in Figure B.6. A comparison of the open annulus 1-D and CFD model results is given in Figure B.3. At lower flow rates, the 1-D model continuously over-calculates the average heat transfer coefficient. This improves to a close match of the CFD values for increasing flow rates. At low flow rates, a significant variation is also seen

between temperature differences, which is due to both the 1-D model over-calculation of heat transfer coefficient as well as the use of a 1st-order upwind discretization scheme.

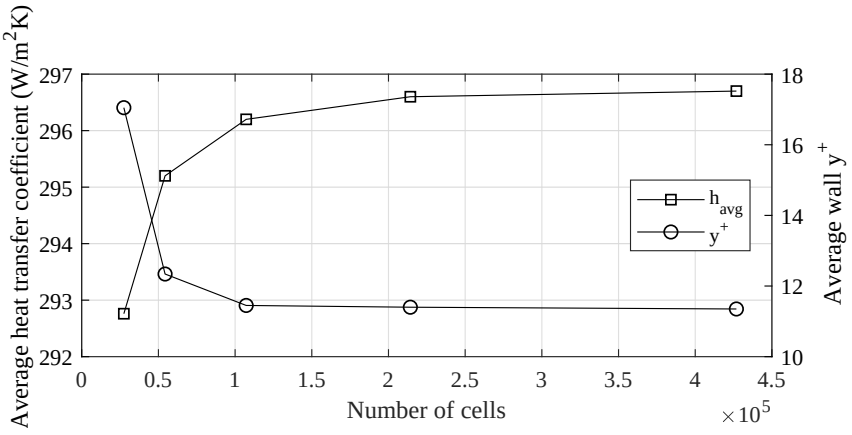

Figure B.6: Average duct heat transfer coefficient and y^+ history for increasing mesh resolution

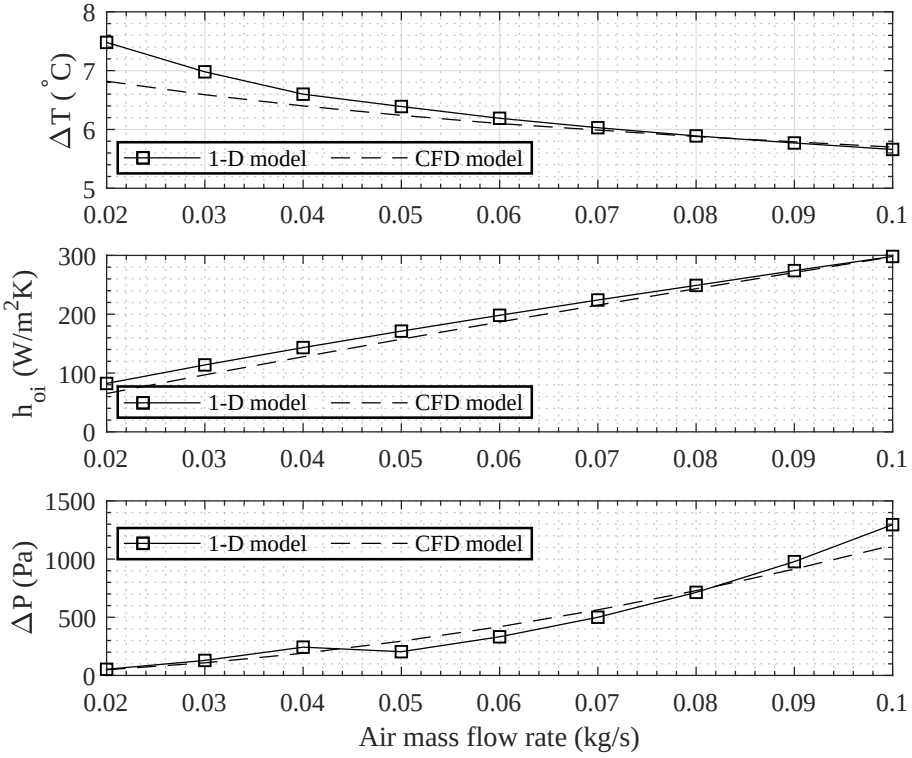

Figure B.7: Comparison of finned annulus 1-D and CFD model results for increasing air mass flow rates

For the pressure drop, a similar phenomenon is observed as noted in Grobler (2015), where the friction factor correlations under-predict friction factor at low flow rates and over-predict at higher flow rates. The discontinuity in pressure drop is also observed as Reynold's number transitions to $Re > 8000$, switching between friction factor correlations. The data shows does show, however, that the choice of mean coil diameter as between duct centroids is appropriate.

B.2 Tip CFD model

Details for increasing mesh sizes used to develop the tip heat transfer correlation discussed in Section 4.3.4 is given in Table B.3. Convergence history of average wall y^+ and average wall heat transfer coefficient are also given in Figure B.8.

Table B.3: Mesh details for tip CFD model

Mesh	Cells	Faces	Nodes
1	33351	67035	33685
2	48191	96766	48576
3	87928	176287	88360
4	137622	275724	138103

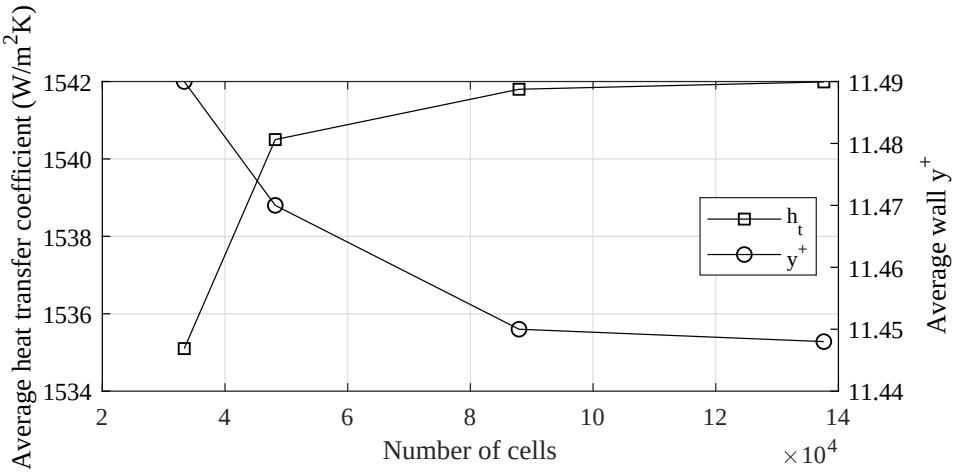

Figure B.8: Average tip heat transfer coefficient and y^+ history for increasing mesh resolution

B.3 DO irradiation CFD model

For the DO irradiation model discussed in Section 6.5, an initial focal point was set at 1 m behind the spike tip so that the highest amount of false diffusion would be induced as the irradiation direction would be dis-aligned with the computational mesh. The amount of azimuth and elevation angular divisions was then increased until the final average surface incident irradiation on the spike wall equalized. This process was repeated for four separate meshes of increasing density for both 1st and 2nd-order upwind discretization schemes. Figure B.9 shows the convergence history for the separate meshes given in Table B.4. The notation used is *M-mesh number-discretization scheme*.

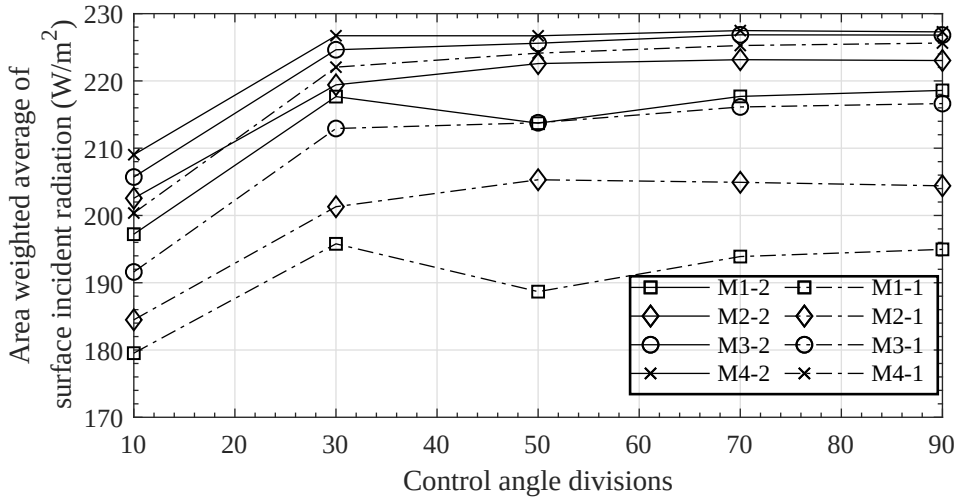

Figure B.9: Average surface incident radiation on spike wall for increasing control angle divisions

Table B.4: Mesh details for spike DO radiation model

Mesh	Cells	Faces	Nodes
1	506	1065	555
2	1439	2995	1549
3	4094	8416	4323
4	11643	23719	12077

Figure B.10 shows a contour plot of total irradiation for the mesh used with an aperture focal point at the spike root. A distinction is made between total irradiation and surface incident radiation; total irradiation is the irradiation at a given point in the domain, while surface incident radiation is the radiation component normal to a surface.

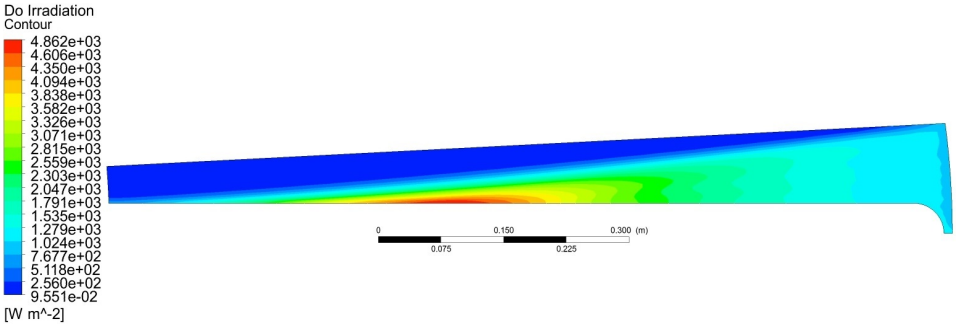

Figure B.10: Contour plot of total irradiation with an aperture focal point at the spike root

Appendix C

1-D numerical model validation

After verifying the internal heat transfer for both open annulus and finned annulus 1-D numerical models in Section B, the experimental data can be used to validate the 1-D model for given measured experimental inputs. From the experimental results presented in Section 6, a significant amount of variation is seen in the measured temperature data due to the constantly changing thermal inertia of the experimental receiver with changes in wind speed and direction, as well as changes in air mass flow rate.

Where the 1-D model would calculate a steady-state operation of the experimental receiver, true steady-steady state is never achieved in practice. As such, validation data points are taken as the average values between two time points for the same air mass flow rate. To ensure that changes in thermal inertia due to changes in air mass flow are reduced, the time points are taken as the 5 minutes preceding an increase in air mass flow where the operation was closest to a perceived steady-state.

C.1 Open annulus model

For the open annulus model, a case was chosen between 14:38 to 14:42 for an average air mass flow rate of 0.062 kg/s, and between 14:50 to 14:55 for an average air mass flow rate of 0.086 kg/s. The first case is presented in Section 6. The second case is presented here.

C.1.1 Case 2

Experimental data for the second case between 14:50 to 14:55 is given in Table C.1. The 1-D model outputs for both irradiation concentration profiles are given in Figure C.1 and Figure C.2. For the second case, p_{sol1} shows equal over and under prediction of approximately 10 °C. Here, p_{sol2} shows a maximum surface temperature variation of approximately 6 °C.

Table C.1: Comparison of model output to measured experimental data for open annulus spike: Case 2

Parameter	14:50	14:55	Average	Model (p_{sol1})	Model (p_{sol2})
T_{amb} (°C)	28.68	29.07	28.88	-	-
$T_{air,in}$ (°C)	33.70	33.30	33.50	-	-
$T_{air,out}$ (°C)	50.23	48.73	49.48	50.22	48.36
T_1 (°C)	71.86	77.63	74.74	77.46	69.99
T_2 (°C)	72.20	71.63	71.91	85.18	74.08
T_3 (°C)	81.59	80.05	81.04	90.11	78.70
T_4 (°C)	111.70	108.0	109.85	100.30	103.40
$\dot{q}_{ap}$ (kW/m^2)	51.14	51.55	51.34	-	-
V_w (m/s)	2.81	2.24	2.15	-	-
V_θ (°)	245	238	-	-	-
$\dot{m}$ (kg/s)	0.087	0.085	0.086	-	-

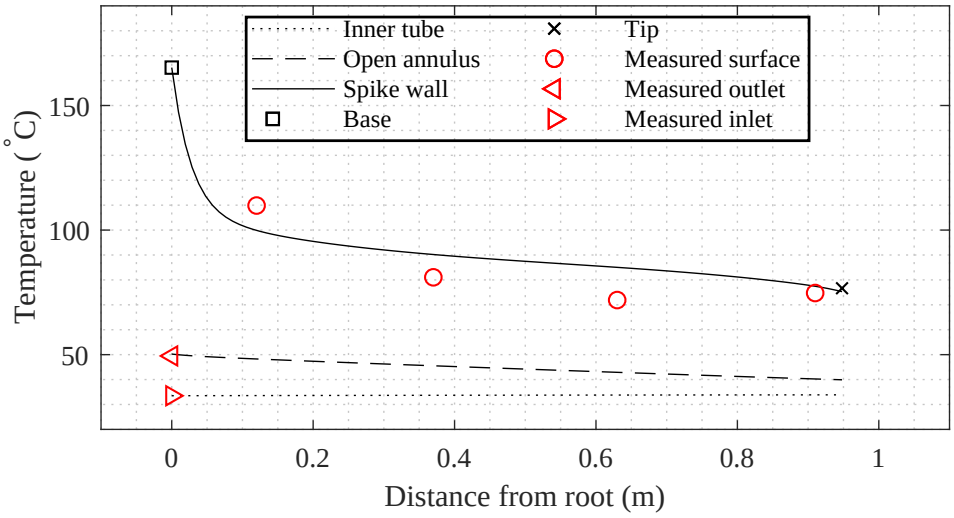

Figure C.1: Open annulus 1-D model output with irradiation concentration profile p_{sol1}: Case 2

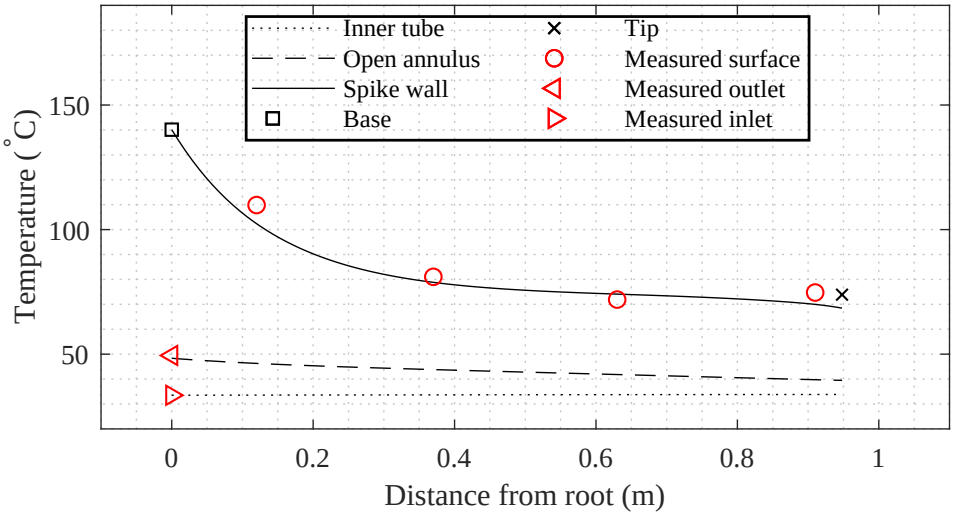

Figure C.2: Open annulus 1-D model output with irradiation concentration profile p_{sol2}: Case 2

C.2 Finned annulus model

For the finned annulus spike, the same process is followed. Discontinuous irradiation concentration profiles, p_{sol1f} and p_{sol2f} shown in Figure C.3, are used.

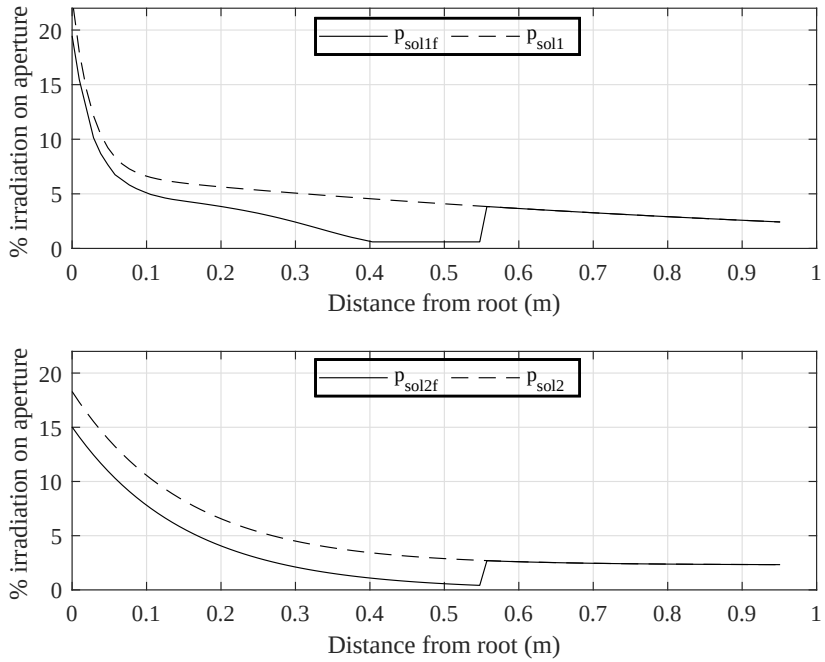

Figure C.3: Comparison of modified irradiation concentration profiles, p_{sol1f} and p_{sol2f} on spike surface

The first profile, p_{sol1f}, is also obtained from the DO irradiation model presented in Section 6.5. For p_{sol2f}, the static component of 2.3% is removed from p_{sol2}. Both p_{sol1f} and p_{sol2f} exhibit the same total irradiation input to the spike surface, within 1%, and both profiles exhibit approximately 62% of the total un-flanged irradiation input to the spike.

C.2.1 Case 1

Experimental data for the first case between 12:40 to 12:45 is given in Table C.2. The 1-D model outputs for both irradiation concentration profiles are given in Figure C.4 and Figure C.5. From Table C.2, both irradiation concentrations show similar deviation from the experimental results with maximum variation in open annulus surface temperatures of approximately 10 °C. A larger variation of 17 °C is seen in the tip surface temperatures. Since the finned section wall temperatures are not measured, the maximum fin temperatures measured at 8 mm are provided here and 1-D model wall temperatures are given. Estimate values for wall temperatures obtained by linear extrapolation from Figure 6.14 is provided in brackets.

Table C.2: Comparison of model output to measured experimental data for finned annulus spike: Case 1

Parameter	12:40	12:45	Average	Model (p_{sol1f})	Model (p_{sol2f})
T_{amb} (°C)	31.01	31.30	31.15	-	-
$T_{air,in}$ (°C)	31.82	31.50	31.66	-	-
$T_{air,out}$ (°C)	44.53	44.37	44.45	48.62	48.17
T_{tip} (°C)	110.9	108.3	109.6	93.75	93.73
T_1 (°C)	86.03	84.14	85.58	78.80	76.06
T_2 (°C)	89.99	92.12	91.05	92.85	91.06
T_{F1max} (°C)	42.38	41.48	41.93 (50.74)	50.64 (wall)	49.33 (wall)
T_{F2max} (°C)	45.31	45.10	45.20 (52.90)	53.0 (wall)	51.77 (wall)
$\dot{q}_{ap}$ (kW/m^2)	55.45	56.24	55.84	-	-
V_w (m/s)	2.08	1.513	1.708	-	-
V_θ (°)	211.2°	245°	-	-	-
$\dot{m}$ (kg/s)	0.083	0.0824	0.0827	-	-

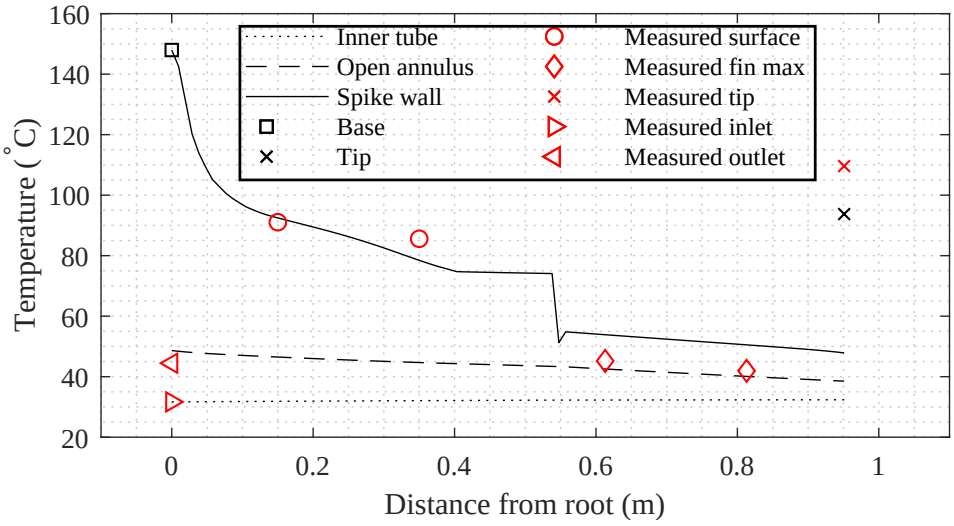

Figure C.4: Finned annulus 1-D model output with irradiation concentration profile p_{sol1f}: Case 1

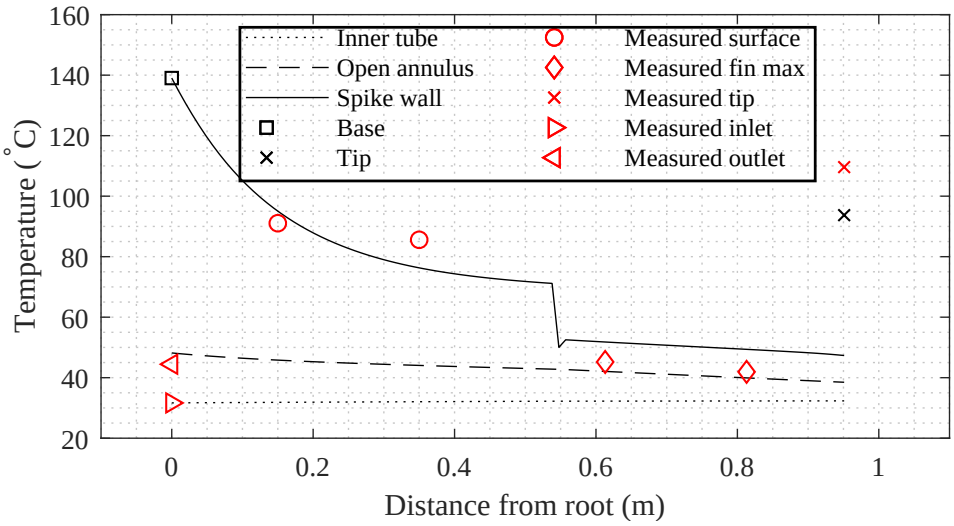

Figure C.5: Finned annulus 1-D model output with irradiation concentration profile p_{sol2f}: Case 1

C.2.2 Case 2

Experimental data for the second case between 14:30 to 14:35 is given in Table C.3. The 1-D model outputs for both irradiation concentration profiles are given in Figure C.6 and Figure C.7. From Table C.3, both irradiation concentration profiles show similar deviation from the experimental results with maximum variation in open annulus surface temperatures below 10 °C. A lower variation of 2 °C is seen in the tip surface temperatures.

For the open annulus model, where surface temperatures showed variations within 10 °C, outlet air temperatures showed a variation of approximately 2 °C. With the addition of the finned annulus section in the 1-D model, the outlet air temperature variation increases to a maximum of 5 °C.

Table C.3: Comparison of model output to measured experimental data for open annulus spike: Case 2

Parameter	14:30	14:35	Average	Model (p_{sol1})	Model (p_{sol2})
T_{amb} (°C)	35.89	34.18	35.03	-	-
$T_{air,in}$ (°C)	33.38	32.33	32.85	-	-
$T_{air,out}$ (°C)	49.19	47.76	48.47	52.57	52.00
T_{tip} (°C)	106.3	110.0	108.13	110.6	108.1
T_1 (°C)	76.84	80.69	78.76	77.96	75.95
T_2 (°C)	84.54	88.81	86.67	92.69	94.90
T_{F1max} (°C)	45.81	44.46	45.13 (51.40)	54.87 (wall)	53.55 (wall)
T_{F2max} (°C)	48.66	46.79	47.72 (53.56)	58.71 (wall)	56.29 (wall)
$\dot{q}_{ap}$ (kW/m^2)	58.67	58.92	58.79	-	-
V_w (m/s)	2.41	2.67	2.015	-	-
V_θ (°)	241°	254°	-	-	-
$\dot{m}$ (kg/s)	0.064	0.063	0.0635	-	-

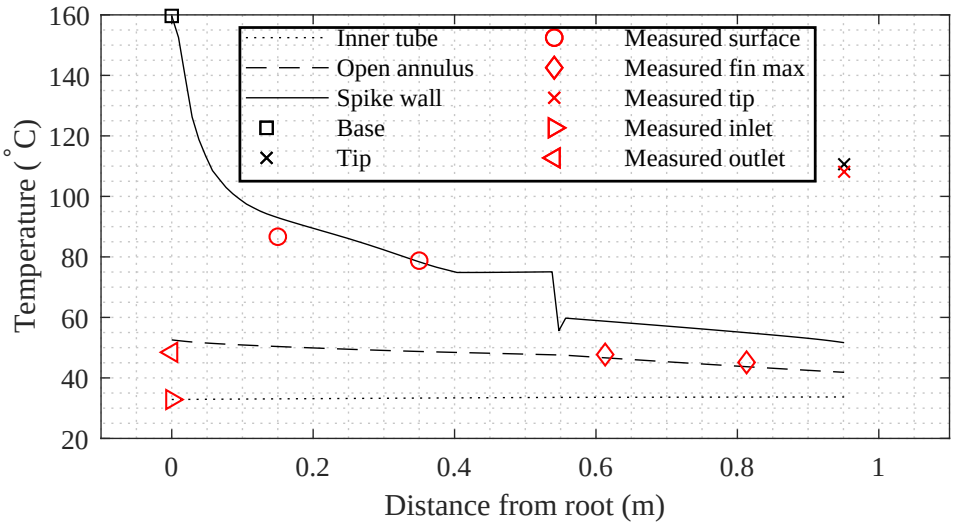

Figure C.6: Finned annulus 1-D model output with irradiation concentration profile p_{sol1f}: Case 2

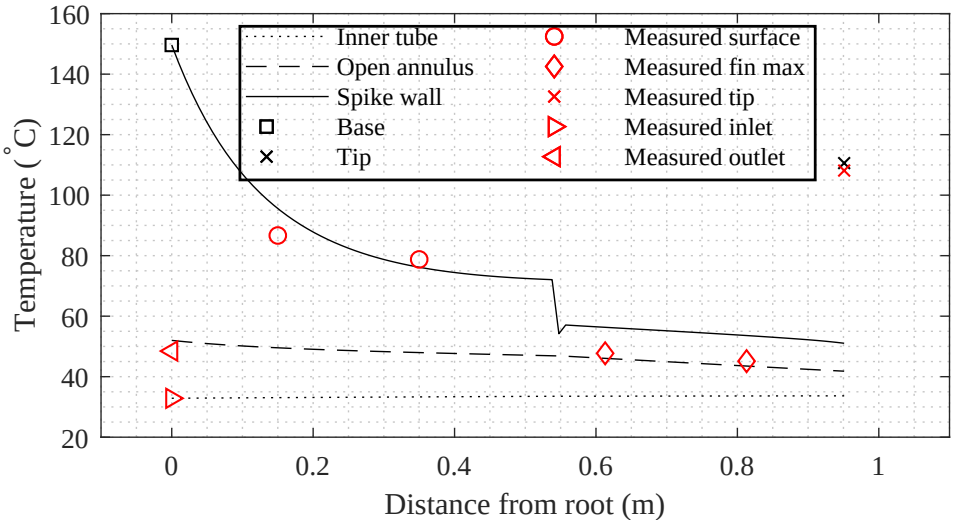

Figure C.7: Finned annulus 1-D model output with irradiation concentration profile p_{sol2f}: Case 2

C.3 Discussion

Given the large amount of variation in the experimental data, it is difficult to absolutely quantify overall error in the numerical model. Here, the internal forced convection Nusselt number correlations for the open annulus is directly applicable. In the case of the coiled triangular ducts, the Nusselt number correlations are intended for coiled tubes and thus only partly applicable. The Nusselt number correlations, also, do not account for differences in local heat transfer coefficients between the fin and outer wall. It was, however, shown through CFD modelling of a discrete duct section that both 1-D model and CFD model values are in good agreement.

From the given cases, it is seen that the 1-D numerical model can, where steady state operation is observed, predict the spike wall temperatures to within a maximum of approximately 12 °C using the irradiation concentration profile given by p_{sol2}. For both models, the 12 °C variation in surface temperatures yield a corresponding maximum variation in outlet air temperature of approximately 5 °C. A conservative estimate for outlet air temperature variation for a full length finned spike is then taken as 5 °C.

Appendix D

Experimental procedure

The experimental procedure was split into 3 parts: start-up, operation and shut-down.

1. Start-up
    a) Start data logger and check that all sensors are active and measuring probable values corresponding with ambient conditions.
    b) Remove facet covers, wash heliostats and reinstall facet covers.
    c) Hang warnings at lab entrances to indicate tests are taking place.
    d) Turn on backup power source and power heliostat field - this will turn on door alarms and warning lights.
    e) Turn on air flow through the receiver.
    f) Begin calibration of heliostats with facet covers on, defocussing after calibration.
    g) Remove facet covers and focus heliostats on receiver.
2. Operation
    a) Monitor temperatures on the receiver.
    b) Wait for temperatures to reach steady state and hold for at least 5 min.
    c) Adjust mass flow rate to obtain new data set and wait for steady state.
    d) Repeat process until the required mass flow range is obtained.
    e) Check that all heliostats are focused on receiver.
    f) Recalibrate individual heliostats if significant drift is observed.
3. Shut-down
    a) Defocus heliostats and reinstall facet covers.
    b) Stow heliostats and turn off power to heliostat field.
    c) Turn off air flow.
    d) Stop datalogger.

Appendix E
Calibration Data

The following section discusses the instrumentation used throughout the project for the experimental setup, covering the calibration and error analysis.

E.1 Solar radiation

DNI and flux concentration measurements were taken using Kipp & Zonen CMP11 pyranometers. The DNI and flux concentration pyranometers have a sensitivity of $8.99 \times 10^{-6}\,\mathrm{V/Wm^{-2}}$ and $8.70 \times 10^{-6}\,\mathrm{V/Wm^{-2}}$ respectively with a range of $0\,\mathrm{W/m^2}$ to $4000\,\mathrm{W/m^2}$. The manufacturer datasheet reports a directional response (up to 80° with a $1000\,\mathrm{W/m^2}$ beam) of less than $10\,\mathrm{W/m^2}$. This gives an error of 1 %.

E.2 Temperature

The thermocouples used throughout the experimental process were J-type thermcouples with an uncertainty of ±1 °C. These thermocouples consisted of 6 mm diameter, 3 m lead or 1.5 mm diameter, 2.5 m lead. The leads were fiberglass insulated, stainless steel braided cables. The thermocouples were calibrated using a FLUKE 9150 portable furnace over a temperature range of 50 °C to 350 °C. From Figure E.1, the J-type thermocouples returned significant reading errors below 100 °C. Above 120 °C, the 6 mm thermocouples reported a maximum of 4 % error and the 1.5 mm thermocouples reported a maximum of 1 % error.

It should be noted that the FLUKE 9150 portable furnace has an operating range of 150 °C to 1200 °C. This would explain the large and non-linear error experienced below 150 °C. The maximum thermocouple errors obtained above 150 °C is therefore used.

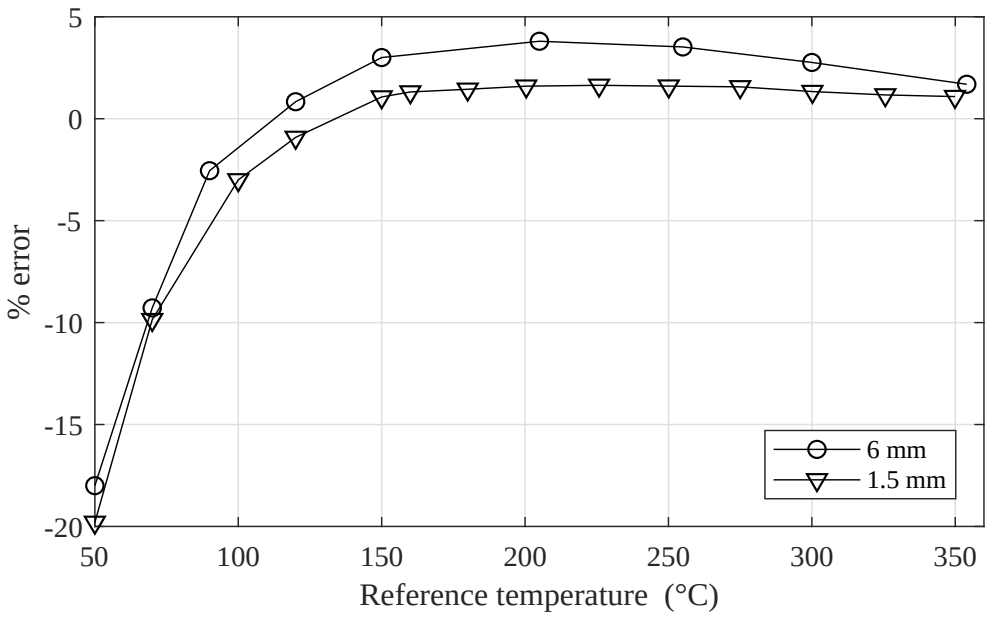

Figure E.1: Calibration curves for 6 mm and 1.5 mm J-type thermocouples

E.3 Data acquisition

For data acquisition throughout the experimental process, a National Instruments data logger (cDAQ-9174) with NI 9213 thermocouple modules and NI 9215 BNC module were used. According to manufacturer datasheets, the NI 9213 and NI 9125 have errors of ±1 °C and 0.02 % respectively.

E.4 Pressure

For pressure measurement, two Endress+Hauser Deltabar M PMD55 differential pressure transducers were used. The transducers have a measurement span of 15 kPa to 300 kPa. According to manufacturer datasheets, the transducers report a maximum of ±3 % error at 300 kPa. The pressure transducers were calibrated using a FLUKE 700PTP1 pneumatic test pump and FLUKE 700G32 10K pressure gauge.

Departmental serial numbers, 2 and 5, will be used to differentiate the two transducers. Transducer 2 was used to measure pressure drop in the pipe discussed in Section E.5. Transducer 5 was used to measure pipe inlet pressure relative to atmospheric pressure. Calibration curves for the transducers are shown in Figure E.2. Transducer 5 and 2 gave zero-readings at 400 Pa (1.99 V) and 20 Pa (2.00 V) respectively.

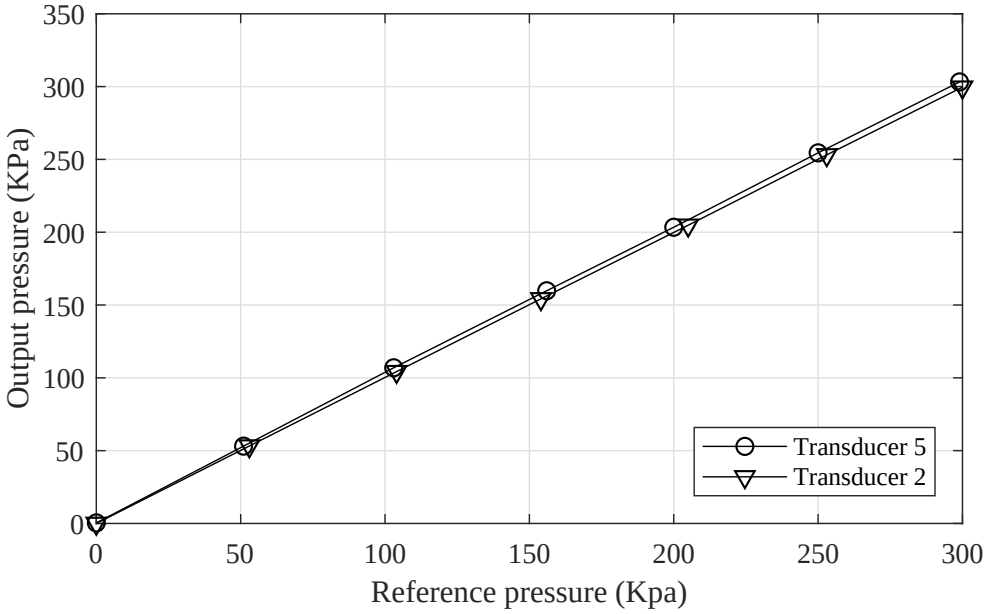

Figure E.2: Calibration curves for Endress+Hauser pressure transducers

E.5 Mass flow

An initial attempt to obtain a calibration curve for the flow meter involved attaching a centrifugal fan to the outlet and sucking air through the pipe with a bellmouth inlet. A bellmouth inlet utilizes the Bernoulli principle given as

$$\frac{P_1}{\rho g} + \frac{V_1^2}{2g} = \frac{P_2}{\rho g} + \frac{V_2^2}{2g}$$

By assuming the inlet velocity at the bellmouth is effectively zero, and assuming negligible fluid compression, the pressure drop between the bellmouth inlet and throat can be used to calculate the fluid velocity through the bellmouth. Rewriting the Bernoulli equation to include the pressure drop contribution from the bellmouth gives,

$$\frac{P_1}{\rho g} + \frac{V_1^2}{2g} = \frac{P_2}{\rho g} + \frac{V_2^2}{2g} + \frac{K_l V_2^2}{2g}$$

where K_l can be taken as 0.03 for a well rounded inlet. The resulting equation can then be rearranged to give the fluid velocity at the bellmouth throat,

$$V_2 = \sqrt{\frac{\Delta P}{\rho\left(\frac{1}{2} + \frac{K_l}{2}\right)}}$$

By measuring the pressure drop across the bellmouth, the flow velocity and subsequently volumetric flow-rate could be determined. The bellmouth

volumetric flow rate and corresponding pressure drop across the pipe is then used to develop a correlation for the pressure drop across the pipe for a given volumetric flow rate. Both raw data and correlation is given in Figure E.3. The limitation of this approach is that flow rate obtained using a centrifugal fan for suction is very low. As pressure drop for both friction and obstruction losses is proportional to u_b^2, friction losses will dominate at higher flow velocities for a uniform pipe. The developed correlation would then need to be extrapolated to flow rates where the friction losses are not taken into account and uncertainty is too great to yield any reliable data.

The second approach was to model the flow meter in Flownex. Considering the ease of simulation setup, quick runtime and intuitive interface, results could be obtained fairly quickly. However, in order to obtain accurate results, specific internal surface roughness values for galvanized pipe as well as specific pressure loss coefficients for the elbows were needed. In practice, these are hard to determine and therefore the Flownex model relies on generic roughness and loss coefficient values. In Figure E.3, large deviation is seen between the initial fan calibration method and the Flownex simulation.

Towards the end of the testing phase, a Festo SFAM-90 volumetric air flow meter was obtained. Manufacturer datasheets state an error of $3\,\% + 0.3\,\%$ of the measuring range final value. The Festo flow meter was only available for a short time and could therefore not be permanently integrated as part of the test setup. Instead, the Festo flow meter was connected to the pipe and a short analysis was conducted to determine the pressure drop across the pipe for a given Festo flow meter reading.

At first, the pipe was disconnected from the downstream tower section and a flow rate - pressure drop curve obtained. The pipe was then reconnected to the downstream tower section and tested again. The latter setup was the closest scenario to real testing conditions. As shown in Figure E.3, at low volumetric flow, initial fan calibration data and Festo flow meter data show good agreement. At high volumetric flow as shown in Figure E.4, the fan calibration, Flownex and first Festo flow meter calibration methods all showed varying degrees of variance and were therefore not viable options in determining the mass flow rate.

The large variation in "In-situ" and the various disconnected pressure curves can easily be explained by utilizing the conservation of mass principle. Assuming high inlet pressure, the pressure drop along a uniform pipe will be spread such that the outlet pressure can be assumed to approximate atmospheric pressure. Rewriting the conservation of mass formula as

$$\frac{\dot{m}}{A} = \rho u_b$$

it is deduced that the product of density and bulk fluid velocity must remain constant. With no heat input to the fluid, density is then purely a function of pressure. Along the length of the pipe, friction at the pipe wall causes a

pressure drop and subsequently an increase in bulk fluid velocity. As such, a non-uniform velocity distribution results. The magnitude of this velocity difference depends largely on the pressure differential across the pipe.

The "In-situ" tests were conducted with a downstream pipe section of roughly 22 m. The pressure drop across the flow meter was therefore only a percentage of the total pressure drop, as opposed to the disconnected tests where the pressure drop across the flow meter accounted for the entire pressure drop. Consequentially, the flow rate-pressure curve for a given downstream setup is invalid for a different downstream setup. The "In-situ" data obtained was used to develop a correlation between pressure drop across the pipe and volumetric flow rate. The correlation is given by

$$\dot{Q}_{pipe} = 1.021 \times 10^{-6} \Delta P + 0.003688 \qquad [\mathrm{m^3/s}] \quad \text{(E.1)}$$

The final mass flow rate is determined by

$$\dot{m}_{pipe} = \rho_{pipe\_inlet} \dot{Q}_{pipe} \qquad [\mathrm{kg/s}] \quad \text{(E.2)}$$

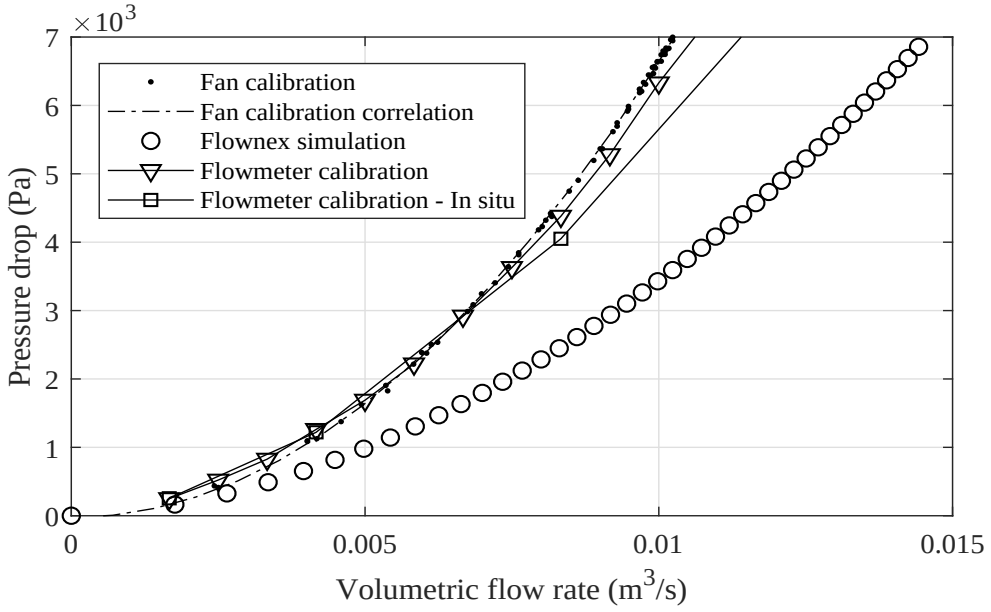

Figure E.3: Pressure - flow rate curves for pipe at low volumetric flow

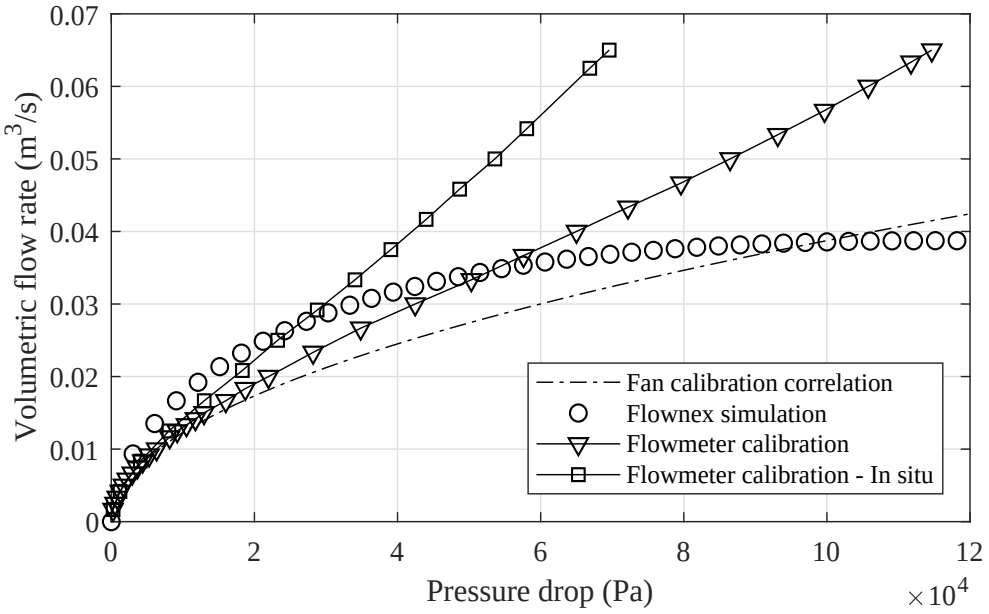

Figure E.4: Flow rate - pressure curves for pipe at high volumetric flow

E.6 Wind speed and direction

Wind speed and direction data is obtained from the Sonbesie weather station, situated approximately 50 m from the receiver tower. Wind speed and direction is measured using an R. M. Young Wind Sentry Set (03001). The manufacturer datasheet reports an accuracy of ± 0.5 m/s for wind speed and an accuracy of $\pm 5^{\circ}$ for wind direction.

E.7 Error estimation

The final overall error is calculated by taking the root mean square of the previously mentioned instrumentation errors. Table E.1 gives an overview of the discussed instrumentation error with the final overall error.

Table E.1: Summary of experimental instrumentation errors

Instrument	% Error
J-type thermocouple (6 mm)	4% + 1%
J-type thermocouple (1.5 mm)	1% + 1%
Transducer 2 (Flow rate)	3% + 0.02%
Transducer 5 (Density)	3% + 0.02%
Festo flow meter	3.3%
DNI pyranometer	1%
Total	7.689%

Appendix F

Air and material properties

The thermal properties of air used in the 1-D numerical model are given here. Polynomial regression was done in Matlab R2017 using the curve fitting toolbox which allows the user to fit a polynomial of predefined order to a dataset. The data was obtained from Mills and Ganesan (1999). The curves are calculated at 100 kPa with a temperature range of 150 K to 800 K.

F.1 Air

$$k = -1.734 \times 10^{-4} T^2 - 7.683 \times 10^{-5} T + 0.00519 \quad [\mathrm{W/mK}] \quad (F.1)$$

$$c_p = 0.0003579 T^2 - 0.223 T + 1041 \quad [\mathrm{J/kgK}] \quad (F.2)$$

$$\mu = -2.06 \times 10^{-11} T^2 + 5.742 \times 10^{-8} T + 2.959 \times 10^{-6} \quad [\mathrm{kg/ms}] \quad (F.3)$$

$$Pr = \frac{c_p \mu}{k} \quad (F.4)$$

$$\rho = \frac{P_{air}}{R T_{air}} \quad [\mathrm{kg/m^3}] \quad (F.5)$$

where $R = 287\,\mathrm{J/kgK}$ is the gas constant of air.

F.2 SAE 1008 mild steel

The thermal properties of SAE 1008 mild steel are given for a temperature range of 200 K to 900 K (Mills and Ganesan, 1999)

$$k_s = 1.879 \times 10^{-5} T^2 - 0.05858 T + 76.65 \quad [\mathrm{W/mK}] \quad (F.6)$$

$$c_{p,s} = -2.045 \times 10^{-5} T^2 + 0.4351 T + 309.2 \quad [\mathrm{J/kgK}] \quad (F.7)$$